

Parameterizing Ion–Lipid Interactions from Local Clusters to Reproduce Experimental Bulk  
Properties of Lipid Bilayers

by

Matthew W. Saunders

A thesis submitted in partial fulfillment  
of the requirements for the degree of  
Doctorate of Philosophy in Cell & Molecular Biology

Department of Molecular Biosciences  
College of Arts and Sciences  
University of South Florida

Co-Major Professor: Sameer Varma, Ph.D.

Co-Major Professor: Sagar Pandit, Ph.D.

Jianjun Pan, Ph.D.

Libin Ye, Ph.D.

Stanley Stevens, Ph.D.

Date of Approval:  
TBD

Keywords: Molecular Dynamics, ???

Copyright © 2025, Matthew W. Saunders

## Contents

List of Tables	vi
List of Figures	viii
Abstract	1
1 Introduction	2
1.1 Phospholipid bilayers	2
1.2 Molecular Simulations	3
1.2.1 Classical Molecular Dynamics	3
1.2.2 Mixing rules, and NB-fix	4
1.2.3 <i>Ab initio</i> calculations and Density Functional Theory	6
1.3 Comparing Molecular Simulations with Experimental Results	7
1.3.1 SAXS (and SANS) – and other properties obtained from density distributions	7
1.3.2 Number density histograms	8
1.3.3 Lipid component volumes	8
1.3.4 Electrostatic and dynamic results... such as GC-theory!	8
1.3.5 Diffusion coefficients	8
1.3.6 Order parameters	8
2 A high dimensional parameter search method to...	9
2.1 Abstract	9
2.2 Introduction	10
2.3 Methods	12
2.3.1 Quantum Mechanical Calculations	13
2.3.2 Parameter Optimization	13
2.3.3 Bilayer Construction	16
2.3.4 Molecular Dynamics	17
2.4 Results and Discussion	17

2.4.1	Optimized Cross-Terms	17
2.4.2	Validation of Parameters	19
2.4.3	Membrane-Salt Interactions	23
2.4.4	Water Structure and Dynamics	25
2.4.5	Bilayer Electrostatics	28
2.5	Conclusions	30
3	Adsorption modes of $\text{Na}^+$ , $\text{Li}^+$ , and $\text{Mg}^{2+}$ to a model zwitterionic lipid bilayer	41
3.1	Abstract	41
3.2	Introduction	41
3.3	Methods	43
3.3.1	Bilayer Construction	43
3.3.2	Molecular Dynamics	44
3.3.3	Force-field parameters	44
3.4	Results and Discussion	47
3.4.1	Bilayer simulations of $\text{Li}^+$ and $\text{Mg}^{2+}$	47
3.5	Specific ion adsorption	51
3.5.1	Bulk ions	51
3.5.2	Adsorbed ions	55
3.6	Conclusions	63
4	Alteration of bilayer structure by $\text{Mg}^{2+}$	64
4.1	Abstract	64
4.2	Introduction	65
4.3	Methods	67
4.3.1	$\text{Mg}^{2+}$ Model Parameters	67
4.3.2	Bilayer Construction	74
4.3.3	Molecular Dynamics	74
4.4	Results and Discussion	74
4.4.1	Water structure, and hydration boundaries	74
4.5	$\text{Mg}^{2+}$ Adsorption Behavior	76
4.6	Bilayer Structure	80
4.6.1	Acyl-Chain order parameters	83
4.7	Conclusions	86
5	Conclusions	88



## List of Tables

2.1	QM Total energies of small molecules	14
2.2	Self energies of isolated molecules	14
2.3	Nelder–Meade constraints	14
2.4	Force–field cross terms	17
2.5	Nelder–Meade constraints. These values were used to constrain the parameter search space during the NM–optimization.	18
2.6	Bilayer structural parameters	20
2.7	Diffusion coefficients of water in different regions	27
3.1	Simulation system details	43
3.2	Mg <sup>2+</sup> binding energies to water	46
3.3	Lennard-Jones cross-terms for Mg <sup>2+</sup>	47
3.4	Bilayer simulation details and structure	49
3.5	Poisson-boltzmann theory parameters	54
3.6	Fractions per lipid of cations per adsorption mode	59
3.7	Fractions per lipid of anions per adsorption modality	59

4.1	NM Constraints	69
4.2	Lennard-Jones cross-terms	71
4.3	Energies (kJ/mol) associated with substituting $n$ water molecules in low coordination clusters, and in 6-fold Mg-water clusters with $n$ methyl acetates (MeAcs) or $n$ diethyl phosphates (DEPhs). Substitution energies are defined in equation 4.2.	72
4.4	Shifts in substitution energies relative to LB Rules: $\Delta E_{\text{sub}}^{202X} - \Delta E_{\text{sub}}^{\text{LB}}$ for 2024 and 2025, and their difference [2025–2024]. Positive values mean 202X is less stabilizing (less negative) than LB; negative values mean more stabilizing than LB.	73
4.5	Bilayer structural parameters	76
4.6	$2D_C$ and $A_L$ from acyl chain ordering	85

## List of Figures

2.1	Representative Nelder–Meade (NM) optimization run.	15
2.2	Substitution energies for $\text{Na}^+$ clusters	19
2.3	Distances from $\text{Na}^+$ to each component atom in sample clusters	32
2.4	Electron densities of the simulated bilayers	33
2.5	Lipid chain deuterium order parameters.	34
2.6	Number of ions bound to the lipid bilayer	35
2.7	$\text{Na}^+$ inner shell coordination partners	36
2.8	Water density at the bilayer interface	37
2.9	Water orientational order parameters	38
2.10	Bilayer electrostatic potential	39
2.11	Poisson-Boltzmann theory predictions and simulation results.	40
3.1	Substitution energies of $\text{Li}^+$ from solvent to ligands	45
3.2	Geometries of $\text{Li}^+$ clusters with ligands	45
3.3	Comparison of SAXS formfactors	48
3.4	Acyl chain order parameters	50



3.5	Water orientational order parameters	52
3.6	Number densities	56
3.7	Number densities of cations and anions	57
3.8	Electrostatic potential	58
3.9	First shell coordinators for $\text{Li}^+$ and $\text{Mg}^{2+}$	61
3.10	Fractions of ion-adsorption modalities	62
4.1	Geometry of optimized clusters of small molecules	70
4.2	Water orientational order parameters	75
4.3	First-shell coordination partners of $\text{Mg}^{2+}$	77
4.4	Fraction of ions in each adsorption modality	79
4.5	SAXS formfactors	81
4.6	Number densities	82
4.7	Acyl-Chain order parameters	84
4.8	Adsorbed charge per adsorption modality	86

## Abstract

# 1 Introduction<sup>1</sup>

## 1.1 Phospholipid bilayers

Phospholipid bilayers are the primary component of the major delimiting boundary between cells and their environment. These membranes are not static walls so much as liquid-crystalline, rapidly exploring their conformational space and adjusting to the external and internal cellular environment. Cells, through the diversity of chemistry of headgroups and acyl-chain selections, tailor the dynamic structure of their membrane to further adapt to the environment around them. Understanding the way that individual lipid species contribute to the structure of a lipid bilayer is critical to understand why a cell might choose one lipid or another in their cell membrane. Additionally, because these lipids are exposed to complex mixtures of ions on either side of the membrane, the interactions with ions in solution cannot be ignored when discussing the bilayer structure. Experimentally observed ion behavior at an interface in solution has been explained using a mean-field model nearly 100 years ago.<sup>?</sup> However, this ignores specific chemical interactions between lipid molecules and the ions in the solvent, that are critical for understanding the effect of changing headgroup species in a membrane. Computational models can enable researchers to observe the specific ion-lipid interactions are critical for understanding of why cells might choose certain lipids to manipulate their membrane structure under varied ion mixtures in their environment. Furthermore, this changing membrane structure also affects the behavior of membrane proteins embedded in the bilayer. Thus, this manipulation of the lipid mixture presents itself as an important regulatory mechanism for cells.

---

<sup>1</sup>Portions reprinted with permission from Matthew Saunders, Vered Wineman-Fisher, and Eric Jakobsson, *High-Dimensional Parameter Search Method to Determine Force Field Mixing Terms in Molecular Simulations*, *Langmuir*, American Chemical Society, March 1, 2022. and from Matthew Saunders, Abibat Adekeye-Olowofela, and Sabrina Downing, *Adsorption Modes of  $\text{Na}^+$ ,  $\text{Li}^+$ , and  $\text{Mg}^{2+}$  to a Model Zwitterionic Lipid Bilayer*, *Langmuir*, American Chemical Society, December 1, 2024.

## 1.2 Molecular Simulations

### 1.2.1 Classical Molecular Dynamics

Molecular Dynamics utilizes computers to simulate systems of molecules in order to study how structure changes with time, and the specific ways that different atomic and molecular species interact. This is done by first creating a model for the Hamiltonian of the system – a "force-field". This consists firstly of the terms for how atoms bond to each other, how these bonds move and stretch, and how they rotate around each other; classical models usually use harmonic potentials for bond and angle stretching and bending, and dihedrals are described using periodic functions.<sup>1</sup> In addition to the bonded terms, we have the non-bonded terms — energy from electrostatic interactions, typically described by Coulomb's law, and dispersion interactions (Van der Waals, or VdW) which arise from instantaneous dipole-induced dipole effects.<sup>1</sup> These are most often modeled using a Lennard-Jones (LJ) potential,<sup>1,2</sup> though other forms are also common, such as the Buckingham (exp-6) potential,<sup>1,3</sup> which replaces the steep  $r^{-12}$  repulsive wall with a short-range exponential. In addition to these two, there are many other functional forms used to describe VdW and dispersion interactions, but they are far less common. An example of this Hamiltonian can be seen here:

$$E_{\text{total}} = E_{\text{bonded}} + E_{\text{nonbonded}} \quad (1.1)$$

$$E_{\text{bonded}} = \sum_{\text{bonds}} k_r (r - r_0)^2 + \sum_{\text{angles}} k_\theta (\theta - \theta_0)^2 + \sum_{\text{dihedrals}} V_n [1 + \cos(n\phi - \gamma)] \quad (1.2)$$

$$E_{\text{nonbonded}} = \sum_{i < j} \left[ 4\epsilon_{ij} \left( \left( \frac{\sigma_{ij}}{r_{ij}} \right)^{12} - \left( \frac{\sigma_{ij}}{r_{ij}} \right)^6 \right) + \frac{q_i q_j}{4\pi\epsilon_0 r_{ij}} \right] \quad (1.3)$$

By using this set of terms one can compute the potential energy of a particular configuration of particles. The forces obtained from the potential energy are used in Newton's equations of motion, which are numerically integrated — most often with algorithms such as the velocity-Verlet method — to update positions and velocities at each time step.<sup>1</sup> The energy of the new configuration can be computed, and the simulation continues. Thus, the

Careful development and improvement of a force-field is critical to reproduce valid results that can help us understand what is seen in experiments.

### 1.2.2 Mixing rules, and NB-fix

Focusing in particular on the non-bonded terms of the hamiltonian, and specifically the Lennard-Jones (LJ) function, we note that there are two free parameters  $\sigma_{ij}$  and  $\epsilon_{ij}$  between a particular pair of particles  $i$  and  $j$ :

$$E_{\text{LJ}_{ij}} = 4\epsilon_{ij} \left( \left( \frac{\sigma_{ij}}{r_{ij}} \right)^{12} - \left( \frac{\sigma_{ij}}{r_{ij}} \right)^6 \right) \quad (1.4)$$

Where  $r_{ij}$  is the distance between the two particles,  $\sigma_{ij}$  is the characteristic distance of the Van der Waals interaction between the two species, and  $\epsilon_{ij}$  is the characteristic energy of the interaction. These parameters are generally determined for a particular species for the case of the self-interaction, or  $\sigma_{ii}$  and  $\epsilon_{ii}$ . In this case, they represent roughly the atomic radius, and the “stickyness” of the particle. These can then be combined with the  $\sigma_{jj}$  and  $\epsilon_{jj}$  from another species by using what are called mixing rules, developed to model the interaction radii and energy well-depth for interacting species.<sup>4,5</sup> The Lorentz rule for computing the  $\sigma_{ij}$  is simply the arithmetic mean of the self terms from the two species, and the Berthelot rule for computing the  $\epsilon_{ij}$  is the geometric mean of the self terms. Modern works have often reported that these mixing rules fail or behave unpredictably for more complicated species than the noble gases,<sup>6,7</sup> and abandonment of the mixing rules for specifically selected cross-terms can be beneficial to improving force-fields.<sup>8-18</sup> This kind of correction is often called a "non-bonded fix" or NB-fix, which is a correction to the cross-terms of the species of interest in order to improve the reproduction of some experimental result. In this dissertation, I expand on the idea of a NB-fix method to improve the modeling of the interactions of ions and phospholipid species. However, the method proposed and characterized is general, and can be applied to other chemically diverse systems of interest.

## MD methods utilized in this dissertation

In the following dissertation, unless otherwise specified, I perform all molecular dynamics simulations with the GROMACS software package.<sup>19–24</sup> I use the SPC/E model for all waters,<sup>25</sup> and I describe lipid interactions with the gromos43A1-S3 parameter set developed by our group in previous work.<sup>26</sup> System temperature is maintained at 300 K using the Nosè–Hoover thermostat with a coupling constant of 0.5 ps,<sup>27</sup> and pressure is maintained at 1 atm with the Parrinello–Rahman semiisotropic barostat using a coupling constant of 1.5 ps.<sup>28</sup> All bonds are constrained with the P-LINCS algorithm, which allows the use of a 4 fs integration timestep.<sup>29</sup> Equations of motion are integrated with the Verlet scheme, and neighbor lists are updated every 2 steps. Electrostatic interactions are treated with the particle–mesh Ewald (PME) method,<sup>30</sup> using a real–space cutoff of 1.6 nm and reciprocal grids of either  $56 \times 56 \times 224$  or  $52 \times 52 \times 240$  cells, together with 4th order B-spline interpolation. Van der Waals interactions are calculated with a single cutoff of 1.6 nm.

## Simulation system construction

All simulations systems unless otherwise noted are constructed by first creating a leaflet of 100 POPC lipids arranged on a  $10 \times 10$  grid with sufficient spacing to avoid chain overlap. This leaflet is then reflected along the  $z$ -axis to generate the second leaflet, producing a bilayer of 200 lipids. A solvent block is added by placing 60,000 water molecules on a three–dimensional grid with excess spacing, and a subset of water molecules is randomly replaced with ions to achieve a starting concentration of 200 mM (see Table 3.1).

Energy minimization is performed using the steepest–descents algorithm with a force tolerance of  $50 \text{ kJ mol}^{-1} \text{ nm}^{-1}$ . Electrostatic interactions are treated with the particle–mesh Ewald (PME) method,<sup>30</sup> using a real–space cutoff of 1.6 nm, reciprocal grid spacing of  $0.12 \text{ nm}^{-1}$ , and 6th order B-spline interpolation. Van der Waals interactions are calculated with a single cutoff of 1.6 nm. Neighbor searching is performed every 2 steps.

Following energy minimization, I relax the system with a constant-pressure simulation at 290 K for 200 ps. Simulation systems are then annealed by heating the system above the simulation run temperature, and then cooling down to the production temperature following the specific procedure outlined in each following chapter.

### 1.2.3 *Ab initio* calculations and Density Functional Theory

Classical force-fields are effective for simulating large-systems of particles where an explicit description of the electronic behavior is not critical to the understanding of how the particles behave – while this is a major approximation, it turns out to often be useful in studying biological structures like lipid membranes.<sup>31</sup> However, when preparing these classical models, we need to refer to more complicated theory in the form of quantum mechanical calculations to set terms like the charge per particle in a molecule and to compare to the molecular structure predicted by our bonded-parameters. *Ab initio* quantum mechanical calculations include chemistry by explicitly describing the behavior of electrons to varied levels of accuracy depending on the kind of functional form used, and then the basis vectors used to describe the space. Perturbation theory methods include electron correlation, which can be useful for assigning electrons to parts of a molecule. However, these methods quickly become expensive for systems with many electrons. Density functional theory, which treats the electrons with a mean-field approximation is often more computationally efficient and can thus be applied to larger systems.

*Ab initio* methods are used in the works included in this dissertation to generate target data for model parameter optimization from geometry optimizations and substitution energies of small ion–ligand clusters using density functional theory (DFT) as implemented in FHI-aims.<sup>32</sup> Initial cluster geometries are produced with the molecular mechanics force field developed in our previous work<sup>33,34</sup> and then optimized at the DFT level. I use the PBE0 functional<sup>35,36</sup> with Tkatchenko–Scheffler dispersion corrections,<sup>37</sup> a combination that has been benchmarked for ion–ligand clusters and shown to reproduce experimental data and

high-level quantum methods across a range of chemistries.<sup>18,38,39</sup> Geometry optimizations are first performed with the “light” basis set and then refined with the “really tight” basis set provided in FHI-aims. Optimizations are converged to 0.005 eV/Å in forces and  $10^{-6}$  eV in total energy.

Energies of optimized clusters are then used to compute substitution energies, defined as the energy of exchanging water molecules with headgroup analog ligands. The specific cluster sets and substitution energy targets used for parameterization are described in the relevant chapters.

### **1.3 Comparing Molecular Simulations with Experimental Results**

#### **1.3.1 SAXS (and SANS) – and other properties obtained from density distributions**

Systems of crystals are often studied using diffraction or scattering experiments. In the case of lipid bilayers, we often use Small-Angle scattering of x-rays (SAXS) or neutrons (SANS) to study the bilayer structure. Lipid bilayers are smectic crystals, and thus give scattering patterns that look like concentric circles – these circles are the bilayer form-factor.<sup>40</sup> This form-factor is the reciprocal-space structure of the bilayer, but phase information of each lobe is lost. Thus, a simple reverse-transformation cannot be performed. In order to produce the appropriate density distribution, one can approximate the number density of bilayer parts as gaussian functions, and compute the appropriate scattering density from that.<sup>40,41</sup> This can then be transformed via a cosine transform into a form-factor. The gaussians are then adjusted until the resulting continuous form-factor fits the data from the experiment.<sup>40,41</sup> In simulations, we can compute the number density histograms of the system components directly from the trajectories, and thus the electron densities directly. Once we have the electron density of our system per nanosecond, we determine the lipid bilayer centerpoint by locating the minimum at the center of the histogram. We symmetrize the histogram around the minimum at the center, and then take an average over many nanoseconds. We subtract the bulk solvent value of the electron density from the average histogram, and



then use a cosine transform to obtain the bilayer SAXS form-factor. This can be compared with the experimental data directly. We also use the electron density to directly obtain the peak-to-peak distance of the bilayer,  $D_{\text{hh}}$ , as one measure of the bilayer thickness.

### 1.3.2 Number density histograms

The number density histograms are also used to compute the various bilayer thicknesses via probability densities of the various system components. We compute

### 1.3.3 Lipid component volumes

Phospholipid headgroup and chain occupied volumes are computed using the method of Petrache *et al.* for computing the volume of immiscible liquids.<sup>42</sup> In the work outlined in this dissertation, we identify lipid chains as starting at the first carbon attached to the lipid chain carbonyl oxygen, including the oxygen. The atom groups not part of the lipid chains are partitioned into the headgroup volume. The number-density of these component groups along with that of the solvent are taken and used to optimize the objective function:

$$\Omega(v_i) = \sum_{z_j}^{\rho_s} \left( 1 - \sum_{i=1}^{N_{\text{Groups}}} (\rho_i(z_j) v_i)^2 \right), \quad (1.5)$$

In the equation above,  $\rho_i(z_j)$  is the number density of the  $i$  component in the  $z_j$  slice of the box and  $v_i$  is the corresponding component volume. The component volumes are then multiplied by the corresponding number of particles per molecule per group – 32 for the chain particles, and 20 for the headgroup. This gives us the total volume per molecule for each group, defined as  $V_{\text{H}}$  and  $V_{\text{C}}$ . These are then added together to make the total  $V_{\text{L}}$ .

### 1.3.4 Electrostatic and dynamic results... such as GC-theory!

### 1.3.5 Diffusion coefficients

### 1.3.6 Order parameters

## 2 A high dimensional parameter search method to determine force field mixing terms in molecular simulations<sup>1</sup>

### 2.1 Abstract

Molecular dynamics (MD) force fields for lipids and ions are typically developed independently of one another. In simulations consisting of both lipids and ions, lipid-ion interaction energies are estimated using a predefined set of mixing rules for Lennard-Jones (LJ) interactions. This, however, does not guarantee their reliability. In fact, compared to the quantum mechanical reference data, Lorentz-Berthelot mixing rules substantially underestimate binding energies of  $\text{Na}^+$  ions with small molecule analogues of lipid headgroups, yielding errors on the order of 80 and 130 kJ/mol, respectively for methyl acetate and diethyl phosphate. Previously, errors associated with mixing force fields have been reduced using approaches like ‘NB-fix’ in which LJ interactions are computed using explicit cross terms rather than those from mixing rules. Building on this idea, we derive explicit lipid-ion cross terms that also may implicitly include many-body cooperativity effects. Additionally, to account for interdependency between cross terms, we optimize all cross terms simultaneously by performing high-dimensional searches using our ParOpt software. The cross terms we obtain reduce the errors due to mixing rules to below 10 kJ/mol. MD simulation of lipid bilayer conducted using these optimized cross terms resolve the structural discrepancies between our previous simulations and small-angle X-ray and neutron scattering experiments. These results demonstrate that simulations of lipid bilayers with ions that are accurate up to structural data from scattering experiments can be performed without explicit polarization terms. However, it is worth noting that such NB-fix cross terms are not based on any physical

---

<sup>1</sup>Portions reprinted with permission from Matthew Saunders, Vered Wineman-Fisher, and Eric Jakobsson, *High-Dimensional Parameter Search Method to Determine Force Field Mixing Terms in Molecular Simulations*, *Langmuir*, American Chemical Society, March 1, 2022. © 2022 American Chemical Society.

principle; a polarizable lipid model would be more realistic, and is still desired. Our approach is generic and can be applied to improve accuracies of simulations employing mixed force fields.

## 2.2 Introduction

Cellular membranes function as highly dynamic interfaces with many diverse components, including lipids, peptides, carbohydrates, and charged species like ionic salts. Studies of these complex systems often benefit from computational methods, particularly molecular dynamics (MD) simulations.<sup>31</sup> In our previous MD simulation studies, we characterized the effects of various monovalent and divalent ions on model 1-palmitoyl-2-oleoyl-sn-glycero-phosphatidylcholine (POPC) bilayers.<sup>33,34,43,44</sup> We reported that ions modify POPC bilayer structure with significant effects on area per lipid and bilayer thickness. Similar results were also reported in MD simulations by others.<sup>45–49</sup> Experiments characterizing bilayer structures in the presence of ions have not been as numerous as simulation studies. However, experimental findings indicate that dissolved salts at physiological concentrations do not modify bilayer structure significantly.<sup>50–52</sup> Specifically, Petrache *et al.* performed small angle X-ray scattering (SAXS) experiments on multilamellar vesicles of 1,2-dilauroyl-sn-glycero-3-sn-glycero-phosphatidylcholine as well as other lipids in KCl and BrCl salt solutions, and reported that while small changes can be seen in the X-ray scattering form-factor due to the salts, the fitted electron density profiles are essentially identical for systems with and without salt.<sup>51</sup> Similarly, Pabst *et al.* found no significant change in bilayer structure for POPC bilayers in NaCl salt at or below 1 M concentration.<sup>50</sup> Furthermore, Uhrikova *et al.* reported small structural changes using small angle neutron scattering (SANS) experiments on 1,2-dipalmitoyl-sn-glycero-3-sn-glycero-phosphatidylcholine vesicles interacting with  $\text{CaCl}_2$ .<sup>52</sup> Taken together, these results point to a general discrepancy between structural data from MD simulations and scattering experiments.

The reliability of MD simulations depends greatly on the force field (FF) parameters used for describing intra- and inter-molecular interactions. While FF parameters of lipids,

including ours, are developed with great accuracy and care, we note that they are derived in the absence of ions. Similarly, ion parameters are also derived in the absence of lipids.<sup>53</sup> When simulations of bilayers are conducted in salt solution, ion-lipid interactions are computed using FF mixing rules. In our previous MD simulations of POPC bilayers in salt solutions, we employed our gromos43A1-S3 lipid FF parameters<sup>26</sup> that were developed for use with SPC/E water to determine lipid-lipid and lipid-water interactions. Ion-ion and ion-water interactions were described using Joung and Chetham<sup>53</sup> parameters, also developed for use with SPC/E water. Lipid-ion interactions were estimated using Lorentz-Berthelot (LB) mixing rules for Lennard-Jones (LJ) components, and there was a significant change in bilayer structure compared to that of the bilayer without salt despite the relatively small initial salt concentration of 200 mM. Does this suggest that the discrepancy between our MD predictions and experiments is the result of the LB mixing rules? Note that none of the MD simulations of lipid-ion interactions discussed above include explicit terms to describe electronic polarization. Errors in mixing rules may, therefore, emerge if the high electric fields of ions induce cooperativity effects in lipid groups differently from those in water. Quantum mechanical (QM) studies, in fact, suggest that many-body cooperativity effects, such as polarization depend strongly on ion-coordinator chemistry.<sup>18,54</sup> It has also been postulated that these effects, and specifically electronic polarization may play an important role in determining the structure and dynamics of lipid bilayers – especially when interacting with ions.<sup>55–59</sup>

Small deviations from LB rules have been shown to have a significant effect on the behavior of systems of particles,<sup>7</sup> and it is possible that a systematic tuning of these parameters could be used to correct for artifacts in a simulation.<sup>8–18</sup> Such a ‘Non-Bonded-fix’ (NB-fix) strategy has been shown to effectively improve protein-ion, protein-nucleotide, and ion-membrane interactions while retaining the commonly used form of the LJ 6-12 potential.<sup>8–18</sup> Building on this idea, here we propose a more general approach to optimize interaction cross terms for use with the 6-12 potential, and also validate its prediction in condensed

phase simulations. We expand on the NB-fix method by (a) optimizing all ion-lipid LJ cross terms simultaneously, and (b) implicitly including many-body cooperativity effects. We consider simultaneous optimization of all cross terms to be critical, because of their strong, interdependent correlation with the target results.<sup>60</sup> This high-dimensional optimization is performed using our software tool ParOpt.<sup>60,61</sup> Many-body cooperativity effects have been shown to be a major contributor to ion binding<sup>54</sup>. Thus, it is important to include them in lipid bilayer simulations where ions are known to coordinate simultaneously with multiple ligands.<sup>44</sup>

We show that the cross terms we obtain from this approach substantially improve ion-lipid interaction energies over those obtained from LB mixing rules. MD simulation of a POPC bilayer in 200 mM NaCl initial solution conducted using these optimized cross terms also resolves the structural discrepancies between our previous MD simulations and small-angle X-ray and neutron scattering experiments at low salt concentrations.

### 2.3 Methods

The method proposed here is generic and can be applied to any pair of interacting species that use cross terms, and ensures that we are reproducing macroscopic results based on the most accurate representation of the local inter-molecular interactions. We chose small molecular analogues of the important ion binding sites in the polar region of phospholipid molecules. These molecules were also used as building block molecules in development of our lipid FF.<sup>26,33</sup> Specifically, we selected methyl-acetate (MeAc) to represent the ester group binding the acyl-chain to the glycerol backbone, and diethyl-phosphate (DePh) to represent the headgroup phosphate and surrounding carbons (See insert on figure 2.2). The overall goal was to take the substitution energy of ions from water to the selected molecules, along with the corresponding geometries, all computed using a benchmarked quantum mechanical framework, and optimize the interaction cross terms to reproduce these target data within the Molecular Mechanics force-field.

Combined analysis of results from experiments and *ab initio* molecular dynamics simulations in the aqueous phase suggest that  $\text{Na}^+$  ions prefer to directly coordinate with  $\sim 5 - 6$  water molecules.<sup>62-66</sup> However, when coordinating with MeAc molecules, steric hindrance restricts the number of binding partners to fewer than four coordinating molecules. Thus, we limited the size of our MeAc clusters to up to four molecules around an ion. DePh has resonant oxygens on each molecule that potentially act as two binding sites, so we limited these clusters to up to two molecules around a  $\text{Na}^+$ . These were compared to the clusters of  $\text{Na}^+$  surrounded by up to four water molecules. In this work, we forgo modifying terms for  $\text{Cl}^-$ , as we have found in our previous work that anions do not bind to the bilayer headgroup significantly, and remain solvated by water molecules.<sup>33</sup>

### 2.3.1 Quantum Mechanical Calculations

For this work, I compute target data for parameter optimization from geometry optimizations and substitution energies of  $\text{Na}^+(\text{Water})_n$ ,  $\text{Na}^+(\text{MeAc})_n$  ( $n \leq 4$ ), and  $\text{Na}^+(\text{DePh})_m$  ( $m \leq 2$ ) clusters. Substitution energies are defined as the energy cost of replacing water molecules with methyl acetate (MeAc) or diethyl phosphate (DePh) ligands:

$$\begin{aligned} E_{\text{MeAc}}^n &= E_{\text{Na}^+(\text{MeAc})_n} - nE_{\text{MeAc}} - E_{\text{Na}^+(\text{Water})_n} + nE_{\text{Water}} \\ E_{\text{DePh}}^n &= E_{\text{Na}^+(\text{DePh})_n} - nE_{\text{DePh}} - E_{\text{Na}^+(\text{Water})_{2n}} + 2nE_{\text{Water}}. \end{aligned} \tag{2.1}$$

The QM total energies and self-energies used in these calculations are reported in Tables 2.1 and 2.2. These values, together with the corresponding optimized configurations, serve as the target data for the parameter optimization in this chapter.

### 2.3.2 Parameter Optimization

Parameter optimization is performed using our ParOpt software package.<sup>60,61</sup> This software is available for download at <https://csmllabfs1.cas.usf.edu/Sites>. We utilized the Nelder-Mead method to perform a search to simultaneously optimize all  $\sigma_{ij}$  and  $\epsilon_{ij}$  cross

Table 2.1: Total energies of systems of small molecules from QM calculations. These energies are computed by taking the total energy from the final step of geometry optimization on clusters of our selected small molecules around a single  $\text{Na}^+$  following the procedure outlined in the methods section. We computed binding energies using these values.

Cluster Size	Water (kJ/mol)	MeAc (kJ/mol)	DePh (kJ/mol)
1	$-9.048 \times 10^5$	$-1.130 \times 10^6$	$-2.528 \times 10^6$
2	$-1.609 \times 10^6$	$-1.834 \times 10^6$	$-4.630 \times 10^6$
3	$-2.313 \times 10^6$	$-2.538 \times 10^6$	N/A
4	$-3.018 \times 10^6$	$-3.243 \times 10^6$	N/A

Table 2.2: Self energies of isolated molecules. These are computed by performing geometry optimization on an isolated molecule following the procedure outlined in the methods.

	Water	$\text{Na}^+$	MeAc	DePh
Energy (kJ/mol)	-2.006E+05	-4.253E+05	-7.042E+05	-2.102E+06

terms of  $\text{Na}^+$  ions with MeAc and DePh molecules. Specifically, there are seven atom types in these two small molecules (table 2.4), and so all 14 cross terms for the 6-12 LJ potential are optimized. Error was determined by comparing the optimized geometries and substitution energies of each new parameter set to the reference data from QM.

Boundary constraints are imposed on  $\epsilon_{ij}$  and  $\sigma_{ij}$  to keep the search space finite. Table 2.5 shows all of the constraints placed on the parameter search. Additionally, constraints are applied to keep the NA-OM  $\sigma_{ij}$  to be smaller than the  $\sigma_{ij}$  for NA-P to avoid unphysical conformations of DePh. Boundary constraints are enforced by reassigning  $\sigma_{ij}$  or  $\epsilon_{ij}$  values

Table 2.3: Nelder–Meade constraints. These values were used to constrain the parameter search space during the NM-optimization.

	NA-CH3		NA-CH2		NA-CO*		NA-OA,-OM*,-O*,-P		Additional Con-straints
	Min	Max	Min	Max	Min	Max	Min	Max	N/A
$\sigma_{ij}$ (nm)	0.2	0.5	0.2	0.5	0.2	0.5	0.2	0.5	$\sigma_{ij}^{\text{NA-OM}^*} \leq \sigma_{ij}^{\text{NA-P}}$
$\epsilon_{ij}$ (kJ/mol)	0	0.79	0	0.81	0	0.83	0.05	7	N/A

that violate the bound to the boundary value. Throughout optimization, constraint violations are monitored to ensure that a final parameter set that is the result of a constraint violation is not selected. High-dimensional optimizations of this nature may not have a unique solution; thus, 200 independent optimizations are performed, each initialized with random initial parameter values. Parameter sets that best improved the substitution energy without significantly compromising the conformational geometries are compared to select the final parameters that are used in the present work.

Figure 2.1a illustrates a representative NM-trajectory that follows NM-error as a function of optimization step. In this case, the NM-error is defined as an equally-weighted combination

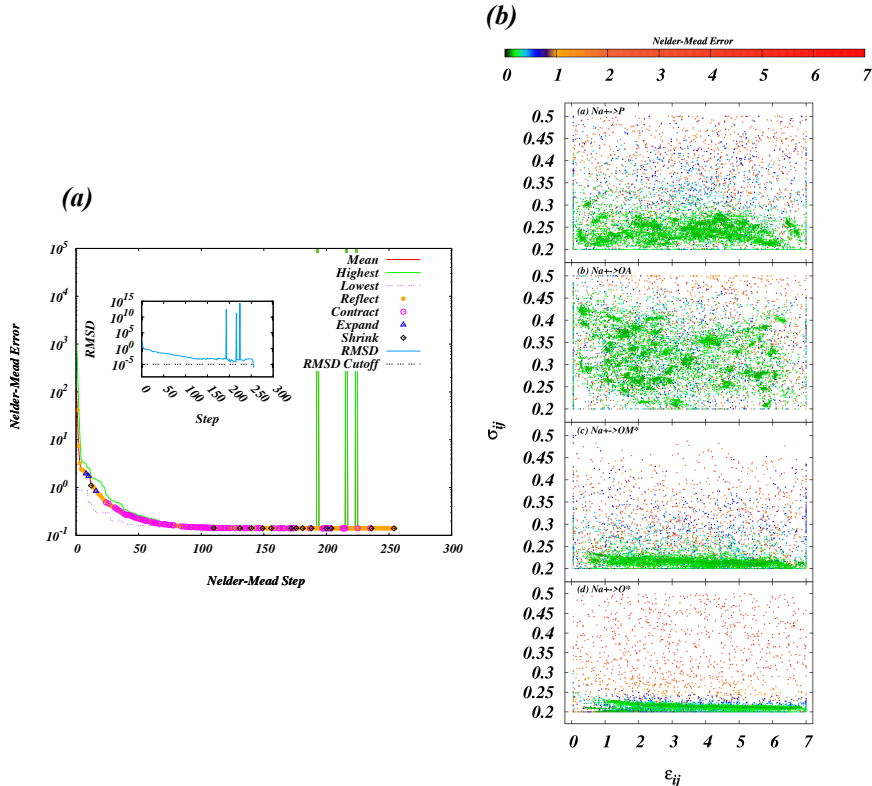


Figure 2.1: (a) Representative Nelder-Mead (NM) optimization run. Each point represents a move that the NM simplex can make while navigating the parameter space (See Fogarty *et al.* for a full description of the Nelder-Mead algorithm and available moves<sup>60</sup>). The insert illustrates the RMSD between the simplex vertices. The optimization is considered converged when the simplex collapses, which is defined by an  $\text{RMSD} \leq 10^{-10}$ . (b) Map of all  $\sigma_{ij}$  and  $\epsilon_{ij}$  tested for interactions of Na<sup>+</sup> with non-carbon atom types in the 200 optimizations performed to find our final optimized set of cross terms. A total of 291,870 combinations of parameters were tested, shown color-coded according to their NM error.



of the mean absolute error of the substitution energy and the distances between each atom in the cluster and the  $\text{Na}^+$  ion. Each NM-move used is illustrated as a point on the error curve (see Fogarty *et al.* for complete description of NM algorithm and moves<sup>60</sup>). The insert shows the root-mean squared distance (RMSD) between the simplex vertices at each step. As is typical with the NM method, error drops exponentially during the initial steps, and slows down towards the end of the optimization process. The termination condition for the optimization run is the collapse of the NM-simplex (defined by the  $\text{RMSD} \leq 10^{-10}$ ). Figure 2.1b shows all of the 291,870  $\sigma_{ij}-\epsilon_{ij}$  pairs tested between  $\text{Na}^+$  ions and the non-carbon atoms in the 200 independent optimization runs, and provides a visual perspective of the sampled parameter space. The parameter set that yielded the lowest error, as discussed in the results section, was chosen to perform MD simulations of a POPC bilayer.

### 2.3.3 Bilayer Construction

Simulation systems are constructed following the method outlined in chapter 1. Based on a conservative estimate of one binding site per lipid, at least 200  $\text{Na}^+$  ions are required in bulk solvent to avoid depletion during equilibration. To achieve this, I double the solvent block size used in our previous work,<sup>33,44</sup> adding 60,000 waters to the system on a three-dimensional grid and randomly replacing water molecules with 216  $\text{Na}^+$  and 216  $\text{Cl}^-$ . This corresponds to an initial concentration of 200 mM, similar to our previous simulations, and yields a simulation box with initial dimensions of  $9.75 \times 9.75 \times 59.84 \text{ nm}^3$ . Following energy minimization as described in Chapter 1, the system is relaxed with a short NPT equilibration at 290 K and annealed by heating to 350 K and cooling in 10 K steps to the production temperature of 300 K (155 ps per step).

Following energy minimization and annealing, the box dimensions shrink to  $7.97 \times 7.97 \times 32.14 \text{ nm}^3$ . This final structure is used as the starting point for production simulations.

### 2.3.4 Molecular Dynamics

Trajectories are simulated continuously for 0.7  $\mu$ s to match the simulation length of Kruczek *et al.*<sup>33,44</sup> Trajectory analysis is performed using a combination of GROMACS built-in tools and in-house software developed on the GROMACS API.

## 2.4 Results and Discussion

### 2.4.1 Optimized Cross-Terms

The final optimized parameters are detailed in table 2.4 alongside the original parameters computed using LB rules. One can immediately note a general trend of an increase in the value

Table 2.4: Force-field cross terms. Original terms, as used in the system simulated with LB rules were computed by applying Lorentz-Berthelot mixing rules to the LJ parameters of Na<sup>+</sup> and each lipid component atom type. Optimized parameters are the result of the NM-optimization using ParOpt.<sup>60,61</sup> All constraints on the search space can be seen in figure 2.5

	Original		Optimized	
	$\sigma_{ij}$ (nm)	$\epsilon_{ij}$ (kJ/mol)	$\sigma_{ij}$ (nm)	$\epsilon_{ij}$ (kJ/mol)
NA-CH3	0.295	1.100	0.235	0.700
NA-CH2	0.312	0.772	0.237	0.809
NA-OA	0.256	1.120	0.211	3.035
NA-P	0.277	1.900	0.301	0.483
NA-OM*	0.252	1.221	0.211	1.445
NA-CO*	0.335	0.362	0.315	0.758
NA-O*	0.251	1.221	0.216	2.440

of  $\epsilon_{ij}$  for the non-carbon atom types. With the constraints on the carbon atoms, parameters have been nudged into gaining the binding energy by increasing the  $\epsilon_{ij}$  for the specifically electronegative atoms. Values of  $\sigma_{ij}$  have changed, but remained close to the original values in general, suggesting that the optimum distance to the minimum energy of the LJ potential is estimated well by LB rules. We can also see that no values of  $\sigma_{ij}$  or  $\epsilon_{ij}$  violate the constraints described in table 2.5. Substitution energies and corresponding conformational

Table 2.5: Nelder–Meade constraints. These values were used to constrain the parameter search space during the NM–optimization.

	NA-CH3		NA-CH2		NA-CO*		NA-OA,-OM*,-O*,-P		Additional Con- straints
	Min	Max	Min	Max	Min	Max	Min	Max	N/A
$\sigma_{ij}$ (nm)	0.2	0.5	0.2	0.5	0.2	0.5	0.2	0.5	$\sigma_{ij}^{\text{NA-OM}^*} \leq \sigma_{ij}^{\text{NA-P}}$
$\epsilon_{ij}$ (kJ/mol)	0	0.79	0	0.81	0	0.83	0.05	7	N/A

geometries are examined by running energy minimization of the QM–optimized structures using the final parameter set. These are then analyzed using the GROMACS built–in energy and distance tools. The substitution energies and the conformations for this parameter set are shown in figure 2.2 and in figure 2.3, respectively. It can be noted that for MeAc we have substantially improved substitution energies relative to those obtained from using LB mixing rules, which started with an discrepancy of around 30–80 kJ/mol. The optimization has also improved the relative substitution between the clusters of various sizes. The substitution energies for DePh have also improved by a similar magnitude. The conformational geometries are largely unchanged, with a general trend of the binding distance to OM shrinking on the order of 0.25 Å in DePh. This shrinkage is common when optimizing both energies and conformations with the relatively small number of free parameters corresponding to the LJ cross terms.<sup>18</sup>

Notably, the substitution energies for both molecule types improve more in the larger cluster sizes. Larger clusters are more relevant to the dense environment in the lipid headgroup region of the bilayer, as few, if any, ions bind to a single lipid at a time.<sup>33</sup> Furthermore, the substitution energy profile for MeAc has become much closer to that of the QM profile. Thus, these new parameters substantially improve the energetic balance between the lipid–ion, lipid–water and ion–water interactions.

The conformational geometries were mostly unchanged with the new parameter set, as even the original parameters do a good job in reproducing the QM–configurations. The least precise cluster appears to be for 4 MeAc, where the original LB parameters poorly

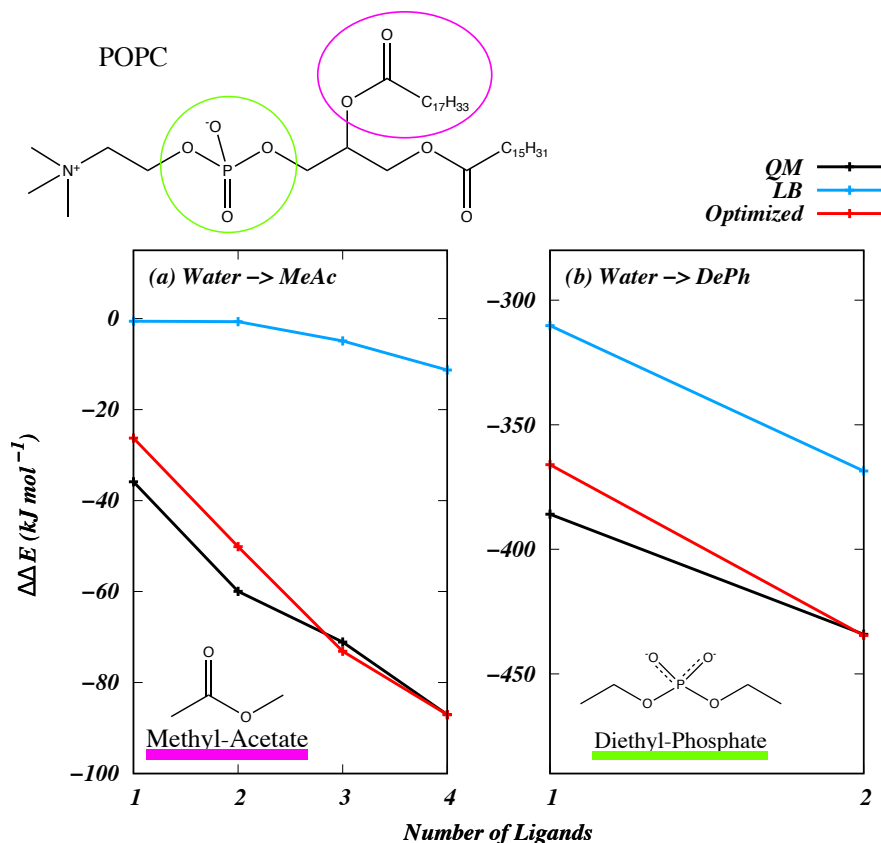


Figure 2.2: Substitution energies for  $\text{Na}^+$  clusters computed as described in equation 2.1. The energies of systems computed using the standard mixing rules are shown in black, the energies from benchmarked DFT are in red, and in blue are the optimized results. There is a significant error with the standard LB mixing rules, which is substantially improved with the new optimized cross terms. The insert shows a diagram of POPC, and the small molecules Methyl-Acetate (MeAc) and Diethyl-Phosphate (DePh) that were used to represent the major  $\text{Na}^+$  interaction sites on the POPC molecule.

represent the symmetries exhibited in the QM data. Even with the improvement from our new parameters, we may be missing behavior from explicit polarization effects that cannot be captured properly by a non-polarizable model.<sup>54</sup>

## 2.4.2 Validation of Parameters

In order to characterize our new parameter set in a bilayer, I generated a 700 ns simulation of a bilayer of POPC lipids in NaCl salt solution, and the results are compared against a similar system simulated using LB rules in previous work.<sup>33,44</sup> These older trajectories for systems both with salt and without will be referred to, respectively, as LB and ‘without salt.’

New simulations are performed with optimized cross terms, hence forth will be referred to as the ‘optimized’ system, long enough to equilibrate the number of bound ions (see figure 2.6). This ion binding is further characterized in a subsequent section.

## Bilayer Structure

Bilayer structural parameters can be seen in table 2.6. The phospholipid component

Table 2.6: Bilayer structural parameters.  $D_{hh}$  is the peak-to-peak distance from the electron density of the lipid bilayer, and is a measure of bilayer thickness. Bilayer thickness  $D_B$  and chain thickness  $2D_C$  are computed from number densities of the solvent and the lipid chains, respectively.  $V_H$ , and  $V_C$  are the volumes of the headgroup and lipid chains computed using the method from Petrache *et al.*<sup>42</sup>  $V_L$  is the sum of  $V_H$  and  $V_C$ . Rows 7-11 contain kinetic parameters for ion binding to membrane. These parameters come from fitting the equation  $N_b(t) = \frac{K_a}{K_a + K_d} N (1 - \exp[-(K_a + K_d)(t - t_0)])$  to the data for the number of ions bound to the lipid bilayer across the simulation time.  $A$  is the asymptotic number of ions bound to the lipid bilayer, and can be used as the expected number of ions that will bind to the system at equilibrium.  $\tau$  is the characteristic timescale of the fitted function.  $n_0$  is the number of ions bound at the beginning of the production run of the simulation.  $K_D$  and  $K_A$  are the computed binding association and dissociation constants, and  $K_A/K_D$  is the binding rate constant.

	Without salt	LB	Optimized
$D_{HH}$ (Å)	$37.44 \pm 1.07$	$40.18 \pm 1.04$	$37.64 \pm 0.88$
$D_B$ (Å)	$36.54 \pm 0.47$	$40.90 \pm 0.31$	$39.36 \pm 0.43$
$2D_C$ (Å)	$27.07 \pm 0.34$	$30.33 \pm 0.29$	$28.97 \pm 0.34$
$V_H$ (Å <sup>3</sup> )	$310.68 \pm 1.14$	$316.13 \pm 0.83$	$314.81 \pm 0.75$
$V_C$ (Å <sup>3</sup> )	$904.89 \pm 1.28$	$891.79 \pm 1.65$	$896.50 \pm 1.19$
$V_L$ (Å <sup>3</sup> )	$1215.57 \pm 1.00$	$1207.92 \pm 1.57$	$1211.32 \pm 1.21$
$K_A$ (ns <sup>-1</sup> )	N/A	$7.12 \times 10^{-3} \pm 8.18 \times 10^{-5}$	$2.65 \times 10^{-3} \pm 1.74 \times 10^{-5}$
$K_D$ (ns <sup>-1</sup> )	N/A	$3.20 \times 10^{-3} \pm 4.75 \times 10^{-5}$	$3.58 \times 10^{-3} \pm 2.83 \times 10^{-5}$
$A$	N/A	74.51	91.88
$\tau$ (ns)	N/A	96.73	160.54
$K_A/K_D$	N/A	2.225	0.74

volumes  $V_H$  and  $V_C$  (lines 1 and 2) are computed following the procedure outlined by Petrache

*et al.*,<sup>42</sup> and described at length in chapter 1 of this dissertation. The total lipid volume  $V_L$  (line 3 in table 2.6) is taken to be the sum of these two values. These remain relatively similar in all three systems, as this value is intrinsic to the lipid molecule and should not change with the inclusion of ions.

Structural data are obtained for lipid bilayers via small angle X-ray and neutron scattering experiments as a one-dimensional form-factor. Data are then fitted to a continuous function to retrieve number and electron densities for the various lipid components.<sup>40,41</sup> Our simulations allow us direct access to the electron densities and number densities. The entries in table 2.6 are determined from these densities.

Figure 2.4 shows the electron densities and corresponding bilayer form-factors. Form-factors are computed by taking the cosine-transform of the symmetrized electron densities. We note that the simulations carried out using LB rules produced a thicker bilayer and had different details at the peak region of the density. The new parameter set results in similar electron density to that of the system without salt. This is similar to the results reported by Petrache *et al.* and Pabst *et al.*, where for systems with less than 1 M NaCl, the differences in the electron densities were not discernible.<sup>50,51</sup> These electron densities are used directly to measure the value of  $D_{hh}$ , defined as the peak-to-peak distance (see table 2.6 line 4). The new parameter set corresponds to a smaller  $D_{hh}$ , similar to the system without salt.

In addition to  $D_{hh}$ , different measures are used to assess the bilayer thickness that relies on the probability densities of different components of the system. It can be shown that  $D_B$  (see table 2.6 line 5) computed by integrating one minus the probability density of solvent and ions is equivalent to the computation of the Luzzati thickness of the total bilayer.<sup>26,41</sup> We define probability of finding a particular component in a slice of the box as,

$$P_i(z) = \frac{\rho_i(z)}{\sum_j^n \rho_j(z)}, \quad (2.2)$$

where  $\rho_i(z)$  are the number densities for the component particles ( $i$ ) of the system as a function of the  $z$ -position of each slice of the box, and the summation ranges over all components in the particular slice. Thus,

$$D_B = \int_{\text{Box length}} (1 - P_{\text{water+ions}}(z)) dz. \quad (2.3)$$

In table 2.6 line 2, the  $D_B$  is larger for the systems with ions, but the value obtained using our new parameter set is closer to that of the bilayer simulated without salt.

We use a similar definition of probability density for  $2D_C$ , computed from the probability distribution of the lipid chains. This component is defined by the hydrocarbon chains starting after the ester-linkage on both the Sn1 and Sn2 terminal of the lipid backbone. This value (line 6 in table 2.6) is increased in the system simulated with LB rules over the system without salt, as we reported in our previous work. However, the new parameter set yields a value similar to the system without salt, which is consistent with the smaller overall thickness of the bilayer simulated with optimized cross terms.

The differences in bilayer thickness are closely related to the packing of the lipid chains in the hydrophobic core of the bilayer. When the chains become more disordered, the bilayer thickness typically drops.<sup>40</sup> Lipid chain ordering can be determined experimentally by performing NMR on specifically deuterated hydrocarbon chains. Since we lack hydrogen on our coarse-grained lipid chains, we cannot directly access the C-D ordering. Instead, we compute the chain order tensor  $S_{\alpha\beta}$  defined as

$$S_{\alpha\beta} = \frac{1}{2} \langle 3 \cos \theta_\alpha \cdot \cos \theta_\beta - \delta_{\alpha\beta} \rangle,$$

where the angles  $\theta_\alpha$  and  $\theta_\beta$  are the angles between the molecular axis and the box  $z$ -direction. We then use this tensor to calculate the  $S_{CD}$  as

$$-S_{CD}^{\text{Saturated}} = \frac{2}{3} S_{xx} + \frac{1}{3} S_{yy} \quad (2.4)$$

for saturated carbons,<sup>67</sup> and as

$$-S_{CD}^{\text{Unsaturated}} = \frac{1}{4}S_{zz} + \frac{3}{4}S_{yy} \mp \frac{\sqrt{3}}{2}S_{yz} \quad (2.5)$$

for unsaturated carbons.<sup>68</sup> These values are plotted per each carbon in the lipid chain in figure 2.5. As reported in our previous simulations, the addition of salt has an ordering effect on the lipid chains. This effect is also seen in our new parameter set; however, the ordering is less pronounced, which is consistent with the notion that the bilayer structure is not significantly altered at physiological salt concentration.<sup>50,51</sup>

While this result indicates a structure more consistent with experimental results, the detailed structure of a lipid bilayer is a result of the delicate balance between ion–lipid, lipid–water, and ion–water interactions. In order to fully understand how our new parameter set has altered the overall bilayer structure, we next characterize the specific interactions between these moieties.

### 2.4.3 Membrane-Salt Interactions

Both ions and solvent compete for the binding sites on the lipid headgroup. As seen in figure 2.2, the new cross terms produce a relatively stronger interaction between  $\text{Na}^+$  and lipid headgroup components compared to that of the LB rules. Thus, there is potentially a reduction in the available binding sites for the solvent. To examine how the new cross terms have altered ion interactions with lipids in the bilayer, we first characterize the dynamics of ion binding to the lipid bilayer.

We define ion binding to the lipid bilayer when half or fewer of its first shell coordinators are not waters. In order to compute the equilibrium binding constant, we must determine the equilibrium number of bound ions to the lipid surface. Figure 2.6 shows the number of bound ions as a function of time over the entire duration of the simulation. We note that even after 700 ns of simulation time, the number of bound ions are not fully equilibrated.



Thus, we use first-order reaction kinetics to estimate the asymptotic number of bound ions. The first-order reaction kinetics are modeled as a differential equation:

$$\frac{dN_b}{dt} = K_a (N - N_b) - K_d N_b, \quad (2.6)$$

where  $N_b$  are the number of bound ions, and  $K_a, K_d$  are the association and dissociation time constants, respectively. The solution of this differential equation is:

$$N_b(t) = \frac{K_a}{K_a + K_d} N (1 - \exp[-(K_a + K_d)(t - t_0)]). \quad (2.7)$$

This solution is fit to the data in figure 2.6, and the resulting fit is also plotted. The fitting parameters are listed in table 2.6. The first-order reaction kinetic model fits reasonably well to the data from both the systems, except in the beginning of the simulation where the effect of the annealing process is more pronounced; however, we are only interested in the asymptotic behavior of the fit as this is representative of the equilibrium state of the system. The asymptotic number of bound ions as  $t \rightarrow \infty$ ,  $A = \frac{K_a}{K_a + K_d} N$  (table 2.6 row 9), is larger in the system simulated with optimized terms. We also report the timescale of ion binding  $\tau = \frac{1}{(K_a + K_d)}$  for both systems (table 2.6 row 10). The timescale of binding in the system using optimized cross terms is longer, and suggests that this system would need more time to equilibrate than the system simulated with LB rules. Finally, we report the value of  $\frac{K_a}{K_d}$  (table 2.6 row 11), which we observe is much smaller with the new parameter set than compared to that of the system simulated with LB rules.

To examine how specific interactions between ions and lipids are modified by the new parameters, we tracked the binding partners of ions across the box over the last 150 ns of simulation time. Moieties are considered to be bound to an ion if they are within a distance of 3.3 Å from the  $\text{Na}^+$  ion. Several electronegative groups in the simulation can potentially bind to the  $\text{Na}^+$  ion. We compute the number of these potential binding partners within the first shell of each  $\text{Na}^+$  ion across the simulation box. Ions are then sorted according to

their box z-positions, and then the data are averaged over the last 150 ns. This is plotted in figure 2.7. We note first that the total number of solvating oxygens of ions within the bilayer headgroup region with the optimized parameter set has dropped by  $\sim 1$  when compared to ions in similar locations in the system simulated using LB rules. This is not surprising, given the dependence of ion coordination preferences on the local environment.<sup>69</sup> The binding to other lipid oxygens has not been altered much by the new parameter set; however, we do note that water within the headgroup region does not appear to be strongly associated with ions.

#### 2.4.4 Water Structure and Dynamics

To further characterize the dehydration of ions in the new simulated system, we look to the lipid– and ion–water interactions. Figure 2.8 shows the number density of water as a function of distance from the bilayer center for each of our simulated systems, with the  $2D_C$  and  $D_B$  illustrated as dotted lines. We see that our new parameter set produces a bilayer interface that has more solvent inside the headgroup region, between  $10 - 25 \text{ \AA}$  from the bilayer center. This density is more similar to that of the system simulated without salt. This suggests that the dehydration of ions in the system simulated with optimized parameters does not correspond to a dehydration of the lipid bilayer.

Next, we characterize the orientational structure of the water. Figure 2.9 examines the water order parameter across the simulation box. We identify perturbed water structure by examining first ( $P_1$ ) and second ( $P_2$ ) orientational order parameters for the  $OW \rightarrow HW1$  bond of water with respect to the z-axis of the simulation box ( $\beta$ ). These order parameters are defined using the first and second Legendre polynomials with respect to the angle  $\beta$ ,

$$\begin{aligned} P_1 &= \langle \cos(\beta) \rangle \\ P_2 &= \frac{1}{2} \left\langle (3 \cos^2(\beta) - 2) \right\rangle, \end{aligned} \tag{2.8}$$

where average is over all the waters in a particular volume slice of the box and then over simulation time. We plot these values as a function of distance from the bilayer center.  $P_1$  denotes dipolar ordering of the bond vector and the bilayer normal direction, with a positive value indicating an average outward orientation and a zero value corresponding to an average perpendicular orientation to the bilayer normal or a uniformly random orientation. We observe a similar pattern of ordering across the box in all systems; however, we see an overall reduction in ordering with our new parameter set when compared to both the LB and the no-salt system. We also see the inner minimum of the order parameter moved further into the bilayer when compared to LB, which is consistent with the larger quantity of water in this region that we observe in the water densities.

Following the protocol established in our previous work,<sup>34</sup> we identify three regions within the bilayer interface,  $B_{-1}, B_+, B_{-2}$ . The  $B_{-1}$  region is defined as the region of negative ordering starting at the bilayer center, and ending when the order parameter values cross zero at the start of the  $B_+$  region. The  $B_+$  region starts at the end of the  $B_{-1}$  region, and is the area of positive ordering, ending where the order parameter crosses zero again. The  $B_{-2}$  region starts at the end of the  $B_+$ , and extends out to where the second order parameter goes to zero. This was found by fitting an exponential function to this region and taking the scale parameter from that fit as the boundary with bulk solvent. We find that water is significantly less perturbed by the bilayer with our new parameter set. We have also computed  $P_2 \cdot \rho_{\text{Water}}$ , shown in figure 2.9(c). This value relates the amount of water in each region of the box and the overall ordering in the region. We still see significantly less ordering with the new parameter set, and even with the larger number of waters in the bilayer headgroup. The integral of this curve is related to the quadrupole splitting  $\Delta\nu$  observed in deuterium NMR experiments.<sup>33,70</sup>

This suggests that while there is more solvent in the interface, it is perhaps not associated with either  $\text{Na}^+$  or lipids, and may remain less structured than in the system simulated with LB rules. This can be further ascertained by the lateral diffusion coefficients of waters in

each of the regions defined by  $P_2$ . We compute the mean square displacement (MSD) for water oxygens in each region by first tracking which waters remain in the region. Any waters that leave the region are removed from the MSD calculation. We chose a duration of 100 ps to track the MSD in order to have a sufficiently long time for the MSD to become linear, while still maintaining a statistically significant number of waters in the slice. A line is fit to the middle 80% of the MSD, and the fitted slope is used to calculate the diffusion coefficient following Einstein’s relation for 2D diffusion

$$\lim_{t \rightarrow \infty} \frac{\langle (r(t) - r(0))^2 \rangle}{(t - t_0)} = 4D. \quad (2.9)$$

These values can be seen in table 2.7. We note that the water in the headgroup region,

Table 2.7: Diffusion coefficients of water in different regions of the lipid bilayer, defined by the shape of the second orientational order parameter of water molecules in the box. These regions are defined by the shape of the distribution of the second orientational order parameter across the simulation box.  $B_{-1}$  is the region of negative ordering starting at the bilayer center, and ending when the order parameter values cross zero.  $B_{+}$  starts at the end of the  $B_{-1}$ , and is the region of positive ordering ending where the order parameter becomes negative. This starts the  $B_{-2}$  of negative ordering, extending out to where the second order parameter goes to zero, where we have *Bulk* solvent. We see that the optimized parameters result in slightly increased diffusion in the solvent, which correlates with the reduced ordering of the water dipoles and quadrupoles in the system.

	LB ( $\times 10^{-10} m^2/s$ )	Optimized ( $\times 10^{-10} m^2/s$ )
$B_{-1}$	$1.11 \pm 1.10$	$1.88 \pm 2.41$
$B_{+}$	$4.23 \pm 1.14$	$6.11 \pm 2.83$
$B_{-2}$	$18.11 \pm 4.23$	$21.29 \pm 4.12$
<i>Bulk</i>	$27.32 \pm 1.15$	$27.25 \pm 1.36$

corresponding to  $B_{-1}$  and  $B_{+}$ , diffuses slightly faster with the new parameter set, indicating more mobile water in these regions. However, the computed diffusion coefficients are within the error bars that of the system simulated with LB rules. Diffusion in the  $B_{-2}$  and *Bulk*

regions are similar in both systems, as these are mostly outside of the bilayer and should not be affected by the new parameter set.

#### 2.4.5 Bilayer Electrostatics

We further characterize the electrostatic properties of our bilayer systems by computing the electrostatic potential across the simulation box. We do this following the protocol used in Saunders *et al.*<sup>34</sup> We first compute the charge density of the system components. We integrate this distribution twice, setting both constants of integration to be zero to enforce a zero value for the electric field in bulk solvent and a zero electrostatic potential at the box edge. This is accomplished by taking the average value of the electric field in the *bulk* region of the box defined earlier, and subtracting this value from all points. Due to the larger system size in the optimized system, we needed to compute the average value of a much larger region than in LB in order to apply boundary conditions. We then integrate again to get the electrostatic potential. This result can be seen in figure 2.10 in supporting information. The shape of the potential is largely unaltered within fluctuations. Systems simulated with the optimized parameters and with LB rules both have a similar bilayer dipole potential, which remains elevated over the system without salt, by  $\sim 220$  mV. We report that the optimized system has a slightly elevated bilayer dipole potential compared to the system simulated with LB rules, increased by  $\sim 12$  mV. This may be a direct result of the larger number of ions bound to the bilayer in this system. We also note the system simulated with optimized cross terms has different details throughout the electrostatic potential compared to the system simulated with LB rules and in the system without salt, however these are within fluctuations and cannot be used to draw conclusions.

Poisson–Boltzmann (PB) theory is a mean field approximation for solvated ions near an interface. Experimentally PB theory is used to assess the surface potential of the lipid bilayers. We also examine the behavior of the ions in bulk solvent under the framework of PB theory. Following the procedure used in our previous work,<sup>34</sup> we fit the number density

of Cl<sup>-</sup> ions in the solvent-occupied region of the box to a Poisson-Boltzmann distribution, using the inverse Debye length  $K$  and the density of Cl<sup>-</sup> at the center of the solvent occupied region of the box  $\rho_0$  as fit parameters. The density is modeled as:

$$\rho(z) = \rho_0 \exp(-\bar{z}e\beta\psi(z)), \quad (2.10)$$

where  $\rho_0$  is the number density of the ion at the center of the solvent-occupied region of the box,  $\bar{z} = 1$  is the valency of the ion in the system,  $\beta = \frac{1}{k_b T}$ ,  $e$  is the charge on an electron, and  $\psi(z)$  is the electrostatic potential. We then assume the form of  $\psi(z)$  to be the sum of two Debye-Huckel potentials<sup>71</sup> reflected across the center of the solvent-occupied region of the box:

$$\begin{aligned} \psi_1(z) &= \psi_s \exp(-K(z + \frac{D}{2})) \\ \psi_2(z) &= \psi_s \exp(K(z + \frac{D}{2})) \\ \psi(z) &= \psi_1 + \psi_2, \end{aligned} \quad (2.11)$$

where  $D$  is the distance from the hydration boundary of one bilayer leaflet to the next across the solvent,  $K$  is the inverse Debye length, and  $\psi_s$  is the surface potential:

$$\psi_s = \frac{\varsigma}{\varepsilon_0 \varepsilon K}. \quad (2.12)$$

The LB system yielded a value of  $D = 13.167$  nm and the system simulated with optimized parameters, containing twice as many solvent molecules, gave a value of  $D = 27.01$  nm. We take the surface charge density  $\varsigma$  from the charge density inside of the hydration boundary of the lipid bilayer. Since only ions contribute a net charge to our system, we compute this using only the charge density of ions in the system. This value was computed to be  $\varsigma = 0.13 \text{ } e \text{ nm}^{-2}$  for the system simulated with LB rules, and  $\varsigma = 0.11 \text{ } e \text{ nm}^{-2}$  for the system simulated with the new parameters. Our fitting procedure yielded number densities

$\rho_0 = 0.043\text{nm}^{-3}$  for the system simulated with LB rules, and  $\rho_0 = 0.079\text{nm}^{-3}$  for the system simulated with optimized parameters. The fitted inverse screening lengths were found to be  $K = 0.91 \pm 0.014 \text{ nm}^{-1}$  for the LB rules simulation and  $0.94 \pm 0.018 \text{ nm}^{-1}$  for the system simulated with optimized parameters. The resulting fit and predicted density of  $\text{Na}^+$  ions and electrostatic potential can be seen in figure 2.11. We see the results from our simulation represented by points with error bars, while PB theory results are shown in solid lines. We see excellent agreement in the  $\text{Na}^+$  density profile away from the bilayer surface, and reasonable agreement in the electrostatic potential. From this we can see that the optimized and LB systems both exhibit similar ionic distributions with models used to describe electrophoretic mobility experiments.<sup>71</sup>

## 2.5 Conclusions

Mixing rules are often relied upon to compute non-bonded cross terms for interacting molecules in molecular simulations. However, when mixing force-fields that have been developed independently of each other, inaccuracies may develop. Here we demonstrate one such case and propose a rigorous solution. MD simulations conducted using predefined mixing rules for non-polarizable force fields developed separately for ions and lipids have always produced very pronounced salt-induced structural changes in lipid bilayers. Contrary to this, most experimental observations point to a moderate or even an insignificant change in bilayer structure at physiological salt concentrations. We resolve this discrepancy by explicitly parameterizing ion-lipid cross terms using our procedure “*Many Body Non Bonded fix*” (MB-NB-fix). It is based on the NB-fix method employed in previous works<sup>8-16</sup> and utilizes ParOpt software developed in our lab<sup>60,61</sup>. We note that after applying the optimized parameters for  $\text{Na}^+$ -lipid interactions, the bilayer structure conforms more to experimental observations while all other properties such as solvent structure, electrostatic potential, and dynamic properties are approximately similar to that obtained with those obtained with LB parameters. We note that we have not applied this method to optimize  $\text{Cl}^-$  interactions

terms, which may still further affect the bilayer structure. This will be the subject of future work.

The MB-NB-fix method proposed here is a general method which can be used to derive mixing terms for simulations with independently developed force fields. This method will be used in future work to improve other sets of mixed force-fields, including those of other monovalent ions and the gromos 43A1-S3 lipids, and between these lipids and amino-acids for use in proteins. Furthermore, many body cooperativity effects, such as ion-induced polarization in lipid molecules may be critical to further improving the reproduction of lipid bilayer structure. A correct approach to incorporate these effects to our simulation would be to have explicit polarization terms in our simulation models. This is complicated, as most existing polarizable simulation models are either not very effective at accurately reproducing polarization effects or are much more computationally expensive compared to classical non-polarizable simulations. The MB-NB-fix method has potential to become an ideal solution for mixing force-fields, including polarizable and non-polarizable models in the same system to construct simulations that are tractable yet accurate.



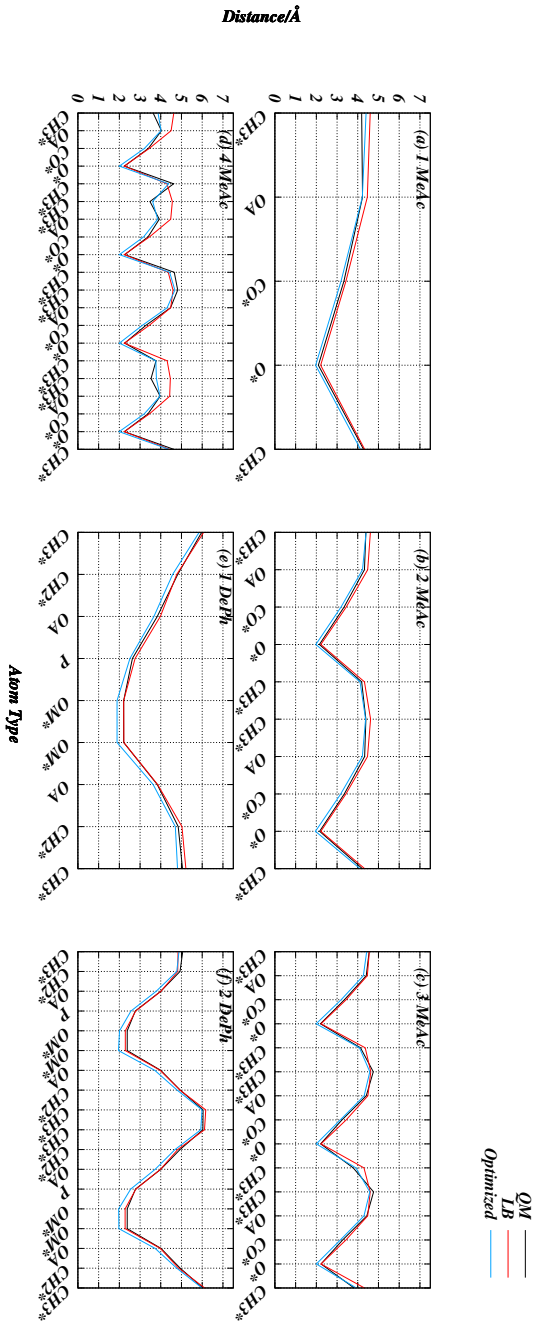


Figure 2.3: Distances from  $\text{Na}^+$  to each component atom in sample clusters. We compute the geometry of our sample clusters by computing the distance from the ion to each other atom in the system, shown per atom type. These distances are used in combination with the substitution energies in figure 2 to compute the error for the NM optimization.

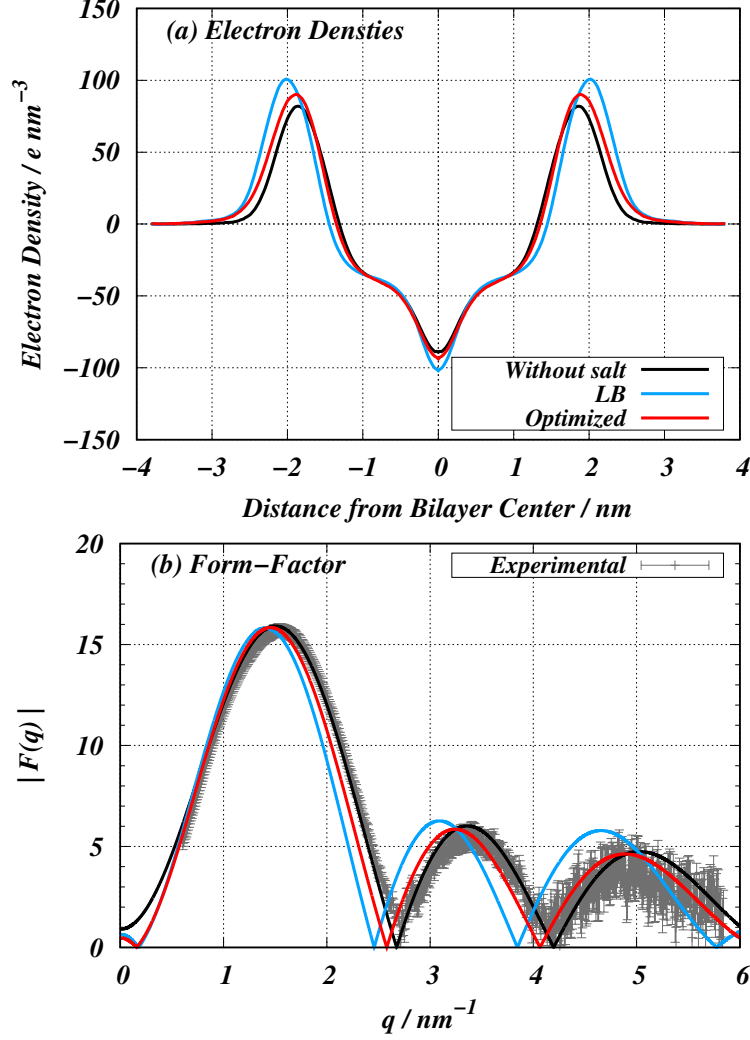


Figure 2.4: Electron densities of the simulated bilayers (a), and corresponding bilayer form-factors (b). Electron densities as obtained using the GROMACS density tool, centered at the minimum to define the bilayer center, and with the electron density of solvent subtracted. The simulated with optimized parameters appears to lack the large peak seen in the system simulated with LB rules, and appears more similar to the bilayer structure of a bilayer simulated without salt. This is further reflected in the bilayer form-factor, computed by taking the cosine-transform of electron density. Experimental SAXS results are for a POPC bilayer in pure solvent.<sup>41</sup> We see the first lobe of the optimized system moves closer to the experimental results and the form-factor of a system without salt. This lines up with experimental results, that have shown small, if any, change in the bilayer SAXS form-factor.<sup>50–52</sup>

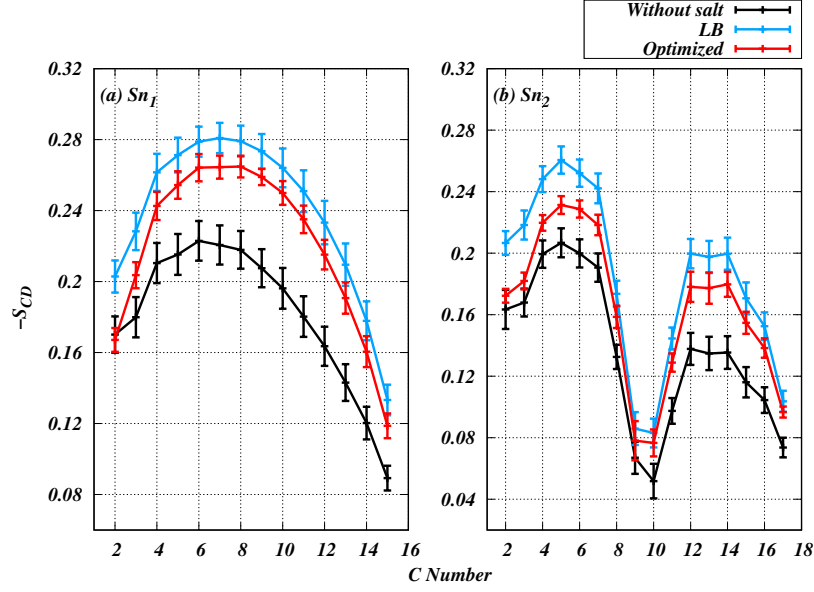


Figure 2.5: Lipid chain deuterium order parameters.  $S_{CD}$ s are computed for each carbon for the chains  $Sn_1$  (a) and  $Sn_2$  (b), starting at the second carbon in the chain. We see that the optimized system is still showing significant ordering in the lipid chains as a result of ion binding; however, the ordering is less pronounced than in the system simulated with LB rules, and is closer to that of the simulation without salt. This result corresponds with the smaller bilayer thickness in the optimized system.

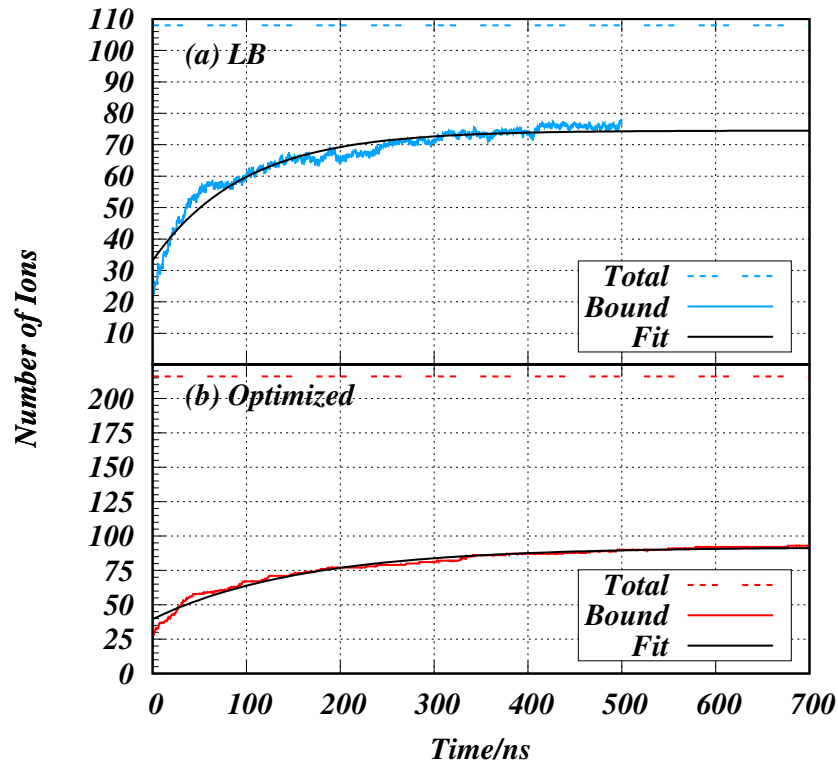


Figure 2.6: Number of ions bound to the lipid bilayer as a function of simulation time. The exponential fits to this data are also shown. These fits are used to compute the asymptotic number of ions bound as well as binding rate constants. ‘Total’ refers to the total number of ions in each simulation box. A membrane bound ion is defined as having half or fewer of its first coordination shell occupied by water molecules.

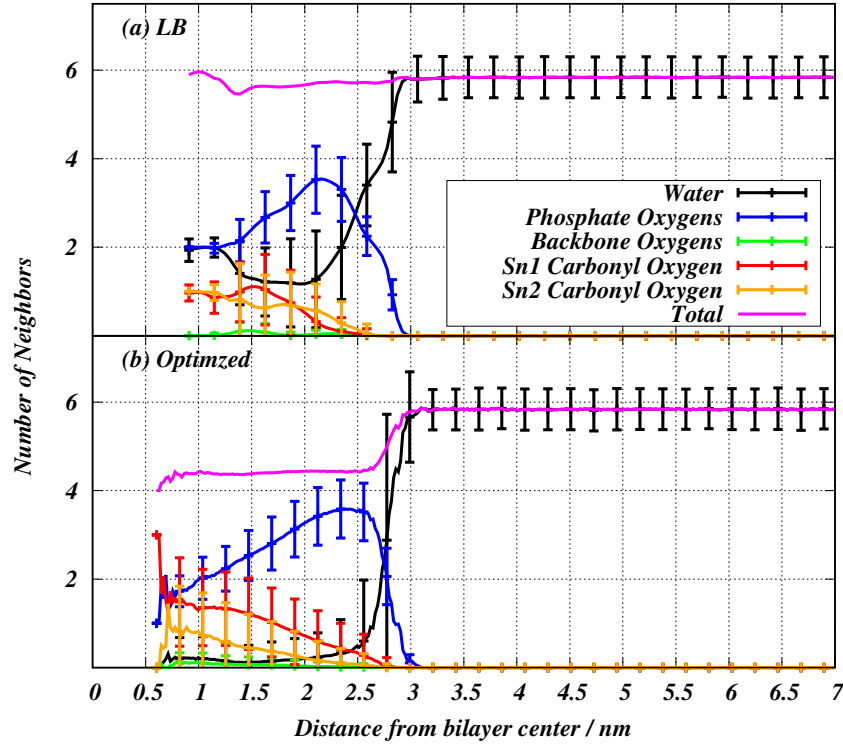


Figure 2.7: Chemistry of  $\text{Na}^+$  inner shell coordination as a function of distance from bilayer center. Compared to the system simulated with LB rules (a), the system simulated with optimized cross terms (b) yields a lower  $\text{Na}^+$  total coordination number within the headgroup region of the bilayer. This drop in coordination appears to be due to a greater dehydration of the ions in this system.

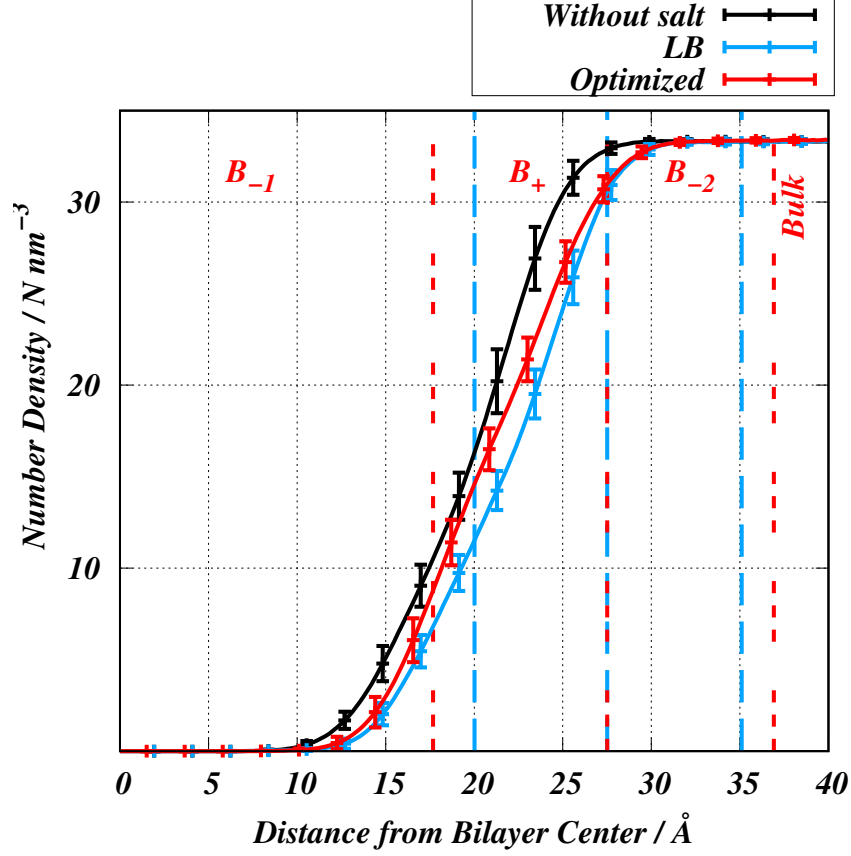


Figure 2.8: Water density at the bilayer interface. We illustrate the regions  $B_{-1}$ ,  $B_{+}$ ,  $B_{-2}$  and  $Bulk$  for each system with dotted lines. We see that the optimized cross terms yield a greater density of solvent in the  $B_{+}$  and  $B_{-1}$  regions over the system simulated with LB rules. We also see the density in these regions of the system optimized with optimized cross terms is more similar to that of the system without salt.

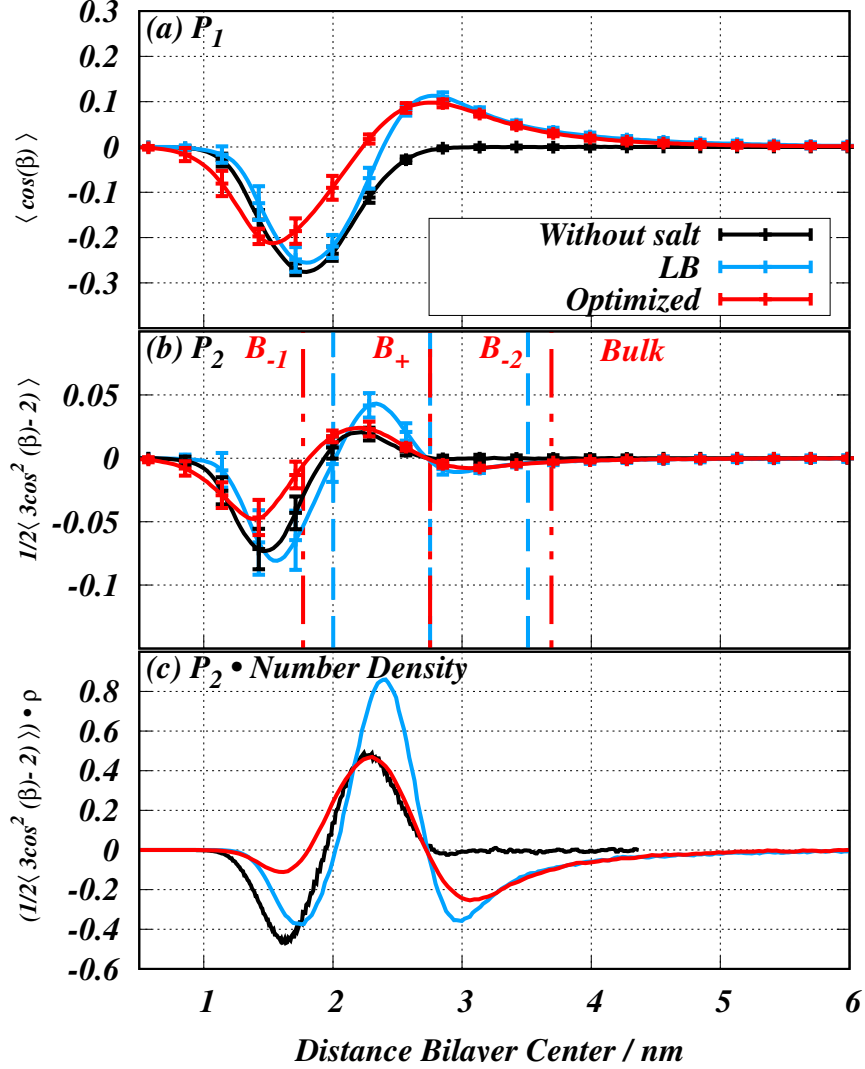


Figure 2.9: Water orientational order parameters  $P_1$  (a) and  $P_2$  (b), and the product of the water number density and  $P_2$  (c). We see in  $P_1$  and  $P_2$  less ordering in the waters in the optimized system, suggesting that waters may be less strongly interacting with ions or lipid components. We denote the four regions of the lipid bilayer based on the shape of the  $P_2$  data as dotted lines in (b).<sup>34</sup> We have not included these regions for the system without salt, as the  $P_2$  data does not include the same details as the systems with salt. The integral of (c) is related to the quadrupolar splitting constant  $\Delta\nu$  found in deuterium NMR experiments. This also gives a closer look at how solvent is ordered in the headgroup while accounting for the amount of solvent in the region. We see that optimized cross terms result in a significant drop in the area under the curve, which is much closer to the shape of the data from the system without salt. The regions  $B_{-2}$  and  $Bulk$  are not within the bilayer headgroup, and are expected to be less affected by the new parameter set.

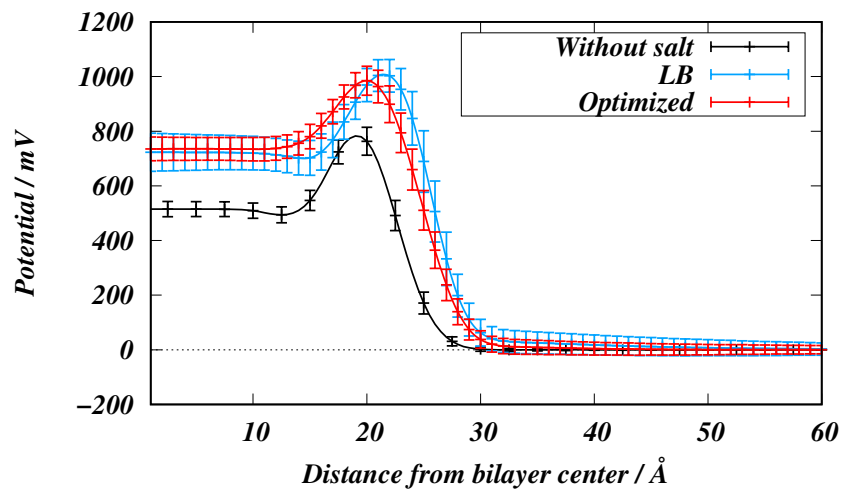


Figure 2.10: Electrostatic potential as a function of distance from bilayer center. The optimized cross terms yield a small change in the location of the peak of the potential in the bilayer simulated with optimized cross terms, as well as the loss of the valley behind the peak.



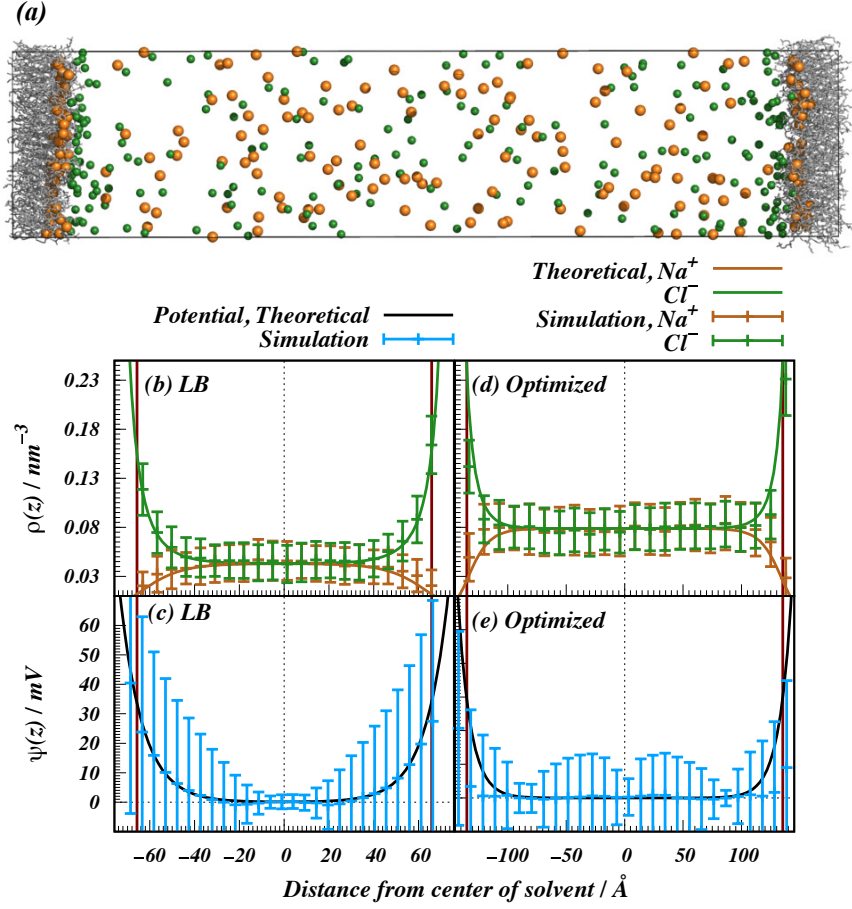


Figure 2.11: Poisson-Boltzmann theory predictions and simulation results. (a) shows a snapshot of the system simulated with optimized cross terms, translated to center the solvent occupied region. Water has been hidden for clarity. (b) and (d) show the number density of ions in the solvent occupied region of the box. (c) and (e) show the corresponding electrostatic potential in solvent. We illustrate theoretical predictions as solid lines, with corresponding simulation results as points with error bars. Red vertical lines denote the *hydration boundary* of the lipid bilayer. Cl<sup>-</sup> density data is used for fitting in both systems.

### 3 Adsorption modes of $\text{Na}^+$ , $\text{Li}^+$ , and $\text{Mg}^{2+}$ to a model zwitterionic lipid bilayer<sup>1</sup>

#### 3.1 Abstract

The adsorption of ions to soft-porous interfaces plays a critical role in many physical and biological processes, such as the function of electrochemical energy storage devices or the attachment of membrane proteins to cells surfaces. In this work we characterize different adsorption modes, and describe the adsorption behavior of  $\text{Na}^+$ ,  $\text{Li}^+$ , and  $\text{Mg}^{2+}$  onto a porous substrate. We identify three categories of adsorption based on the degree of dehydration of the ion, viz., steric adsorption corresponding to a lack of dehydration, imperfect adsorption with partial dehydration, and perfect adsorption representing total dehydration. Using 1-palmitoyl-2-oleoyl-sn-glycero-3-phosphatidylcholine (POPC) in salt solution as a generic model system for salt at a soft and porous interface, based on the simulation model used we find that anions,  $\text{Cl}^-$ , always adsorb sterically. Among cations, the divalent  $\text{Mg}^{2+}$  does not dehydrate, and is also adsorbed sterically. On the other hand,  $\text{Na}^+$  adsorbs to a large fraction perfectly and  $\text{Li}^+$  exhibits a significant fraction of imperfectly adsorbed ions. We demonstrate that, with everything else held fixed, the adsorption mode of a cation is determined solely by the strength of the electric field produced by the ion at the distance of the hydration shell.

#### 3.2 Introduction

Interactions of ions with soft, porous, and charge-neutral substrates such as zwitterionic lipid bilayers are important and a common system of interest in soft matter physics and biophysics. Empirical studies towards these use simplified models to interpret observations,

---

<sup>1</sup>Portions reprinted with permission from Matthew Saunders, Abibat Adekeye-Olowofela, and Sabrina Downing, *Adsorption Modes of  $\text{Na}^+$ ,  $\text{Li}^+$ , and  $\text{Mg}^{2+}$  to a Model Zwitterionic Lipid Bilayer*, *Langmuir*, American Chemical Society, December 1, 2024. © 2024 American Chemical Society.

e.g. assuming the water as a dielectric continuum, or taking the ions as a spherical entity surrounded by a neatly organized hydration shell.<sup>71</sup>

A simple way of defining adsorption of ions to a substrate comes from the Poisson-Boltzmann (PB) theory.<sup>71</sup> This mean-field approximation predicts accumulation of ions near a surface due to the mutual electrostatic repulsion of the ions and entropic factors. Deviations in ion distribution from the predictions of PB theory near a substrate are the defining characteristic of the specific adsorption phenomenon.<sup>72,73</sup>

Experimental studies of ion adsorption can be broadly classified into two main groups – methods that examine the electric field/surface potential produced by the adsorbed ions, e.g, electrophoretic mobility<sup>74</sup> or measurement of the forces between bilayers,<sup>75</sup> and methods that can more directly characterize the location and dynamics of ions such as x-ray or neutron scattering,<sup>40,41,52,63,76,77</sup> and NMR.<sup>12,40,78</sup>

At the atomistic level, identifying adsorbed ions poses a different kind of challenge. We have addressed this issue previously, where we characterized adsorption by examining the dehydration of ions near the interface.<sup>33,44,79,80</sup> This is similar to the kind of adsorption described by the Langmuir isotherm model, where it is assumed that ions stick to a soft, porous interface through direct interaction.<sup>81</sup> Adsorption defined thusly has been reported in our previous works for monovalent ions such as  $\text{Na}^+$  and  $\text{Li}^+$ .<sup>33,34,44,82</sup> Further, our previous work on divalent ions exhibited that  $\text{Mg}^{2+}$  maintains its hydration structure regardless of where the ion is located in the lipid bilayer,<sup>44</sup> yet maintaining a distribution distinct from that predicted by PB theory. Hence, in this work we characterize different modes of adsorption corresponding to different ions. Here we categorize the adsorption behavior based on degree of dehydration, starting from no dehydration at all as in the case of  $\text{Mg}^{2+}$  and  $\text{Cl}^-$ , extending to complete dehydration as in the case with  $\text{Na}^+$ . In the somewhat different context of RNA, which is not a soft, porous substrate, the specific binding of ions has been addressed extensively<sup>83–87</sup> based on the mobility of cations and further characterized by models that describe the structure of their coordination shell. Cations bound to RNA are frequently

distinguished as being diffuse (similar to our steric adsorbed case), and the site-bound ions are further characterized by outer-shell (again analogous to our steric adsorption ions) or inner shell binding (analogous to the imperfect or perfect adsorbed ions), depending on the folded conformation of the RNA or nearby nucleotides.<sup>83–87</sup>

Along with dehydration, we use specific adsorption in the context of PB density as the defining property of adsorption phenomenon. Based on our previous as well as current atomistic simulations we broadly classify adsorption of ions into three categories – viz. *perfect adsorption*, *imperfect adsorption*, and *steric adsorption*. We also demonstrate that, using different force-field for  $\text{Mg}^{2+}$  the predominant mode of adsorption of  $\text{Mg}^{2+}$  to 1-palmitoyl-2-oleoyl-sn-glycero-3-phosphatidylcholine (POPC) is always *steric adsorption*.

### 3.3 Methods

We perform multiple simulations of POPC bilayers with LiCl and  $\text{MgCl}_2$  salt. Configurations for each simulation are listed in table 3.1.

#### 3.3.1 Bilayer Construction

Bilayers are constructed as described in Chapter 1, with 200 POPC lipids (100 per leaflet) and 60,000 waters to provide sufficient bulk solvent. A subset of waters is randomly replaced with ions to achieve the desired system compositions (Table 3.1), corresponding to an initial

Table 3.1: Simulation system details. Each simulated system is started with 200 mM salt, and the final bulk concentration is computed from the average number density of ions at the center of the solvent occupied region of the box, from the last 150 ns of simulation time.  $\text{Na}^+$ –Saunders *et al.* simulation trajectories are published in our previous work, and are re-analyzed in this work. The  $\text{Mg}^{2+}$ –Li *et al.* system is extended to 2.5  $\mu\text{s}$  to ascertain if any exchange of waters from the first shell of  $\text{Mg}^{2+}$  could be observed.  $\text{Li}^+$  (a) parameters are obtained from the work by Joung and Chetatham III.<sup>53</sup>  $\text{Mg}^{2+}$  (b-c) parameters are obtained from Li *et al.*<sup>88</sup> and Grotz *et al.*,<sup>89</sup> respectively.

System	No. of Cations	No. of Anions	Starting Bulk Salt Concentration	Final Bulk Salt Concentration	Simulated Time
$\text{Na}^+$ From Saunders <i>et al.</i> 2022 <sup>82</sup>	216	216	200mM	103mM	0.7 $\mu\text{s}$
$\text{Li}^+$ (a)	216	216	200mM	102.0mM	1 $\mu\text{s}$
$\text{Mg}^{2+}$ (b)	216	432	200mM	152mM	2.5 $\mu\text{s}$
$\text{Mg}^{2+}$ (c)	216	432	200mM	153mM	1 $\mu\text{s}$

salt concentration of 200 mM. Systems containing  $\text{Mg}^{2+}$  include twice the number of counter-ions to balance charge.

Following energy minimization with the steepest-descent algorithm, each system is equilibrated with a 1 ns NPT simulation at 250 K and then annealed by heating to 350 K and cooling in 10 K steps to 300 K, with each step lasting 155 ps. The final annealed configurations serve as starting points for production simulations.

### 3.3.2 Molecular Dynamics

Production simulations are run for the lengths listed in Table 3.1. Most systems are simulated for 1  $\mu\text{s}$ , with the  $\text{Mg}^{2+}$ -Li *et al.* system extended to 2.5  $\mu\text{s}$  to assess slow water-exchange dynamics in the first coordination shell. An additional 1  $\mu\text{s}$  trajectory is generated using the  $\text{Mg}^{2+}$ -water interaction model of Grotz *et al.*,<sup>90</sup> which yields water-exchange rates in closer agreement with experiment. Trajectory analysis is carried out with GROMACS built-in tools, in-house software using the GROMACS API, and the MDAnalysis Python package.<sup>1,91,92</sup>

### 3.3.3 Force-field parameters

Lipid-lipid and lipid-water interactions are described using our gromos43a1-s3 model,<sup>26</sup> which is calibrated to work with the SPC/E water model.<sup>25</sup>  $\text{Li}^+$ -water interactions are described using Joung and Cheatham parameters.<sup>53</sup> Target data are computed using the method described in Saunders *et al.*<sup>82</sup> and in the first chapter of this dissertation to compute non-aqueous cross-terms for  $\text{Li}^+$ . Target data consist of substitution energies and optimized geometries of  $\text{Li}^+$  clusters with water, methyl acetate, and diethyl phosphate ligands. The substitution energies from DFT calculations serve as benchmarks for parameter optimization, and are compared against Lorentz-Berthelot mixing rules and the optimized parameters (see Table 3.3 and Figures 3.1–3.2).

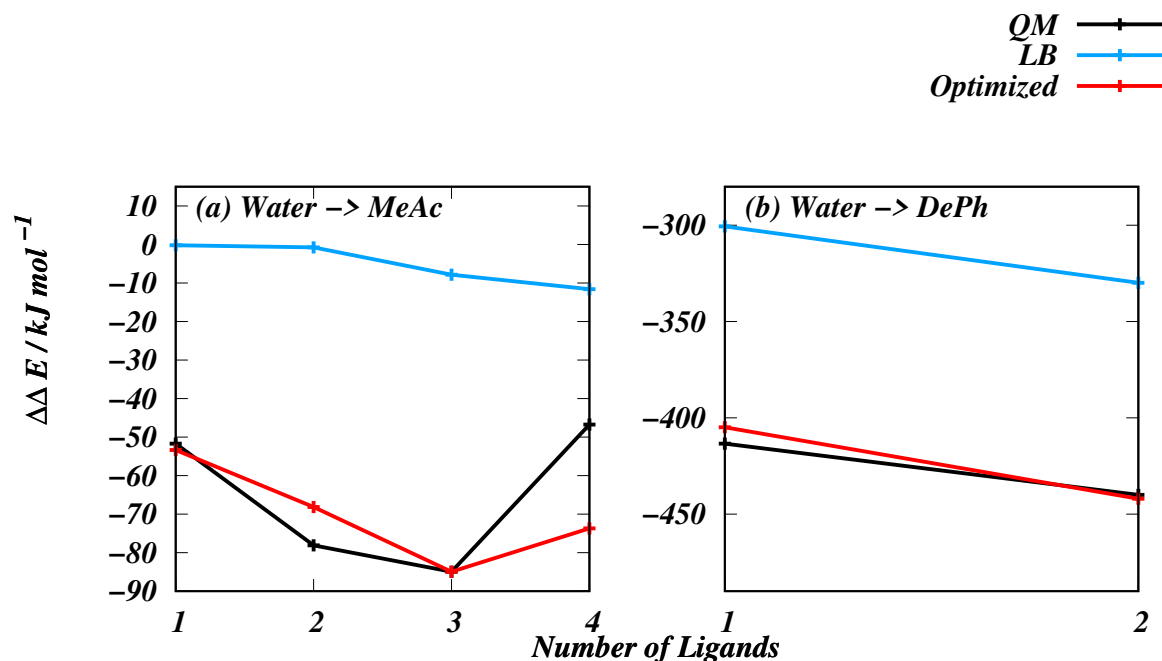


Figure 3.1: Substitution energies of  $\text{Li}^+$  clusters with methyl acetate and diethyl phosphate ligands. Black points are *ab initio* values, blue is the Lorentz–Berthelot prediction, and red is the result of the optimized parameters.

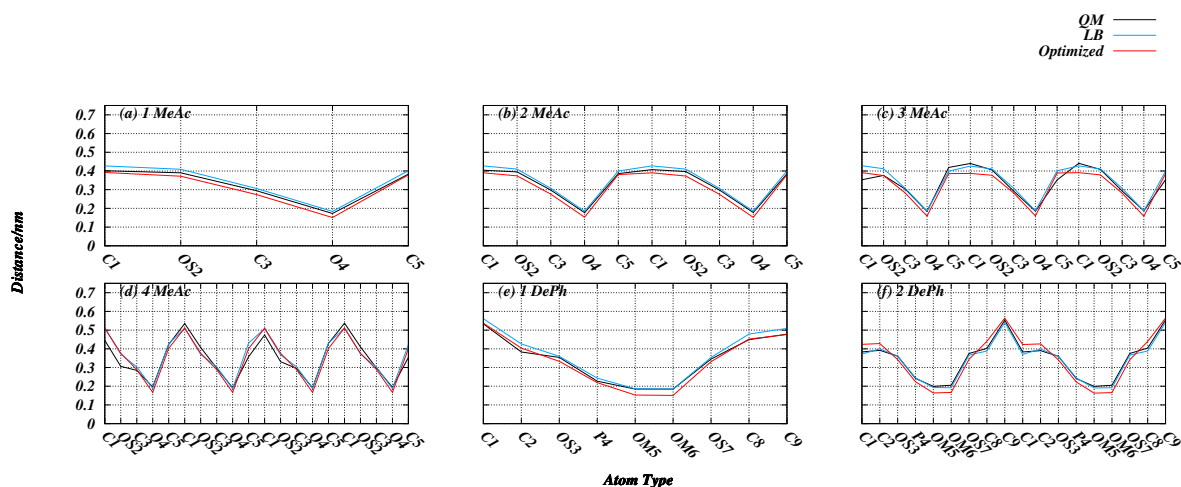


Figure 3.2: Distances of all ligand atoms from  $\text{Li}^+$  for each cluster. Lorentz–Berthelot parameters give geometries close to the target data, while the optimized parameters bring the ion slightly closer to electronegative oxygens.

Describing the interactions of  $\text{Mg}^{2+}$  with water presents several challenges, and there are numerous models developed to describe  $\text{Mg}^{2+}$ -water interaction.<sup>88,89,93</sup> These models are optimized to improve the hydration free energies as well as binding energies with various solvent models.<sup>88,89,93</sup> Previous work by our group has examined  $\text{Mg}^{2+}$  models from Li *et al.* and Allner *et al.*<sup>88,93</sup> in simulations with POPC lipids,<sup>44</sup> and found little variation among them in terms of their effects on lipid bilayer properties. With this in mind, we chose to focus our work here on the parameters developed by Li *et al.* because their optimization procedures closely follow our focus on binding energies. In recent work it has been reported that the existing  $\text{Mg}^{2+}$  parameters, including those developed by Li *et al.* overestimate the residence time for a water molecule in the first coordination shell of an ion.<sup>89</sup> In our past works using this force-field we reported insignificant Langmuir type adsorption of  $\text{Mg}^{2+}$  ions to the POPC bilayer, with waters retained in the first coordination shell of the ion.<sup>44</sup> We have also performed simulations with the parameters developed by Grotz *et al.* that directly reduce residence times while not significantly changing other solvation properties of the ion.<sup>89,90</sup> This was done to study how the interactions with water could affect the first-shell coordination of  $\text{Mg}^{2+}$  in the bilayer interface. We have computed the interaction cross-term for the  $\text{Mg}^{2+}$  ion from Grotz *et al.* with SPC/E water explicitly, using the Lorentz-Berthelot mixing rules. Similarly to  $\text{Li}^+$ , we selected LJ cross-terms for use in our simulation following the procedure from Saunders *et al.* 2022.<sup>82</sup> Target QM data for clusters of water with  $\text{Mg}^{2+}$  are shown in table 3.2.

Table 3.2:  $\text{Mg}^{2+}$  binding energies to water clusters determined using different QM theories and classical force fields. All energies are in kJ/mol. These are used when computing the energies of substitution from water to lipid parts, which we use as our optimization target when selecting LJ cross-terms.

Waters	CCSD(T)/CBS <sup>38</sup>	PBE0+vdW <sup>38</sup>	AMOEBA-HFC <sup>38</sup>	Li et al. <sup>88</sup>	Grotz et al. <sup>89</sup>	Allner et al. <sup>93</sup>
1	-344.8	-349.9	-349.8	-276.8	-282.8	-270.3
2	-651.0	-657.6	-657.3	-544.3	-557.3	-531.5
3	-898.7	-904.6	-902.5	-792.1	-815.2	-774.3
4	-1101.2	-1103.4	-1100.4	-1018.3	-1055.3	-995.7
MAE	-	4.9	4.0	91.1	71.3	106.0

These energies for water were similar enough across force-fields that we chose to use only the values from Li *et al.*<sup>88</sup> for use in computing substitution energies for our target data. The result of our parameter search are shown in table 3.3.

### 3.4 Results and Discussion

#### 3.4.1 Bilayer simulations of $\text{Li}^+$ and $\text{Mg}^{2+}$

##### Lipid bilayer structure

The distribution of electron dense and heavy atoms is often studied by using scattering techniques, like small-angle x-ray and neutron scattering. These methods yield a scattering form-factor. Densities can be obtained from the form-factor by solving the inverse problem, which is a technically hard problem. In experiments this is usually solved by fitting a model to the form-factor. Simulations give us direct access to atomic positions, and consequently the densities. This allows us to compute a scattering form-factor by taking a cosine transform of the density. The computed form-factor can be compared with the direct measurements of the experiment. The simulated lipid bilayer x-ray scattering form-factors and associated

Table 3.3: Lennard-Jones cross-terms used in each  $\text{Mg}^{2+}$  simulation. We have computed LB-terms using Lorentz-Berthelot (LB) mixing rules, starting with the self-terms for  $\text{Li}^+$  from Joung and Chetatham III *et al.*<sup>53</sup> and the self terms from  $\text{Mg}^{2+}$  from the work of Li *et al.*<sup>88</sup> The MB-NB-fix parameters are chosen following the method described in section ?? . The Grotz *et al.* parameters for  $\text{Mg}^{2+}$  only change the cross-term for OW- $\text{Mg}^{2+}$ , and were computed using LB-rules to mix the self-terms from Grotz *et al.*<sup>89</sup> with those of SPC/E water, without changing the cross-terms with anything else in the system.  $\epsilon$  are in units of /Kj/mol and  $\sigma$  are presented in units of /nm.

Atom type	$\text{Li}^+$				$\text{Mg}^{2+}$					
	LB-Rules		MB-NB-fix		LB-Rules		MB-NB-fix		Grotz <i>et al.</i>	
	$\epsilon$	$\sigma$	$\epsilon$	$\sigma$	$\epsilon$	$\sigma$	$\epsilon$	$\sigma$	$\epsilon$	$\sigma$
CH3	1.07485	0.25797	0.99872	0.30898	0.19239	0.30856	0.68709	0.14257	0.68709	0.14257
CH2	0.75411	0.27432	1.05729	0.20001	0.13238	0.32468	0.63126	0.20617	0.63126	0.20617
OA	1.09408	0.21821	2.91925	0.20020	0.19044	0.26890	5.05190	0.26223	5.05190	0.26223
P	1.85667	0.23975	6.99324	0.21844	0.32318	0.29044	3.89200	0.27811	3.89200	0.27811
OM*	1.19328	0.21400	0.23749	0.20015	0.20771	0.26469	3.22262	0.17691	3.22262	0.17691
CO*	0.35344	0.29727	0.48204	0.35920	0.06152	0.34796	0.56152	0.37127	0.56152	0.37127
O*	1.19328	0.21400	0.06248	0.20068	0.20771	0.26469	2.43058	0.13069	2.43058	0.13069
OW	0.95709	0.22875	0.95709	0.22875	0.16659	0.27944	0.16659	0.27944	13.75000	0.21010



electron densities for each system are shown in figure 3.3. We compare all form-factors for

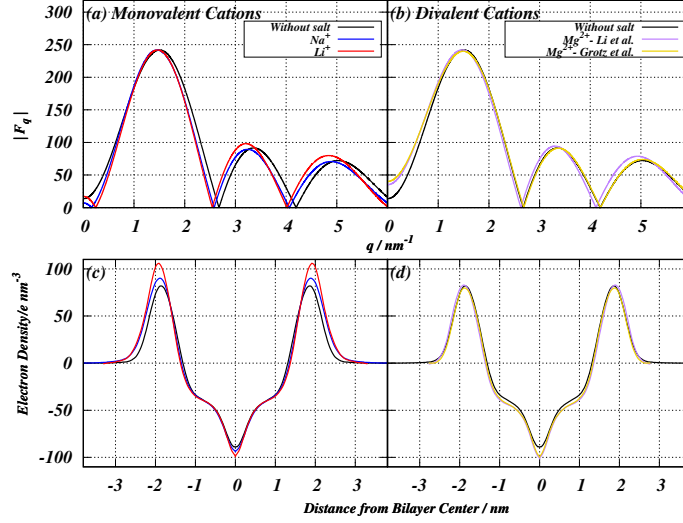


Figure 3.3: Comparison of x-ray scattering formfactors (a,b) and associated electron densities (c,d) for simulated systems. The system with  $\text{Li}^+$  salt has a slightly thicker bilayer compared to  $\text{Na}^+$  and the simulation without salt (a,c) and,  $\text{Mg}^{2+}$  does not significantly change the bilayer thickness under any parameter set studied (b,d).

each system to that of a system simulated without salt, published in our previous work.<sup>33</sup> The bilayer thickness  $D_{\text{hh}}$  is determined by measuring the distance between the peaks in the electron density, which roughly localize the electron-dense phosphates in the lipid headgroup – the values for this can be seen in table 3.4.

Experiments often report various types of thicknesses, volumes, and cross-sectional areas that are model dependent. We also compute these quantities to compare the simulation results with experiments. These values are presented in table 3.4. Based on the  $D_{\text{hh}}$  and the  $2D_{\text{C}}$  there is a slight thickening of the bilayer in the  $\text{Li}^+$  simulation above that seen in the  $\text{Na}^+$  simulation. The  $\text{Mg}^{2+}$  simulations, irrespective of the parameter set, yield much less thickening than the  $\text{Li}^+$  simulation. The volumes per lipid ( $V_{\text{L}}$ ), headgroup ( $V_{\text{H}}$ ), and chains ( $V_{\text{C}}$ ) are computed using the method of Petrache *et al.*<sup>42</sup> This is done by optimizing the function:

$$\Omega(v_i) = \sum_{z_j}^{\rho_s} \left( 1 - \sum_{i=1}^{N_{\text{Groups}}} (\rho_i(z_j) v_i)^2 \right), \quad (3.1)$$

Table 3.4: Bilayer simulation details, and structural parameters. Here we detail the various structural measurements of each simulated bilayer.  $D_{hh}$  is the distance measured between the peaks in the electron density, which localize the electron-dense phosphate moiety in the lipid headgroup.  $D_B$  is a distance between the Gibb’s surfaces<sup>41</sup> on the probability density of solvent as it approaches the lipid bilayer.  $2D_C$  is the distance between the Gibb’s surfaces on the probability density of lipid chains, and represents the lipid chain thickness. Volume per lipid  $V_L$  is measured by dividing the volume of the entire system into solvent and ions, and lipid following the method by Petrache *et al.*<sup>42</sup>. This  $V_L$  is the sum of the  $V_H$  and  $V_C$ , which are the volume per lipid headgroup and volume per lipid chains respectively. Area per lipid molecule  $A_L$  is computed as the ratio of twice the lipid chain volume  $V_C$  with  $2D_C$ . We also report the position of the hydration boundary of each system, which we compute as the point where the second water order parameter  $P_2(\cos(\beta)) \approx 0$  as was done in Saunders *et al.* 2019<sup>34</sup>.

	No Salt	Na <sup>+</sup>	Li <sup>+</sup>	Mg <sup>2+</sup> -Li <i>et al.</i>	Mg <sup>2+</sup> -Grotz <i>et al.</i>
$D_{hh}(\text{nm})$	$3.744 \pm 0.107$	$3.764 \pm 0.088$	$3.864 \pm 0.070$	$3.832 \pm 0.364$	$3.768 \pm 0.525$
$D_B(\text{nm})$	$3.654 \pm 0.047$	$3.936 \pm 0.043$	$4.511 \pm 0.048$	$4.325 \pm 0.044$	$4.213 \pm 0.049$
$2D_C(\text{nm})$	$2.707 \pm 0.034$	$2.897 \pm 0.034$	$3.015 \pm 0.034$	$2.880 \pm 0.029$	$2.809 \pm 0.032$
$V_L(\times 10^{-3}\text{nm}^3)$	$1215.57 \pm 1.0$	$1211.32 \pm 1.21$	$1201.2 \pm 1.05$	$1219.8 \pm 1.24$	$1227.7 \pm 1.24$
$V_H(\times 10^{-3}\text{nm}^3)$	$310.68 \pm 1.14$	$314.81 \pm 0.75$	$306.0 \pm 1.01$	$324.0 \pm 1.26$	$327.9 \pm 1.10$
$V_C(\times 10^{-3}\text{nm}^3)$	$904.89 \pm 1.28$	$896.50 \pm 1.19$	$895.3 \pm 0.91$	$895.8 \pm 1.05$	$899.8 \pm 1.06$
$A_L(\times 10^{-2}\text{nm}^2)$	$66.86 \pm 0.85$	$61.89 \pm 0.73$	$59.39 \pm 0.69$	$62.21 \pm 0.63$	$64.35 \pm 0.82$
Hydration Boundary (nm)	2.79	3.69	3.63	3.48	3.33

where  $\rho_i(z_j)$  is the number density of the  $i$  component in the  $z_j$  slice of the box and  $v_i$  is the corresponding partial component volume.  $N_{\text{Groups}}$  is the number of atom groups for which we are dividing the system volume into component volumes – we have groups for solvent plus ions, lipid chain without the terminal methyls ( $\text{CH}^*$ ), terminal methyls ( $\text{CH}_3$ ), and the lipid headgroups (H). The lipid volumes are then computed as

$$V_C = N_{\text{CH}^*} \times v_{\text{CH}^*} + N_{\text{CH}_3} \times v_{\text{CH}_3} \quad (3.2)$$

and

$$V_H = N_H \times v_{\text{headgroup}}, \quad (3.3)$$

where  $N_{\text{CH}^*} = 30$ ,  $N_{\text{CH}_3} = 2$ ,  $N_H = 20$  are the number of united atoms per atom group for  $\text{CH}^*$ ,  $\text{CH}_3$ , and H. The chain volume  $V_C$  is similar for all systems studied, and there is some variation in the headgroup volume  $V_H$ . However, this method of dividing up the

volume is more prone to errors in the headgroup region due to significant overlap between the headgroup and solvent densities. Thus, we also see similar variation in the total lipid volume  $V_L$ . The two-dimensional area per lipid  $A_L$  is defined as  $\frac{2V_c}{2D_c}$  as is often reported from SAXS and SANS experiments,<sup>40</sup> and is an important measure of how the lipids condense as the bilayer thickens. Both the simulations with  $Mg^{2+}$  yield bilayers with a larger  $A_L$  than the monovalent ions studied in this work, and are closer in area to the simulation without salt.

The detailed structure of molecules and their neighborhoods are often studied using various nuclear magnetic resonance (NMR) techniques. At present, these experiments with various salts are sparse. Thus, we report these data with anticipation that future experiments will fill this gap and validate or invalidate these numbers. Lipid chain ordering is determined via the acyl chain  $S_{CD}$  per carbon atom. These can be seen in figure 3.4.

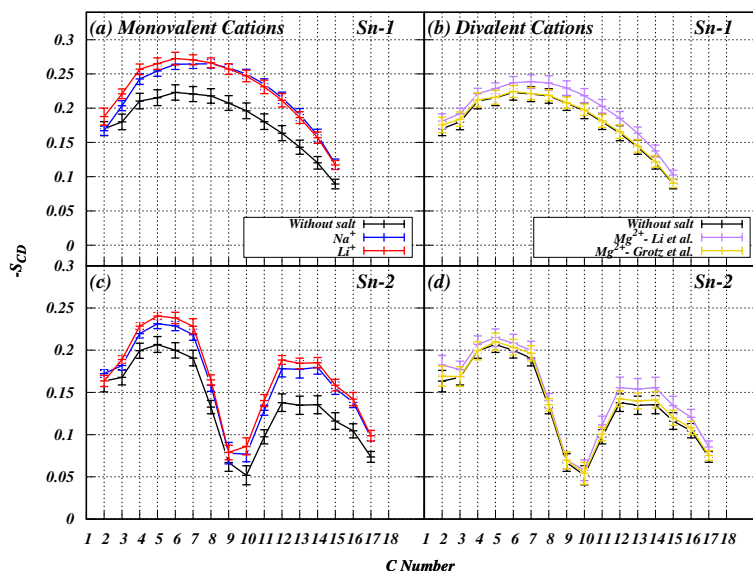


Figure 3.4: Acyl chain carbon-deuterium order parameters. These are computed for the Sn1 and Sn2 chains of each lipid starting at the second carbon in the chain.<sup>67,68</sup> We note that the lipids simulated in systems of monovalent ions (a,c) show a significant increase in the lipid chain ordering for both acyl chains. The systems simulated with  $Mg^{2+}$  (b,d) are much closer in ordering to that of a system simulated without ions.

There is significant increase in chain ordering in the systems with  $Na^+$  and  $Li^+$ , which is consistent with the slight thickening of the bilayer seen in the  $D_B$  values. The less coordinated  $Mg^{2+}$  systems have remained much closer to the ordering seen in the no-salt simulation.

### 3.5 Specific ion adsorption

#### 3.5.1 Bulk ions

Interfaces in salt solutions give rise to a double layer of cations and anions at the surface.<sup>71</sup> Ions in these double layers get stuck to the surface, or adsorb, which is sometimes referred to as specific binding. Zwitterionic lipid bilayers have no net charge before ions are adsorbed, so this adsorption determines the surface charge density on the substrate. This charge is measured experimentally using the electrophoretic mobility of the vesicle. Interpretation of such experiments requires one to define a surface, often called the “slip-surface” where solvent beyond that point can be represented by a dielectric continuum. The electrostatic potential at this surface is the  $\zeta$ -potential. In simulations the interface is not a simple surface, but a region without a clear point of delineation.

#### Hydration boundary

We identify this slip-surface boundary as the point where water orientational ordering is negligible, i.e. beyond the “slip-surface” boundary water quadrupoles are sufficiently isotropic, giving dielectric properties of water similar to that of bulk solvent. We compute this by first dividing the box into slices along the direction normal to the bilayer. For each water within a slice we compute the average value of first and second order legendre polynomial of the cosine of the angle between the box z-axis and the water O-H bond vector, and then average these values over the last 150 ns of simulated time. Figure 3.5 shows the water order parameters as a function of the distance of a slice from the bilayer center.

The first order parameter describes the in-out ordering of the bond vector with respect to the box z-axis – a vector parallel to the axis and pointing normal to the bilayer would have a positive ordering, and a vector pointing into the bilayer would have a negative ordering. We see that waters at the surface of each bilayer have a significant outward orientation at the bilayer surface, and that reverses as we move closer to the bilayer center. When compared to

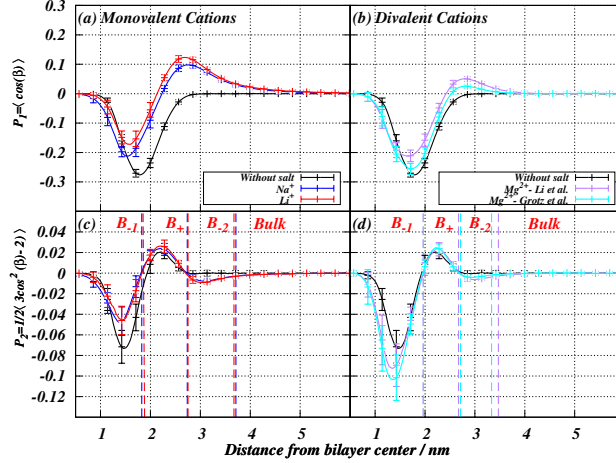


Figure 3.5: Water order parameters. The  $P_1$  and  $P_2$  calculated for monovalent cations (a,c) show greater organization in the bulk region and the  $B_{-2}$  regions, and less organization within the lipid-occupied regions of the system ( $B_+$  and  $B_{-1}$ ) compared to the simulation without salt. On the other hand, with the presence of  $Mg^{2+}$  salts we observe an overall less pronounced effect in the bulk and  $B_{-2}$  regions compared to the system without salt (b,d).

the system simulated without ions, we see that the monovalent ions perturb the water in-out orientation more than  $Mg^{2+}$ , especially in the case of the  $Mg^{2+}$ –Grotz *et al.* parameters.

The second order parameter roughly describes the organization of the quadrupole moments of water, and the value of this parameter can be used to compute the quadrupolar splitting values determined in deuterated water NMR experiments.<sup>70,94</sup> The vertical dotted lines in figure 3.5 denote regions of interest in the bilayer based on the sign of the second order parameter. We call the innermost region of negative ordering  $B_{-1}$ , which ends when the values become positive. This next region of positive ordering is called  $B_+$ , and the following region of negative ordering is  $B_{-2}$ . Each bilayer system with ions has these regions, but they are at differing distances from the bilayer center. It should be noted that beyond the  $B_{-2}$  region the ordering does not abruptly reach zero in the systems simulated with salt.

Figure 3.5 shows monovalent ions have less organization in the  $B_{-1}$  region (inside the lipid headgroup) when compared to that of the divalent ions, whereas in regions  $B_+$  and  $B_{-2}$  (closer to the bilayer surface) the divalent ions show significantly less organization compared to that of monovalent salts. The hydration boundary is determined by fitting an exponential decay

to the second water order parameter starting at the minimum of the  $B_{-2}$  of the histogram. The decay length is used to demarcate the point where the ordering becomes zero – water beyond this region is regarded as bulk solvent. The location of the hydration boundary is noted in figure 3.5, and the distance to this point from the bilayer center is listed in table 3.4.

### Poission-Boltzmann Theory

With the boundary defined, we look to the region of bulk solvent to examine the behavior of ions and ascertain that they follow the predictions of PB-theory.<sup>71</sup> The purpose of this endeavor is to distinguish the ions in bulk solvent from those that are adsorbed, as the density of the adsorbed ions are expected to deviate from PB-theory predictions. We must first compute all the model parameters for the number density and electrostatic potential predicted by PB-theory, and compare our simulation results to this prediction. The PB-theory assumes that the number density of ions follow a Boltzmann distribution:

$$\rho(z) = \rho_0 \exp(-\bar{z}e\beta\psi(z)), \quad (3.4)$$

where  $\rho_0$  is the ion density in the center of the dielectric continuum,  $\bar{z}$  is the valency of the ion,  $\beta = (k_bT)^{-1}$ ,  $e$  is the charge on an electron, and  $\psi(z)$  is the electrostatic potential. The surface is defined by the hydration boundary of each system. The lengths of the solvent occupied regions,  $D$ , in each system is found by measuring the distance across the solvent from the hydration boundary of one leaflet of the bilayer to the other. These values are listed in table 3.5. This places the surfaces at  $z = \pm D/2$  nm, where  $z = 0$  is the center of the

Table 3.5: Poisson-boltzmann theory parameters. These parameters are computed for each simulated system studied (excepting the bulk density ( $\rho_{0,i}$ ), which we fit to our simulation results). These are then used to compute the number density distribution and the electrostatic potential as described by Poisson-Boltzmann theory to compare to our simulation results.  $\sigma$  is the surface charge density of the bilayer, D is the length of the bulk-solvent occupied region of the box, K is the Debye screening length, and  $\rho_{0,i}$  is the number density of the particular ion at the center of bulk solvent.

Parameter	Na <sup>+</sup>	Li <sup>+</sup>	Mg <sup>2+</sup> –Li <i>et al.</i>	Mg <sup>2+</sup> –Grotz <i>et al.</i>
$\sigma(e/nm^2)$	0.161	0.182	0.0690	0.0476
D (nm)	26.927	26.557	26.658	25.226
K (nm <sup>-1</sup> )	3.331	3.333	3.913	3.921
$\rho_{0,cation} (nm^{-3})$	0.059	0.060	0.091	0.092
$\rho_{0,anion} (nm^{-3})$	0.062	0.063	0.183	0.185

solvent-occupied region of the simulation box. The electrostatic potential  $\psi(z)$  is modeled as a sum between two Debye-Huckle potentials:<sup>71</sup>

$$\psi_1(z) = \psi_s \exp\left(-K\left(z + \frac{D}{2}\right)\right) \quad (3.5)$$

$$\psi_2(z) = \psi_s \exp\left(K\left(z - \frac{D}{2}\right)\right) \quad (3.6)$$

$$\psi(z) = \psi_1(z) + \psi_2(z) - (\psi_1(0) + \psi_2(0)), \quad (3.7)$$

where  $\psi_s = \frac{\sigma}{\epsilon_0 \epsilon} K$  is the electrostatic potential at the bilayer surface as defined by the hydration boundary,  $\epsilon$  is the dielectric constant of SPC/E water  $\epsilon = 70.7$ ,<sup>95</sup> and  $\sigma$  is the surface charge density of the bilayer leaflet.<sup>71</sup>

$\sigma$  is determined for each system by integrating the charge density of all species within the hydration boundary on either side of the bilayer. This charge divided by the box area is the surface charge density. These values can be seen in table 3.5. Since our phospholipid is

zwitterionic, all of the surface charge comes from the ions that have accumulated within the hydration boundary (see figure 3.6)

Returning to equation 3.7,  $K$  is the inverse Debye length,

$$K = \sqrt{\sum_i \rho_{0,i} \bar{z}_i^2 \frac{e^2}{\epsilon_0 \epsilon k_b T}}, \quad (3.8)$$

where  $\rho_{0,i}$  is the density of each ion in a given system at the center of bulk solvent. This is taken as an average of the number density of each ion in the solvent occupied region of the box.

Finally, we fit equation 3.4 to the density of anions in bulk solvent via  $\rho_0$ . The comparisons can be seen in figure 3.7. Past the hydration boundary of the lipid bilayer, it can be seen that the density of anions continues to climb monotonically. Additionally, the density of cations drops monotonically to a trough value before climbing closer to the bilayer center, near the phosphate groups (see figure 3.6 and 3.7).

We also compare the electrostatic potential from our simulations to the potential from PB-theory (figure 3.8). The electrostatic potential for each simulated system can be computed by twice integrating the Poisson equation

$$\phi(z) = -\frac{1}{\epsilon_0} \int_0^z \int_0^{z'} \rho(z) dz dz' + C_1 z + C_2. \quad (3.9)$$

We set the boundary conditions that the electric field in bulk solvent must be zero, and the electrostatic potential at the box edge must be zero. The electrostatic potential from simulation agrees well with the prediction from PB-theory.

### 3.5.2 Adsorbed ions

The total number of adsorbed ions are counted as the number of ions within the “slip-surface” or “hydration-boundary” of the bilayer, and further characterization is based on the level of hydration of the ion. Binding constants from the Langmuir Isotherm model are often



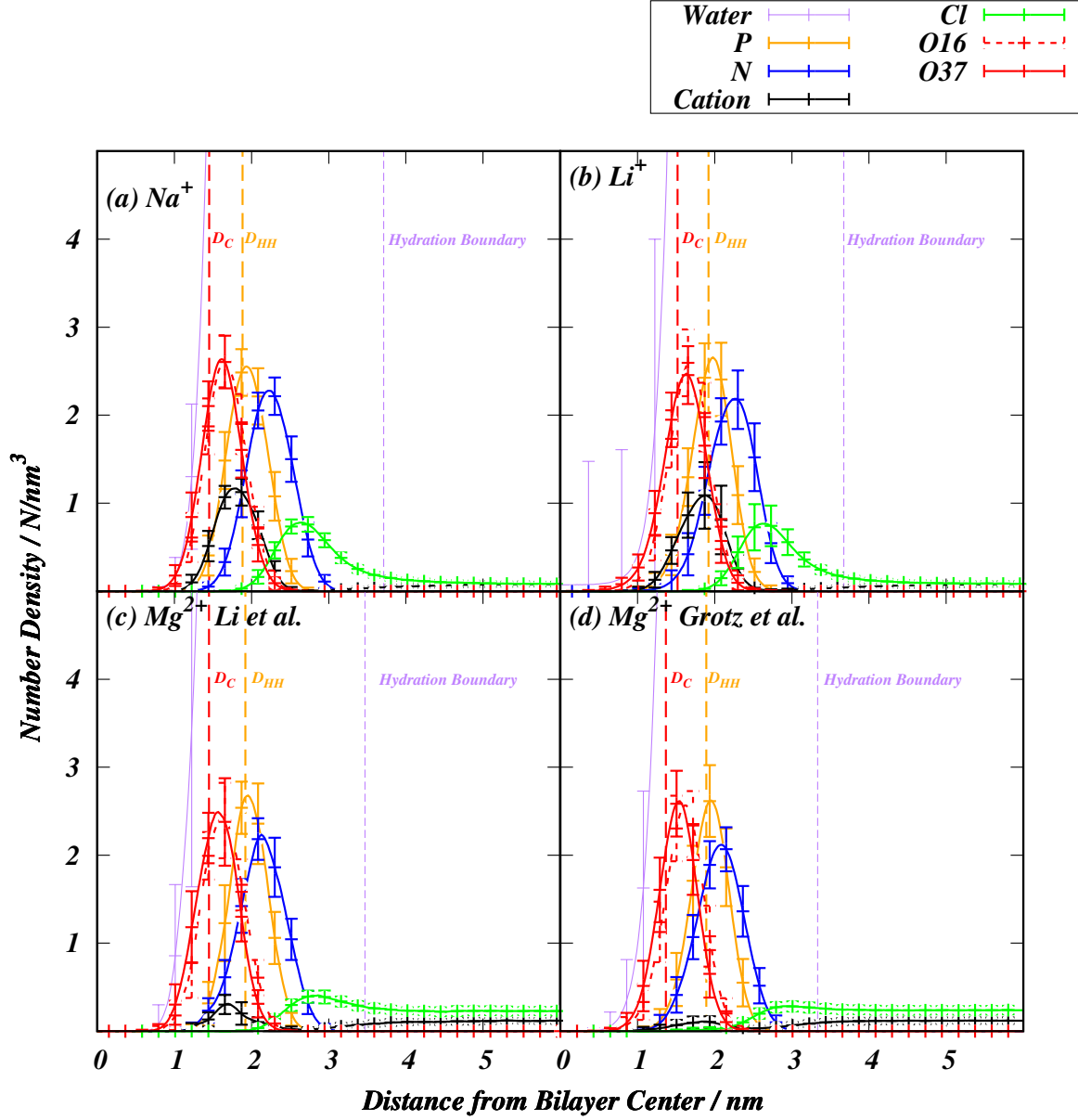


Figure 3.6: Number density of lipid headgroup species and ions near the bilayer interface. (a-b) We report that the monovalent cations show peaks near the phosphate, with accumulation of an anion peak that resembles the double layer. (c-d)  $\text{Mg}^{2+}$  does not show significant accumulation in the lipid bilayer headgroup compared to the monovalent ions, with a similarly small anion peak. However, in all systems studied, ions are accumulated near the phosphorus. Integrating the number density of cations within the hydration boundary, denoted by the purple vertical dashed line, gives the number of ions that are sterically bound. The orange vertical dashed line delineates the  $D_{hh}$  and the red vertical dashes delineate the  $D_C$  of the bilayer.

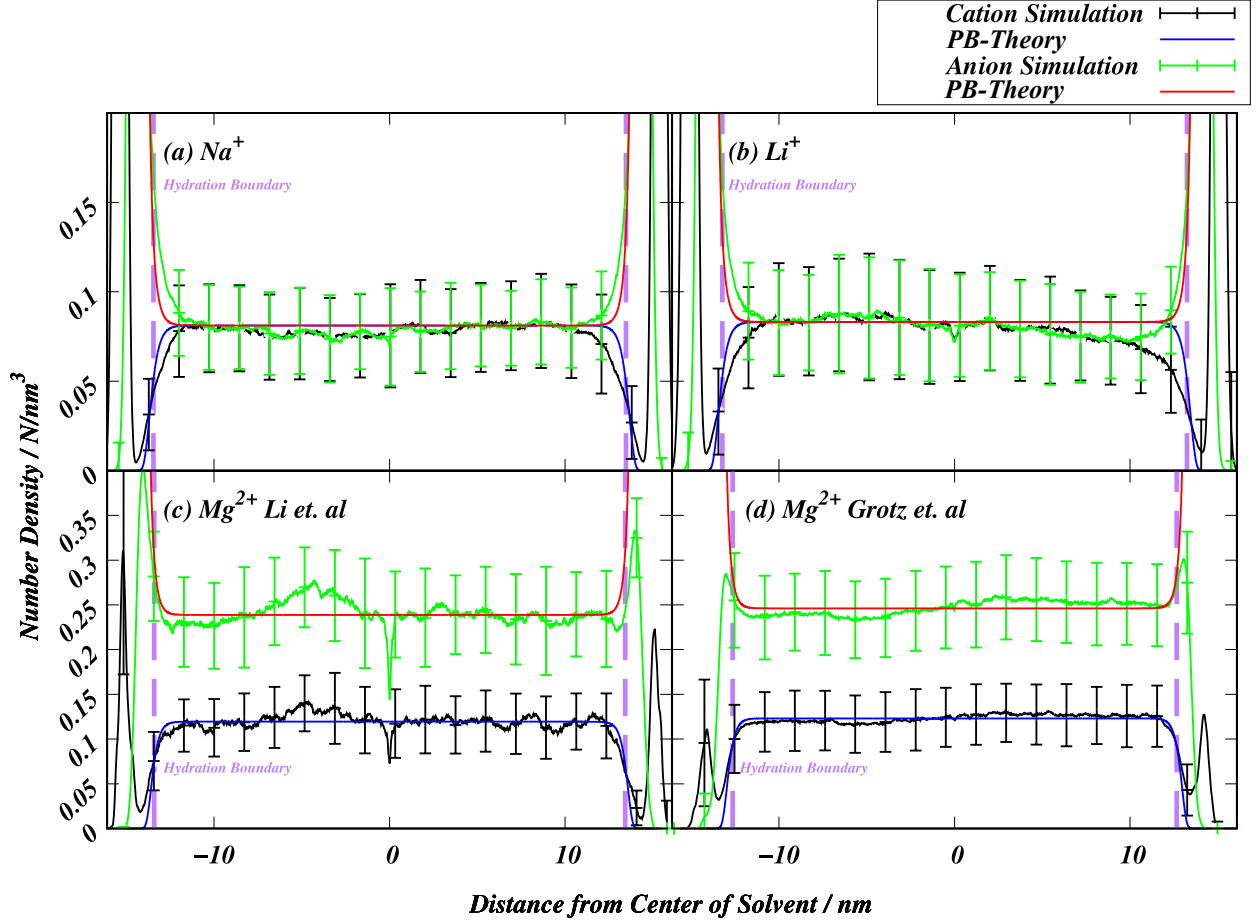


Figure 3.7: Number density of cations and anions in the bulk solvent-occupied region of each simulated system, compared with theoretical predictions from PB-theory for each calculated  $\sigma$ . PB-theory predictions correspond well with the simulation results within the region bounded by the hydration boundary.

computed in experiments to describe ion binding affinity for surfaces; however, this model requires a fixed number of binding sites per lipid. The actual number of binding sites per lipid is not known. Therefore, we report the number of ions adsorbed per lipid ( $\theta$ ), which is related to the binding affinity of each ion for the lipid bilayer. We observe 0.51  $\text{Na}^+$  per lipid bound, 0.57  $\text{Li}^+$  per lipid, 0.13  $\text{Mg}^{2+}$  per lipid in the  $\text{Mg}^{2+}$ -*Li et al.* system, and 0.10  $\text{Mg}^{2+}$  per lipid in the  $\text{Mg}^{2+}$ -*Grotz et al.* system. We see a substantially larger number of  $\text{Na}^+$  and  $\text{Li}^+$  adsorbed per lipid than  $\text{Mg}^{2+}$ , which may be reflective of the amount of space occupied by each ion, and seems to follow the binding modes such that the more dehydrated ions correlate with a larger number of ions adsorbed per lipid. The fraction of cations adsorbed in each

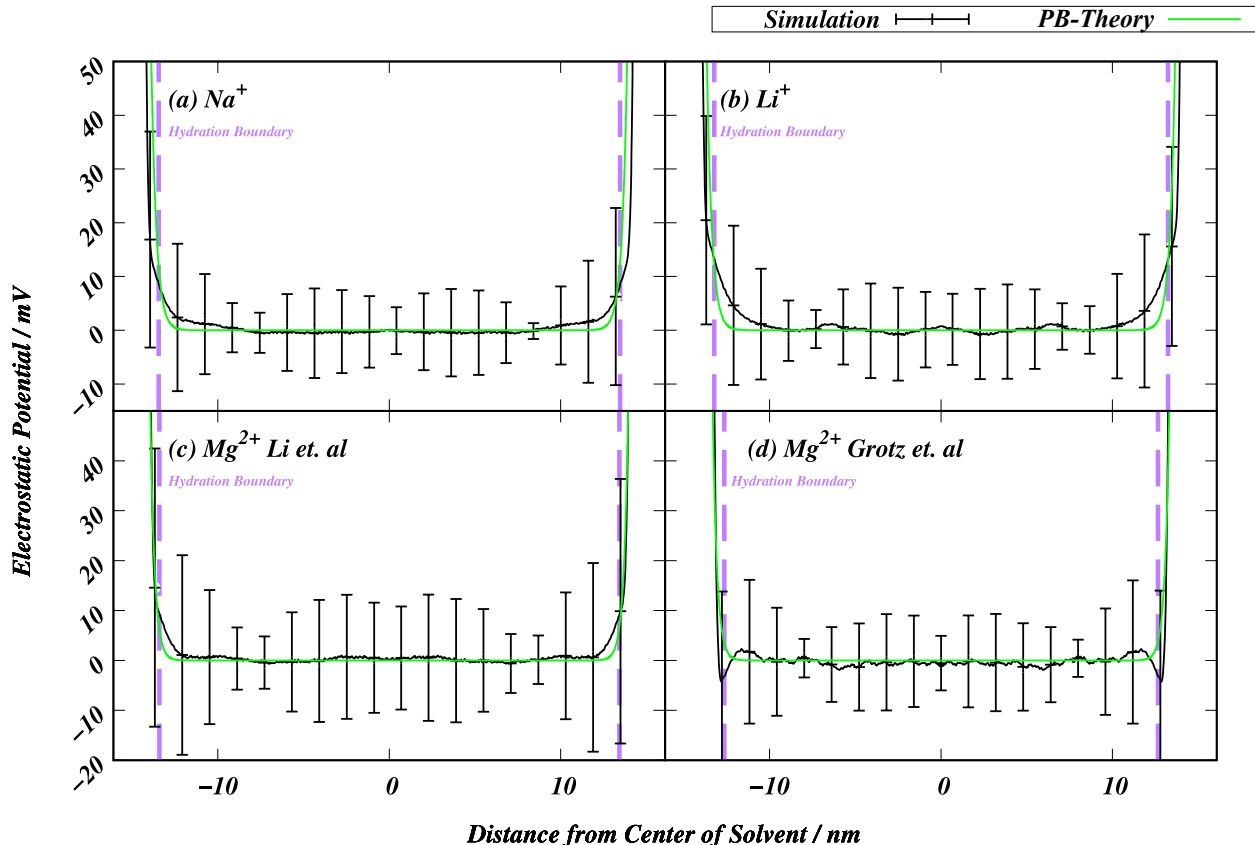


Figure 3.8: Electrostatic potential in the bulk solvent-occupied region compared to predictions from PB-theory. We report good agreement between the theoretical potential shown in green, and the simulation results shown in black, within the region bounded by the hydration bounds of the lipid bilayer.

mode of adsorption can be seen in table 3.6, and the fractions of  $\text{Cl}^-$  anions adsorbed can be seen in table 3.7.  $\text{Cl}^-$  adsorption fractions follow a similar trend to that of the total number of cations bound, but adsorption is almost entirely in the steric modality.

### Adsorption modalities

Further characterization of the adsorbed ions begins by examining the first-shell coordination partners of cations in each system. This can be counted by first determining a cutoff value for the first hydration shell of each ion – the values for this cutoff are 3.2 Å for  $\text{Na}^+$ , 2.7 Å for  $\text{Li}^+$ , 3.3 Å for  $\text{Mg}^{2+}$ , and 3.0 Å for  $\text{Cl}^-$ . These values are determined from radial distribution functions for water oxygen (or water hydrogen in the case of  $\text{Cl}^-$ ) around

Table 3.6: Fractions per lipid of cations perfectly adsorbed, imperfectly adsorbed, sterically adsorbed, and non-adsorbed cations averaged over the last 150 ns of simulation time. These are computed by counting the number of waters in the first-coordination shell of every ion in the simulation box in every frame. For the total number of adsorbed ions, we only check if the ion is within the hydration boundary of the bilayer. We then subtract the number within this region that are completely dehydrated – these are the perfectly adsorbed ions. We further subtract any ions that have lost one or more waters – the imperfectly adsorbed ions. The remaining are considered sterically adsorbed. We also report the total number of bound ions per lipid as a measure of the affinity of the ion to the lipid bilayer – the number of  $\text{Mg}^{2+}$  ions per lipid is fall smaller than that for the more perfectly adsorbed ions  $\text{Li}^+$  and  $\text{Na}^+$ .

Adsorbed cations / lipid	$\text{Na}^+$	$\text{Li}^+$	$\text{Mg}^{2+}$ –Li <i>et al.</i>	$\text{Mg}^{2+}$ –Grotz <i>et al.</i>
Total $\theta$	0.472	0.575	0.129	0.091
Steric $\theta_s$	0.010	0.015	0.116	0.071
Imperfect $\theta_I$	0.068	0.165	0.008	0.020
Perfect $\theta_P$	0.394	0.395	0.005	0.000

Table 3.7: Fractions per lipid of anions perfectly adsorbed, imperfectly adsorbed, sterically adsorbed, and non-adsorbed anions in each simulation, defined in the same way as we define adsorption of cations. These are computed by counting the number of waters in the first-coordination shell of every anion in the simulation box in every frame. For the total number of adsorbed anions, we only check if the anion is within the hydration boundary of the bilayer. We then subtract the number within this region that are completely dehydrated – these are the perfectly adsorbed anions. We futher subtract any ions that have lost one or more waters – the imperfectly adsorbed ions. The remaining are considered sterically adsorbed. We indicate each system by the cation name, as the anion in the system is always  $\text{Cl}^-$ . We note that the anion binding fractions follow the trend seen in the total number of cations bound for each system, due to the formation of the ionic double-layer at the bilayer-water interface. Most anions adsorb sterically in each system, with some adsorbing imperfectly as they approach the positively charged choline trimethylammonium in the lipid headgroup.

Adsorbed anions / lipid	$\text{Cl}^-$ in $\text{Na}^+$ System	$\text{Cl}^-$ in $\text{Li}^+$ System	$\text{Cl}^-$ in $\text{Mg}^{2+}$ –Li <i>et al.</i> System	$\text{Cl}^-$ in $\text{Mg}^{2+}$ –Grotz <i>et al.</i> System
Total $\theta$	0.423	0.463	0.186	0.208
Steric $\theta_s$	0.209	0.213	0.107	0.126
Imperfect $\theta_I$	0.214	0.250	0.079	0.082
Perfect $\theta_P$	0.000	0.000	0.0	0.0

each. This cutoff is used to produce a neighborlist for ions across each simulation in every frame, and count the number of neighbors within this cutoff. These data are histogrammed and averaged over the last 150ns of simulation time. The results for this are presented in figure 3.9.

The number of perfectly adsorbed ions is determined by counting the number of ions without any remaining waters in their first coordination shell. It is observed that in the  $\text{Na}^+$  system, a majority of the ions adsorbed to the bilayer are completely dehydrated. The  $\text{Li}^+$  system has a similar fraction of perfectly adsorbed ions compared to  $\text{Na}^+$ , and practically no perfectly adsorbed ions are seen in any of the  $\text{Mg}^{2+}$  simulations.  $\text{Cl}^-$  anions are not seen adsorbed perfectly in any simulation.

Similarly to the perfect adsorption case, imperfectly adsorbed ions are counted as ions with one or more waters in their first coordination shell, but missing at least one water from the shell. We use the number of coordinating waters of an ion in the bulk solvent region of our simulation as the maximum coordination number for the ion (Figure 7). This gives a coordination number of 4 for  $\text{Li}^+$  and 6 for  $\text{Mg}^{2+}$ . We calculate the number of imperfectly adsorbed ions by counting the number of ions with one or more water missing from their hydration shell, and then subtracting the number of perfectly adsorbed ions. We see more than twice the fraction of these ions in the  $\text{Li}^+$  system compared to the  $\text{Na}^+$  system.  $\text{Mg}^{2+}$  shows an insignificant number of imperfectly adsorbed ions.  $\text{Cl}^-$  adsorbs in a large fraction imperfectly, as they begin to interact with the headgroup trimethylammonium.

The remaining ions are considered sterically adsorbed – this number is whatever ions remain after subtracting the perfect and imperfectly adsorbed ions from the number of overall adsorbed ions based on the position of the hydration boundary.  $\text{Mg}^{2+}$  seems to have most of the ions in this adsorption mode, where  $\text{Na}^+$  and  $\text{Li}^+$  do not adsorb in this way in significant numbers. Additionally,  $\text{Cl}^-$  shows significant steric adsorption.

These data raise the question, what determines the mode of adsorption for a given ion? Since everything else, such as the substrate and the solvent, are held constant, the magnitude

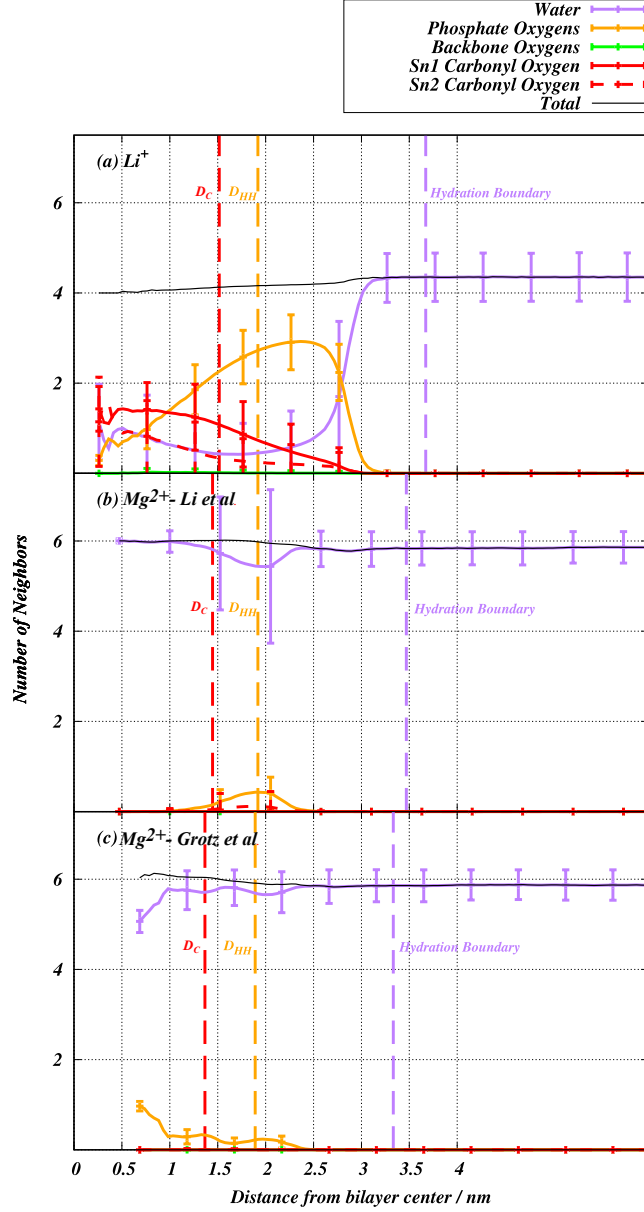


Figure 3.9: First shell coordination partners for  $\text{Li}^+$  and  $\text{Mg}^{2+}$  in each simulation. These are computed over the last 150ns of simulation time in each system by counting the atoms of each species within a cutoff of each ion in the system, and histogramming the data based on the position of the ion. The dotted vertical lines denote the various bilayer surfaces – the vertical black line delineates the hydration boundary of the bilayer, the vertical blue line delineates the  $D_{HH}$ , and the vertical red line delineates the  $D_C$ .  $\text{Li}^+$  (a) retains some water coordination well into the bilayer interface.  $\text{Mg}^{2+}$ -Li *et al.* (b) on the other hand does not lose nearly any first-shell coordinating waters in the bilayer, with some exchange for phosphate oxygens. The  $\text{Mg}^{2+}$ -Grotz *et al.* (c) parameters yield again more exchange but relatively far less than the monovalent ions.

of the electric field at the position of the hydration shell of each ion is all that remains to determine the adsorption modality of the ion (figure 3.10). The electric field strength of each

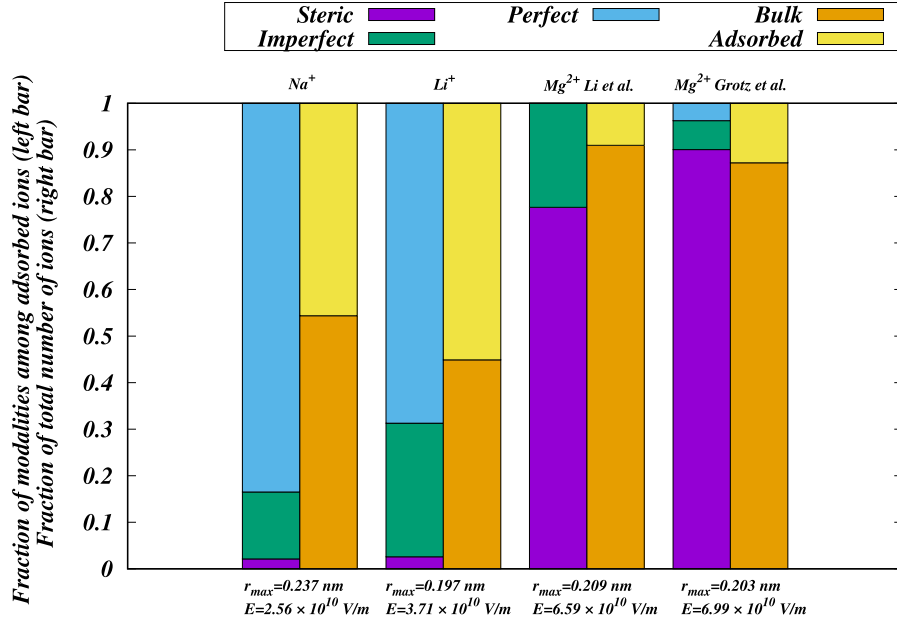


Figure 3.10: Fractions of ion-adsorption modality per each simulated system as a function of electric field strength. Here we show that the fractions of ions adsorbed in each modality follow a trend with an increasing electric field strength at the hydration shell of the cation. The overall trend is that the cations with the weakest field at the hydration shell position adsorb more perfectly, and as the field strength increases more ions adsorb imperfectly and then sterically. We note that little correlation with field strength can be seen in the total number adsorbed per ion.

ion is calculated by applying Coulomb's law to a point charge, placing the test charge at the position of the first hydration shell of the ion in question. We note that the  $Mg^{2+}$ -Li *et al.* ion keeps waters slightly closer in the hydration shell compared to the  $Mg^{2+}$ -Grotz *et al.* model, resulting in a stronger electric field produced at this point by that ion. The largest ion with the smallest charge-density  $Na^+$  dehydrates completely in the largest fraction.  $Li^+$  is smaller, and thus the field near the first shell is stronger and can hold waters a little better than  $Na^+$ .  $Mg^{2+}$  is similar in size to  $Li^+$ , but has a 2+ charge and holds onto waters substantially more than either of the monovalent ions. We also note that the  $\|\vec{E}\|$  does not exhibit strong correlation with the fraction of the total number of ions adsorbed in each system, it only determines the adsorption mode.

### 3.6 Conclusions

Ion adsorption to porous interfaces is a complex interplay between solvent–surface, solvent–ion, and solvent–solvent interactions. With the solvent–surface and solvent–solvent interactions held constant, we identify three different adsorption modalities of ions based on the degree of dehydration of the ion upon adsorption. The binding modality of a particular ion is significantly correlated with the electric field strength of the ion at the position of the first hydration shell, with stronger fields encouraging less dehydration of the ion upon adsorption to the surface (figure 8). This affect appears irrespective of the force-field used in the case of  $\text{Mg}^{2+}$ , which primarily adsorbs in the non-Langmuir type steric modality.

Furthermore, we identify several bilayer structural parameters that can be verified experimentally via x-ray scattering, neutron scattering, or various NMR methods (figures 1, 2, and 3 respectively). While the effect on lipid bilayer structure is not obvious in the electron density (figure 1), the pertubation can be seen in the  $D_B$  and water density – the less hydrated ions induce slight thickening of the lipid bilayer. This is reinforced by the chain ordering, where these ions increase chain ordering (figure 2) while the hydrated ions leave the lipid bilayer structure similar to that of the no-salt case. These two results can be verified experimentally via solvent deuterium NMR, and lipid chain NMR. In the case of POPC, we expect deuterium solvent quadrupolar splitting values will be larger for the less hydrated ions  $\text{Na}^+$  and  $\text{Li}^+$  when compared to the more hydrated  $\text{Mg}^{2+}$  (figure 3). We also expect the lipid chain order parameters to follow the opposite trend, with the monovalent ions inducing more ordering and  $\text{Mg}^{2+}$  inducing a smaller change from the no-salt system. We also expect that the adsorption of  $\text{Mg}^{2+}$  will be less detectable via the electrophoretic mobility of a vesicle in an  $\text{MgCl}$  salt solution, as the energy required to remove a hydrated ion from beneath the slip-surface of a vesicle may be low enough to allow their escape, while a dehydrated ion may remain adsorbed. These experiments are needed to verify these conclusions.



## 4 Alteration of bilayer structure by $\text{Mg}^{2+}$

### 4.1 Abstract

Developing molecular mechanics force fields to model interactions of biological membranes with  $\text{Mg}^{2+}$  cations is challenging. There are no direct estimates of the binding modes of  $\text{Mg}^{2+}$  ions with lipid headgroups or other phosphates in the condensed phase. Experimental data on lipid bilayers in  $\text{Mg}^{2+}$  solution are sparse and limited to biologically relevant but very low ion concentrations. At these concentrations, no statistically discernible effects on bilayer properties are observed. Simulations at these concentrations are difficult due to system size and the extensive conformational sampling required for force-field development. Considering these issues, we previously calibrated  $\text{Mg}^{2+}$ -lipid Lennard-Jones cross-terms using benchmarked quantum mechanical (QM) target data on small clusters of ions and ligands representative of common cation binding sites on 1-palmitoyl-2-oleoyl-sn-glycero-phosphatidylcholine (POPC). Our simulations with these new  $\text{Mg}^{2+}$  parameters yielded bilayer structures very similar to those without salt, in agreement with available experimental data. We adopted this strategy because it worked well for modeling membrane interactions with monovalent cations, for which additional experimental data are available. However, newer studies from our group show that for  $\text{Mg}^{2+}$  ions, the choice of target  $\text{Mg}^{2+}$ -lipid mimetic clusters is non-trivial. Inclusion of fully coordinated (6-fold)  $\text{Mg}^{2+}$  ions, which better represent potential ion-lipid structures in the condensed phase, may be critical for selecting models that reproduce experimental condensed-phase interactions of  $\text{Mg}^{2+}$  with nucleotide phosphates. Using this new protocol, we propose an additional set of  $\text{Mg}^{2+}$ -lipid interaction Lennard-Jones cross-terms. With this parameter set, we find that at concentrations between 100-200 mM, there is a systematic thickening of the lipid bilayer, not observed with our previous  $\text{Mg}^{2+}$ -lipid model. Additionally, compared to the earlier model, we observe more

$\text{Mg}^{2+}$  adsorbed on the bilayer and a larger fraction directly coordinating lipid headgroups. However, the new model does not alter our previous observation that structural changes in the bilayer correlate with the amount of ionic charge directly coordinating lipid molecules.

## 4.2 Introduction

Salts have a well characterized behavior at interfaces in the condensed phase – ions form a classic double layer, where one charge accumulates near the substrate’s surface, and the second charge then accumulates to compensate for that charge.<sup>71</sup> This can be explained using a mean-field approximation. However, the mean-field approximation does not provide details on specific interactions between ionic species and interface moieties. These details are non-trivial, especially in the case of phospholipid membranes, where the substrate itself is liquid and can adopt new conformations in response to ion adsorption.

Molecular dynamics (MD) simulations can, in principle, provide such details. However, the development of MD force fields for  $\text{Mg}^{2+}$ , and modeling their interaction with lipid bilayers poses significant challenges. Firstly, experimental data needed for force field development and validation is scarce. To our knowledge, there are no direct estimates on the binding modes of  $\text{Mg}^{2+}$  ions with lipid headgroups or any other phosphates in the condensed phase. Secondly, the effects of  $\text{Mg}^{2+}$  on lipid bilayer structure are only known for small concentrations of salt.<sup>96,97</sup> Simulations such low salt concentrations push the limits of hardware requirements for conformational sampling and force field testing. For example, in our previous simulations with  $\text{Na}^+$ ,<sup>82</sup> we observed between 75-90  $\text{Na}^+$  ions adsorbed to an equilibrated lipid bilayer of 100 POPC molecules per leaflet. If we assume similar numbers of  $\text{Mg}^{2+}$  to be adsorbed, simulating at a biologically relevant concentration of 0.5 mM<sup>98</sup> will require more than 11 million waters. Additionally, since the residence time of waters in the first shell of  $\text{Mg}^{2+}$  is of the order of a microsecond,<sup>99-101</sup> capturing statistics on water-lipid exchanges in the first shell of  $\text{Mg}^{2+}$  requires prohibitively long MD simulations.

Considering these issues, we previously chose to calibrate  $\text{Mg}^{2+}$ -lipid Lennard-Jones (LJ) terms using benchmarked quantum mechanical (QM) target data clusters of small molecules

representative of the ion binding sites on 1-palmitoyl-2-oleoyl-sn-glycero-phosphatidylcholine (POPC).<sup>82</sup> Methyl acetate (MeAc) and diethyl phosphate (DEPh) were taken as small molecule representatives for lipid headgroups, and we targeted the changes in energy and structure associated with replacing water molecules in  $\text{Mg}^{2+}$ -water clusters with these smaller molecules. Using this model we found that at about 100 mM concentration,  $\text{Mg}^{2+}$  adsorbed into the headgroup region of POPC bilayer, but without losing its inner-shell waters (steric binding mode). We also observed formation of ion double layer at the headgroup-water interface. However,  $\text{Mg}^{2+}$  adsorption had a negligible effect on POPC bilayer structure. We posited that since our model at high salt did not affect bilayer structure, our model at low experimental salt concentration will also not affect POPC bilayer structure; making the result consistent with experiment. We adopted this strategy because we showed that it worked well for modeling interactions of lipid bilayers with monovalent cations.<sup>82</sup> Prior to our development, all simulations, irrespective of the employed force field, reported that monovalent salts thickened POPC bilayers.<sup>33,49,57,102</sup> In contrast, experiments reported insignificant changes in POPC lipid bilayer structure.<sup>51,103</sup> The use of our new  $\text{Na}^+$ -lipid LJ terms resolved this discrepancy to a large extent.<sup>82</sup> Recent developments in our lab, however, motivate us to explore a modified strategy for developing  $\text{Mg}^{2+}$ -lipid LJ terms. Our recent work of polarizable force fields for describing  $\text{Mg}^{2+}$ -protein/nucleotide interactions<sup>104</sup> suggests that perhaps within the classical framework, a single set of force field parameters for  $\text{Mg}^{2+}$  do not perform well at simultaneously reproducing energies of both fully coordinated (6-fold) and partially coordinated  $\text{Mg}^{2+}$  structures. Furthermore, force field developed using 6-fold coordinated structures performed excellently at reproducing not only local interactions of  $\text{Mg}^{2+}$  ions in clusters containing nucleotide phosphates but also condensed phase binding free energies of  $\text{Mg}^{2+}$  ions with nucleotides.<sup>104</sup> We have shown that this strategy also works for other cations<sup>105</sup> Fully coordinated 6-fold clusters of  $\text{Mg}^{2+}$  were not considered in the development of our previous  $\text{Mg}^{2+}$  model,<sup>106</sup> in which target data consisted of only partially coordinated structures of  $\text{Mg}^{2+}$ .

Here we apply this new protocol to develop a new set of  $\text{Mg}^{2+}$ -lipid LJ terms. Our target data consists exclusively of full 6-fold coordinated  $\text{Mg}^{2+}$  clusters with different combinations of waters and MeAc/DEPh ligands representative of the common binding sites on POPC. This allows us to focus our model parametrization on clusters that are more representative of the dense, bulk phase systems that we are interested in studying. As before, target data are obtained from benchmarked quantum mechanical (QM) vdW-inclusive density functional theory (DFT).

Using these new parameters, we perform MD simulations of POPC in  $\text{MgCl}_2$  solution with the aim of comparing these results with those of our previous interaction model parameters. We also characterize their behavior using two different ion-water interaction parameter sets, parameters from Grotz *et al.*<sup>90,107</sup> that are developed to improve the first shell water residence times in comparison to experiments, and parameters from Li *et al.*<sup>108</sup> which target experimental hydration free energies.

In this way, we aim to test how changes to the  $\text{Mg}^{2+}$ -water and  $\text{Mg}^{2+}$ -lipid interaction models affect adsorption behavior and the resulting perturbations to bilayer structure. Our goal is not to validate a specific force field parameterization scheme, but to identify which structural metrics are most sensitive to these parameter choices and to provide a framework for future comparisons with experimental results. Essentially, in absence of appropriate experimental data, we have two competing models for describing  $\text{Mg}^{2+}$ -lipid interactions in MD simulations that point to different adsorption behavior.

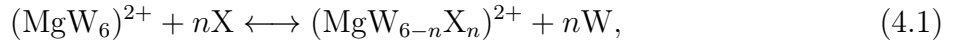
### 4.3 Methods

#### 4.3.1 $\text{Mg}^{2+}$ Model Parameters

We perform a parameter search for the 7 pairs of Lennard-Jones (LJ)  $\sigma_{ij}$  and  $\epsilon_{ij}$  interaction cross-terms of  $\text{Mg}^{2+}$  with lipid headgroup oxygens, carbon, and phosphorus atoms (see Table 4.2). This search is performed using target  $\text{Mg}^{2+}$  clusters containing water molecules and ligands that represent the major cation binding sites in phospholipid headgroups. The

clusters contain exactly 6  $\text{Mg}^{2+}$  coordinators, representing a full first-shell coordination shell of  $\text{Mg}^{2+}$ .

These clusters are geometry optimized following the general procedure described in Chapter 1, and substitution energies are computed as the target data for parameter optimization. As before,<sup>82</sup> we do not use the absolute interaction energies of  $\text{Mg}^{2+}$  clusters. Instead, we target the substitution energy associated with replacing water molecules with ligands  $X$  representing POPC headgroup fragments (methyl acetate or diethyl phosphate):



with

$$\Delta E_{\text{sub}} = E_{\text{MgWX}} + nE_W - E_{\text{MgW}} - nE_X, \quad (4.2)$$

where  $E_{\text{MgW}}$  is the energy of the fully hydrated  $\text{Mg}^{2+}$  cluster,  $E_{\text{MgWX}}$  is the energy of the mixed cluster with  $n$  ligands and  $6 - n$  waters, and  $E_W$  and  $E_X$  are the isolated water and ligand energies, respectively. The substitution energies and corresponding optimized geometries for these clusters are reported in figure and table .

Parameter optimizations were performed using the ParOpt software package developed by our group.<sup>60</sup> We used the Nelder-Mead optimizer to simultaneously optimize the 14 LJ cross terms for each atom type in our target clusters. Constraints are detailed in Table ?? . We first perform parameter searches using a full-random simplex initialization, to obtain 400 converged simplexes, regarding a simplex as converged if the RMSD collapses to  $10 \times 10^{-3}$ . The best parameters from this search are then used to perform another search using around-point initialized simplex, with an RMSD cutoff of  $10 \times 10^{-5}$ , again for 400 converged simplexes. From this search, we select the parameters that balance the error in substitution energies and geometries simultaneously. These optimized parameters are provided in table 4.2. We denote these parameters as the  $\text{Mg}^{2+}$  2025 model, and compare them with our parameters from Saunders *et al.* 2024,<sup>106</sup> which we will refer to as the  $\text{Mg}^{2+}$  2024 model. There are

Table 4.1: Parameter bounds and active constraints.  $\varepsilon$  and  $\sigma$  correspond to Lennard-Jones well depth and size.

Parameter	Min	Max	Additional Constraint
MGCH3- $\varepsilon$	0.0	2.19239	
MGCH3- $\sigma$	0.2	0.5	
MGCH2- $\varepsilon$	0.0	2.13238	
MGCH2- $\sigma$	0.2	0.5	
MGOA- $\varepsilon$	0.0	30.0	
MGOA- $\sigma$	0.2	0.5	
MGP- $\varepsilon$	0.0	30.0	
MGP- $\sigma$	0.2	0.5	
MGOM <sup>*</sup> - $\varepsilon$	0.0	30.0	
MGOM <sup>*</sup> - $\sigma$	0.2	0.5	$\sigma_{\text{MG-OM}^*} = \min \{ \sigma_{\text{MG-P}}, \sigma_{\text{MG-OM}^*} \}$
MGCO <sup>*</sup> - $\varepsilon$	0.0	2.06152	
MGCO <sup>*</sup> - $\sigma$	0.2	0.5	
MGO <sup>*</sup> - $\varepsilon$	0.0	30.0	
MGO <sup>*</sup> - $\sigma$	0.2	0.5	

substantial differences between the  $\text{Mg}^{2+}$  2024 and  $\text{Mg}^{2+}$  2025 models, with the greatest changes in the size of the well depth  $\epsilon_{ij}$  for MG-OA, MG-P, and MG-OM<sup>\*</sup>

The substitution energies before and after optimization are compared to target QM values in Table 4.3. The geometries before and after optimization are compared to QM geometries in figure 4.1.

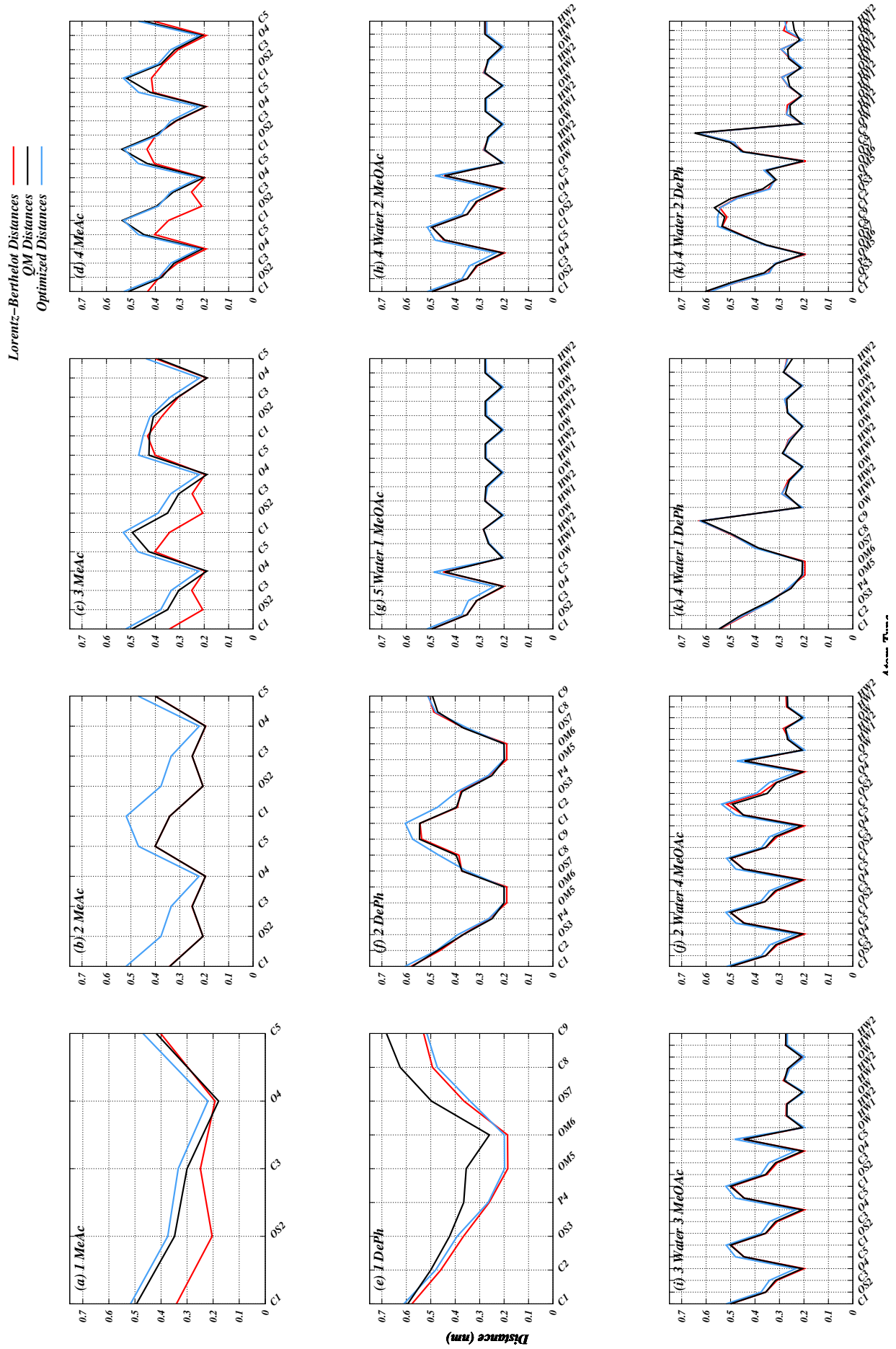


Figure 4.1: Comparison between distances of  $Mg^{2+}$  atom from other atoms in clusters optimized using QM and MM.

We note substantial improvements in both substitution energies with a minimal loss of accuracy in geometries, with parameter optimization reducing mean absolute error in  $\Delta E_{sub}$  from 0.26 to 0.01.

Table 4.2: Lennard-Jones parameters for magnesium interactions: well depth  $\epsilon_{ij}$  (kJ/mol) and distance parameter  $\sigma_{ij}$  (nm), comparing the 2025 optimized model, the 2024 model, and the original LB-rules.

	<b>2025</b>		<b>2024</b>		<b>LB-rules</b>	
Parameter	$\epsilon$	$\sigma$	$\epsilon$	$\sigma$	$\epsilon$	$\sigma$
MG-CH3	0.60498	0.22161	0.68709	0.14257	0.19239	0.30856
MG-CH2	1.36553	0.41404	0.63126	0.20617	0.13238	0.32468
MG-OA	25.25725	0.30372	5.05190	0.26223	0.19044	0.26890
MG-P	29.74732	0.23348	3.89200	0.27811	0.32318	0.29044
MG-OM <sup>*</sup>	22.04699	0.20018	3.22262	0.17691	0.20771	0.26469
MG-CO <sup>*</sup>	0.57040	0.42212	0.56152	0.37127	0.06152	0.34796
MG-O <sup>*</sup>	2.06827	0.24468	2.43058	0.13069	0.20771	0.26469



Table 4.3: Energies (kJ/mol) associated with substituting  $n$  water molecules in low coordination clusters, and in 6-fold Mg-water clusters with  $n$  methyl acetates (MeAcs) or  $n$  diethyl phosphates (DEPhs). Substitution energies are defined in equation 4.2.

System	PBE0+VdW			LB Rules			2024			2025		
	Ref.	Energy	Abs.%	MAPE	Energy	Abs.%	MAPE	Energy	Abs.%	MAPE	Energy	Abs.%
1MeOAc	-268.702	-130.319	0.515		-299.844	0.116		-32.724	0.878			
2MeOAc	-449.770	-243.856	0.458		-545.386	0.213		-59.544	0.868			
3MeOAc	-550.360	-263.968	0.520		-598.606	0.088		-42.191	0.923			
4MeOAc	-609.631	-341.534	0.440	0.483	-690.483	0.133	0.137	-98.578	0.838	0.877		
1DEPh	-942.545	-972.812	0.032		-1063.300	0.128		-772.729	0.180			
2DEPh	-1302.053	-1051.842	0.192	0.112	-1488.761	0.143	0.136	-1248.054	0.041	0.111		
5W 1MeOAc	-71.288	-91.759	0.287		-165.829	1.326		-71.280	0.000			
4W 2MeOAc	-127.201	-177.528	0.396		-316.012	1.484		-122.881	0.034			
3W 3MeOAc	-166.160	-253.576	0.526		-402.648	1.423		-167.835	0.010			
2W 4MeOAc	-192.534	-317.715	0.650	0.465	-507.049	1.634	1.467	-192.275	0.001	0.011		
4W 1DEPh	-775.546	-640.060	0.175		-848.090	0.094		-754.821	0.027			
4W 2DEPh	-1279.754	-1198.284	0.064	0.119	-1519.772	0.188	0.141	-1333.653	0.042	0.034		

Table 4.4: Shifts in substitution energies relative to LB Rules:  $\Delta E_{\text{sub}}^{202X} - \Delta E_{\text{sub}}^{\text{LB}}$  for 2024 and 2025, and their difference [2025–2024]. Positive values mean 202X is less stabilizing (less negative) than LB; negative values mean more stabilizing than LB.

Cluster	$\Delta E_{\text{sub}}^{2024} - \Delta E_{\text{sub}}^{\text{LB}}$	$\Delta E_{\text{sub}}^{2025} - \Delta E_{\text{sub}}^{\text{LB}}$	[2025–2024]
1MeOAc	–169.525	97.595	267.120
2MeOAc	–301.531	184.311	485.842
3MeOAc	–334.638	221.777	556.414
4MeOAc	–348.949	242.956	591.905
5W 1MeOAc	–74.071	20.479	94.550
4W 2MeOAc	–138.484	54.647	193.131
3W 3MeOAc	–149.072	85.741	234.813
2W 4MeOAc	–189.334	125.440	314.774
1DEPh	–90.488	200.083	290.571
2DEPh	–436.919	–196.211	240.708
4W 1DEPh	–208.031	–114.761	93.270
4W 2DEPh	–321.488	–135.369	186.119

### 4.3.2 Bilayer Construction

Simulation systems are prepared following the general procedure in Chapter 1.<sup>106</sup> Each system contains 200 POPC lipids (100 per leaflet) and 60,000 waters. To achieve a starting concentration of 200 mM  $\text{MgCl}_2$ , 216 waters are replaced with  $\text{Mg}^{2+}$  and 432 with  $\text{Cl}^-$ . These configurations are used for both the  $\text{Mg}^{2+}$ 2025 HFE and micro simulations.

### 4.3.3 Molecular Dynamics

Two 1  $\mu\text{s}$  production simulations are performed using the  $\text{Mg}^{2+}$ 2025 parameters: one with the water- $\text{Mg}^{2+}$  interaction term from the HFE model of Li *et al.*,<sup>108</sup> and one with the  $\text{Mg}^{2+}$  micro model of Grotz *et al.*<sup>90,107</sup> Lipid interactions are described with the gromos43A1-S3 force field.<sup>26</sup> Trajectory analysis is carried out with GROMACS built-in tools, in-house code using the GROMACS API, and the MDAnalysis Python package.<sup>91,92</sup>

## 4.4 Results and Discussion

### 4.4.1 Water structure, and hydration boundaries

To differentiate interfacial ions from those in the bulk solvent, we first need to define an interfacial boundary. As before,<sup>106</sup> we do this using the orientational ordering of water molecules. Waters near the lipid bilayer interface are ordered due to the electrostatic and steric interactions with the lipid bilayer, as well as interactions with dissolved salts. The orientation of these waters can be probed by computing the orientational order parameters  $P_1 = \langle \cos \beta \rangle$  and  $P_2 = \langle \frac{1}{2}(3 \cos^2 \beta - 1) \rangle$ , where  $\beta$  is the angle made between the water OW-HW1 vector and the box z-axis. The hydration boundary marks the location where water molecules become orientationally isotropic, beyond which they no longer contribute to quadrupolar NMR splitting. We use this boundary to distinguish between adsorbed ions and ions in bulk solvent. In our previous work,<sup>106</sup> we demonstrated that ion densities outside this boundary follow Poisson-Boltzmann theory, while those inside deviate from it. This breakdown in mean-field behavior indicates a specific interaction with the membrane.

To compute  $P_1$  and  $P_2$ , we divide the simulation unit cell into 2000 slices along the membrane transverse (z-) axis. The average values over the last 150 ns of the simulation are plotted in figure 4.2, with points shown for every 200 slices.

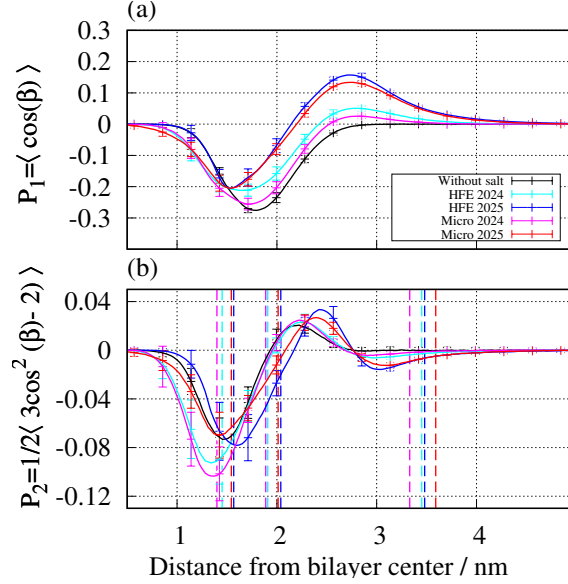


Figure 4.2: Water orientation order parameters. The first order parameter represents an in-out ordering with respect to the bilayer center, and the second is related to the orientation of the quadrupole moment of the box. A value of zero is completely parallel with the box axis. The first order parameter indicates a significant increase in the positive ordering induced by the  $\text{Mg}^{2+}$  2025 parameters compared to the no-salt and the  $\text{Mg}^{2+}$  2024 simulations. The second order parameter indicates increased ordering as one approaches the bilayer starting from the boundary with bulk solvent, indicated by the set of dotted lines furthest from the bilayer center point. Ordering increases as we approach the bilayer  $D_{hh}$ , indicated by the second set of dotted lines. There is also a steeper decline as one follows the plot into the acyl chain region denoted by the bilayer  $2D_C$  – denoted by the innermost dotted lines – in the  $\text{Mg}^{2+}$  2025 Micro system. We note that the hydration boundary of both of the 2025 simulations is further from the bilayer center compared to the 2024 simulations, resulting in a larger region of biological water at the bilayer surface. This alone can result in a greater number of ions adsorbed in at least the *steric* adsorption mode.

The histogram of  $P_2$  is used to calculate the *hydration boundary* of the lipid bilayer system. The outermost region of negative ordering is fitted to an exponential function, and the length scale of the exponential is used to find the location where  $P_2$  is considered to be effectively zero. Lines to delimit these values are drawn on the plot in figure 4.2, and these positions are noted for each bilayer in table 4.5.

Table 4.5: Bilayer structural parameters. The bilayer hydration boundary is defined as the position away from the bilayer center beyond which solvent is isotropic, and denotes bulk solvent from bound solvent. The number of adsorbed charges in each adsorption mode are within the hydration boundary of the system, and are further classified by the degree of loss of hydration water – steric adsorbed have lost no water, imperfect have lost at least one, and perfect have replaced all water oxygens for lipid oxygens. The bilayer thickness  $D_{hh}$  is defined as the distance between the peaks in the electron density of the system, roughly localizing the phosphate groups.  $2D_C$  is the thickness of the acyl-chain region of the bilayer, and is measured as the distance between the Gibb’s surfaces of the acyl-chain probability density. Lipid component volumes  $V_{CH3}$  and  $V_{CH1/CH2}$  are computed using the method of Petrache *et al.*<sup>42</sup>  $V_C$  is computed from the component volumes by multiplying by the number of these components in each acyl chain.  $A_L = \frac{V_C}{D_C}$  is the two-dimensional area occupied per lipid on the bilayer surface. We note a correlation between simulations with larger numbers of adsorbed charges and perturbation of the bilayer structure from that of the simulation without salt, especially in the bilayer  $2D_C$ .

	Without salt	Mg <sup>2+</sup> 2024 HFE	Mg <sup>2+</sup> 2024 Micro	Mg <sup>2+</sup> 2025 HFE	Mg <sup>2+</sup> 2025 Micro
Hydration Boundary (Å)	N/A	34.5	33.3	34.8	35.9
Perfectly Adsorbed Charges	0	1.90	0.00	0.00	0.00
Imperfectly Adsorbed Charges	0	3.68	6.23	28.43	96.93
Sterically Adsorbed Charges	0	37.11	31.45	106.00	20.11
$D_{HH}$ (Å)	$37.57 \pm 1.27$	$38.15 \pm 1.20$	$37.75 \pm 1.19$	$40.75 \pm 0.92$	$40.26 \pm 0.96$
$2D_C$ (Å)	$26.98 \pm 0.35$	$28.99 \pm 0.31$	$28.08 \pm 0.40$	$31.45 \pm 0.29$	$30.84 \pm 0.29$
$V_{CH1/CH2}$ (Å <sup>3</sup> )	$26.33 \pm 0.05$	$26.21 \pm 0.05$	$26.33 \pm 0.05$	$26.22 \pm 0.04$	$26.12 \pm 0.04$
$V_{CH3}$ (Å <sup>3</sup> )	$54.97 \pm 0.39$	$54.77 \pm 0.39$	$54.98 \pm 0.40$	$54.74 \pm 0.24$	$55.19 \pm 0.26$
$V_C$ (Å <sup>3</sup> )	$899.72 \pm 1.01$	$895.85 \pm 1.05$	$899.83 \pm 1.06$	$895.94 \pm 0.95$	$894.00 \pm 1.11$
$A_L = \frac{V_C}{D_C}$	$66.71 \pm 0.89$	$61.80 \pm 0.66$	$64.10 \pm 0.92$	$56.97 \pm 0.54$	$57.98 \pm 0.57$

## 4.5 Mg<sup>2+</sup> Adsorption Behavior

We classify any ion within the hydration boundary as at least sterically adsorbed, with further distinction – steric, imperfect, or perfect – based on how much dehydration the ion undergoes when approaching the bilayer center. A *perfectly* adsorbed ion has lost all waters in its first hydration shell and an *imperfectly* adsorbed ion has lost at least one water from its first coordination shell. *Sterically* adsorbed waters have their first shell of waters intact, but they are spatially located within the *hydration boundary* of the lipid bilayer. To evaluate this, we define a cutoff to the first hydration shell, computed from radial distribution functions. The cutoff used for Mg<sup>2+</sup> in all systems is 3.3 Å, which captures the first peak for Mg<sup>2+</sup> and

lipid oxygens, water, and  $\text{Cl}^-$ . We compute the nearest oxygens (lipid phosphate, glycerol, ester fragment,  $\text{Cl}^-$ , or water) within these cutoffs of cations across the simulation system, and generate a histogram averaged over slices and then over the last 150 ns of simulation time. This histogram is shown in figure 4.3.

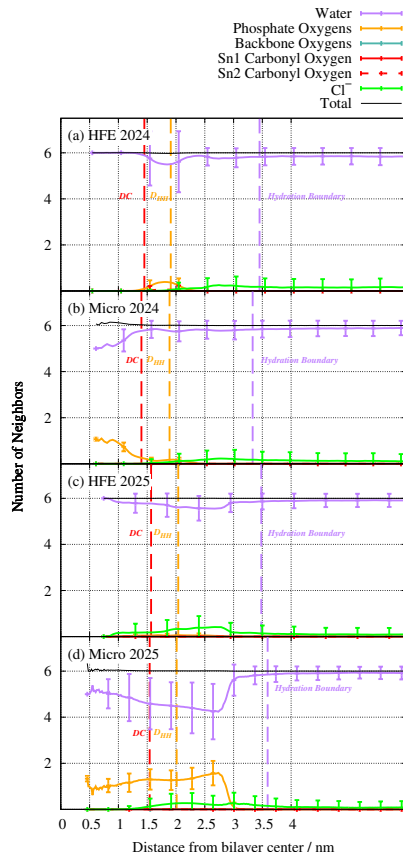


Figure 4.3: Coordination partners of  $\text{Mg}^{2+}$ . We note that while the Micro water with the 2024 parameters do result in some dehydration of the  $\text{Mg}^{2+}$  in the headgroup region of the bilayer, both 2024 parameters yield nearly no dehydration of  $\text{Mg}^{2+}$  at any location in the simulation box. The 2025 HFE parameters still largely do not dehydrate, but the 2025 Micro parameters do result in loss of 1-2 waters from the  $\text{Mg}^{2+}$  coordination shell within the headgroup region. We see substantial interaction with the headgroup phosphate oxygens, and no significant interaction with the glycerol or ester linkage oxygens. We also note the increased interaction with  $\text{Cl}^-$  in the simulations using the 2025 parameters compared to both simulations with the 2024 parameters. The number of first shell  $\text{Cl}^-$  remains below one per ion in any simulation.

We note that the  $\text{Mg}^{2+}$  2024 parameters result in very little dehydration of ions, throughout the simulation box. The 2025 parameters result in loss of 1-2 waters as the ion approaches

the bilayer center, with the  $\text{Mg}^{2+}$  2025 Micro parameters resulting in the greatest degree of dehydration among parameter sets. The  $\text{Mg}^{2+}$  2025 HFE parameters result in some loss of first shell water, but no replacement in the first shell with lipid oxygens. There are a significant number of  $\text{Mg}^{2+}\text{-Cl}^-$  pairs, where a single  $\text{Cl}^-$  replaces a water in the first shell of  $\text{Mg}^{2+}$  as the ion moves into the lipid-occupied region of the bilayer. If these ions do not otherwise lose water for lipid parts, they are counted as *sterically* adsorbed.

The  $\text{Mg}^{2+}$  2025 Micro parameters appear to have a preference for direct interaction with the phosphate group oxygens when dehydrated, and none of the  $\text{Mg}^{2+}$  parameters studied result in significant direct interaction with the ester fragment and glycerol oxygens. There are also far fewer pairs with  $\text{Cl}^-$  under this parameter set. Fractions of ions in each adsorption mode have been computed by counting the number of ions in each frame within the hydration boundary, and the number of those that have lost one water, or all of their waters. We compute averages over the last 150ns, and then fractions of the total adsorbed ions present in each mode. These values are shown in figure 4.4, alongside the fraction of ions adsorbed vs the fraction remaining in bulk solvent.

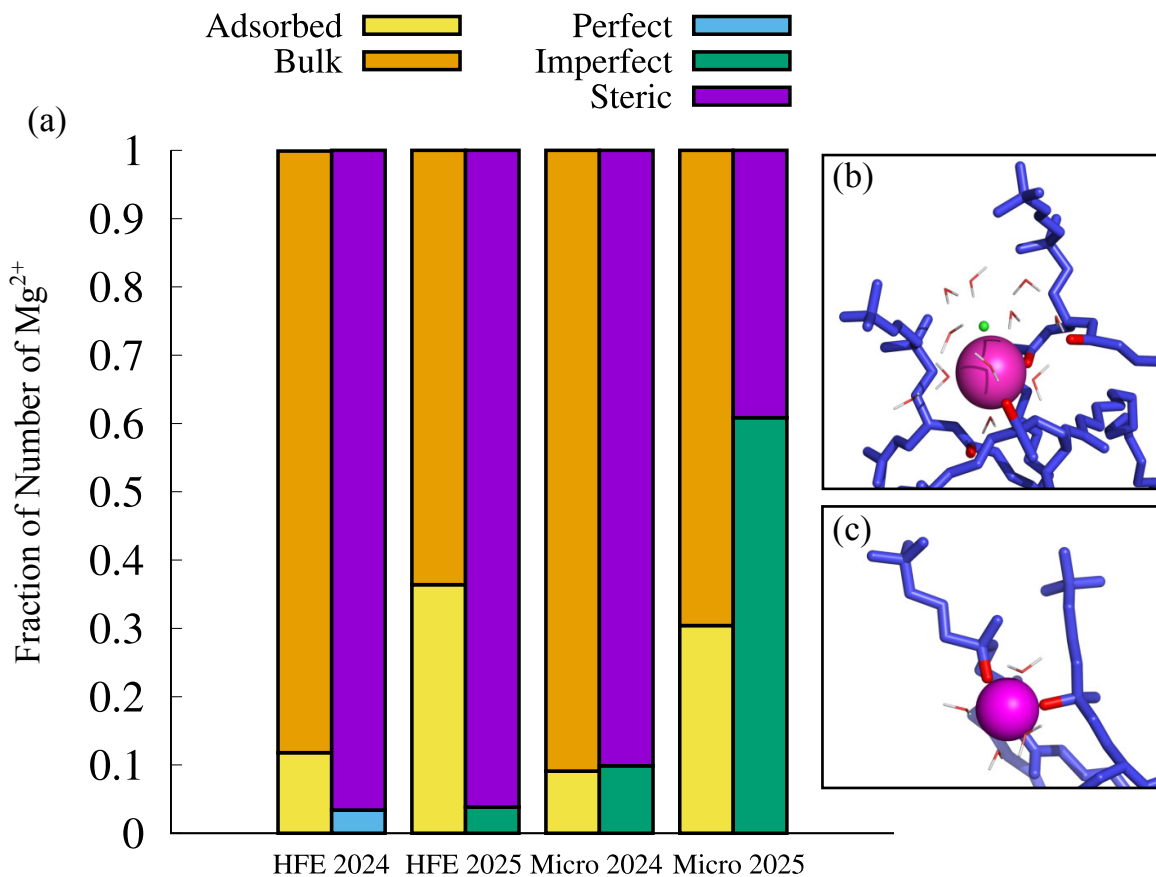


Figure 4.4: (a) Distribution of  $\text{Mg}^{2+}$  ions in different membrane adsorption modes.  $\text{Mg}^{2+}$  are first classified into those in bulk and those adsorbed in membranes. Among those adsorbed in membrane,  $\text{Mg}^{2+}$  are further classified into those that are perfectly, imperfectly and sterically adsorbed. We note that compared to the 2024 models, the 2025 models result in increased membrane adsorption, and among the adsorbed  $\text{Mg}^{2+}$ , the 2025 models result in increased direct coordination with lipid headgroups. Next to the plot, we show examples of  $\text{Mg}^{2+}$  in the *steric* (b) and *imperfect* (c) adsorption modes from our simulations. The *perfect* adsorption mode does not occur in a significant frequency in  $\text{Mg}^{2+}$ , so an example is not included. We note that in this example of the *steric* adsorption mode (b) there is a  $\text{Cl}^-$  (green) included in the hydration shell of the  $\text{Mg}^{2+}$  ion (magenta). This is an example of a partial-ion pair, which while having lost a water from the first-shell, it is not coordinating lipid components directly – these are counted as sterically adsorbed.

The 2025 parameters result in significantly more adsorbed ions and as a result more adsorbed charges in both cases, with the most increased in the  $\text{Mg}^{2+}$  2025 HFE simulation. We count the number of adsorbed charges in each adsorption mode by multiplying the number of ions in each mode by their charge; this would be 2 charges per  $\text{Mg}^{2+}$ , and a  $\text{Mg}^{2+}$  paired with a  $\text{Cl}^-$  counts a single charge. These numbers can be seen in table 4.5 rows 2-4. We also



note an increase in imperfectly adsorbed ions in the  $\text{Mg}^{2+}$  2025 HFE simulation. However, the  $\text{Mg}^{2+}$  2025 Micro parameters result in ions shifting to the majority in the imperfect adsorption mode from the steric mode seen in both 2024 simulations. The  $\text{Mg}^{2+}$  2025 HFE parameters still remain with the largest fraction of ions in the steric adsorption mode. These differences in the distribution of adsorbed  $\text{Mg}^{2+}$  ions – particularly the rise in imperfect adsorption for  $\text{Mg}^{2+}$  2025 Micro – raises the question of how such interactions reshape the membrane itself. We therefore turn to a structural analysis of the lipid bilayer to evaluate the consequences of these adsorption patterns.

#### 4.6 Bilayer Structure

The effect of changes in ion adsorption on bilayer structure was assessed through several structural parameters. Electron densities were computed using the `gmx density` tool included in the GROMACS software suite. Histograms were calculated in 1 ns chunks along the bilayer normal (z-axis) and centered at zero using the position of minimum density, corresponding approximately to the bilayer midplane. These histograms were then symmetrized about the center and averaged over the final 150 ns of each trajectory.

From the resulting profiles, we calculated the small-angle X-ray scattering (SAXS) form factor by subtracting the average water electron density and applying a cosine transform. Electron density profiles and corresponding simulated SAXS form factors are shown in Figure 4.5.

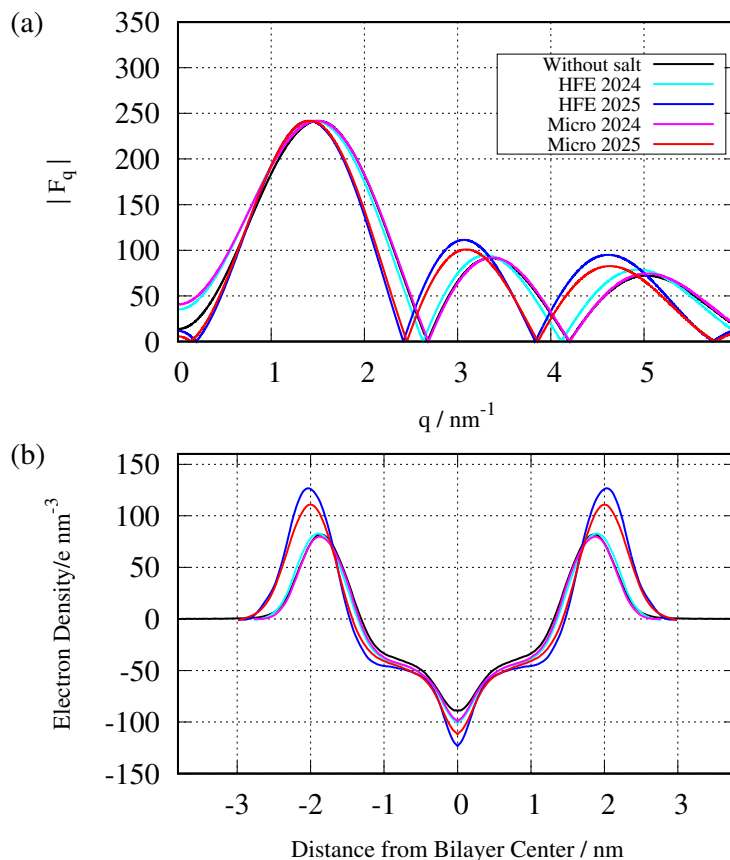


Figure 4.5: SAXS form-factors and associated electron densities for  $\text{Mg}^{2+}$  simulations. (a)  $\text{Mg}^{2+}$  2024 under both Micro and HFE has little effect in changing the bilayer form-factor compared to that of the no-salt simulation, consistent with the available experimental results at lower ion concentrations. Conversely, both of the simulations with 2025 parameters result in significant thickening of the bilayer. This is also seen in the associated electron densities (b), where we see much taller peaks that are further apart in the  $\text{Mg}^{2+}$  2025 simulations than that obtained from the 2024 simulations.

We note significant broadening of the bilayer peak-to-peak distance in the electron densities of the 2025 systems, compared to the 2024 systems. Additional structural parameters are computed from the various number density histograms of our simulations. Similarly to the electron densities, we use the gromacs GMX density tool to compute the number density histogram over 1ns chunks of our simulation. We then center these histograms using the centerpoint found from the electron density at each 1ns chunk. These histograms are then symmetrized, and averaged over the last 150ns of simulation time. These can be seen for solvent and lipid headgroup components of in figure 4.6. We note greater accumulation of

$\text{Mg}^{2+}$  in the  $\text{Mg}^{2+}$  2025 simulations, with greater peak densities of cations in the headgroup regions, with the largest peak in the  $\text{Mg}^{2+}$  2025 HFE system.

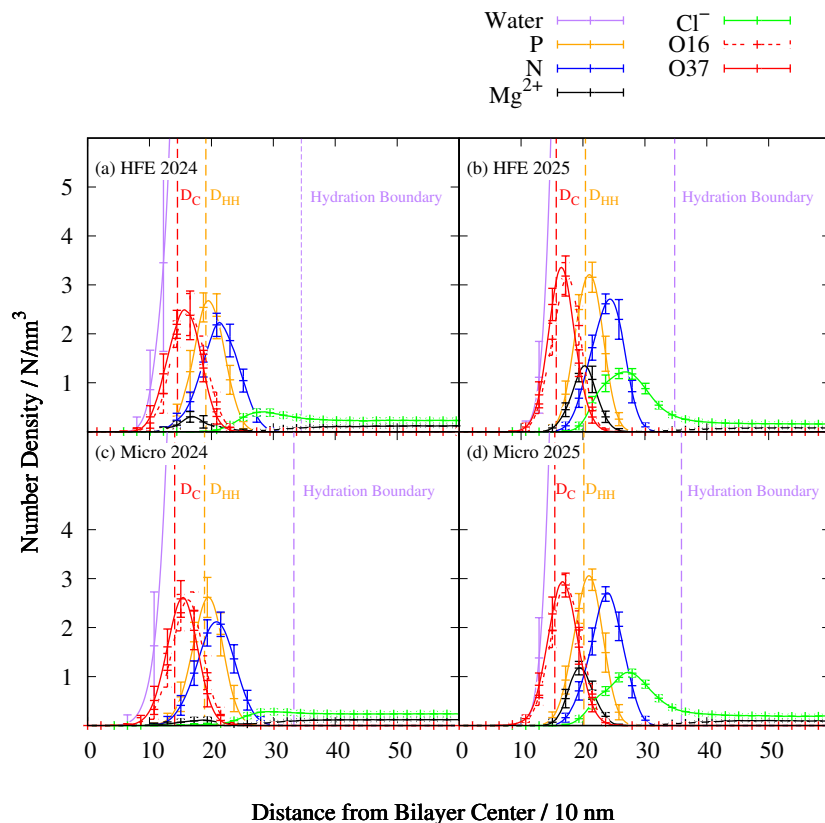


Figure 4.6: Number density histograms of lipid headgroup components. Vertical lines denote the bilayer structural features such as the hydration boundary in purple, the  $D_{hh}$  in orange and the  $2D_C$  in red. We note that within the hydration boundary of each system there is accumulation of ions – anions accumulate near the trimethylammonium nitrogen and cations accumulate near the phosphate group. The  $\text{Mg}^{2+}$  2025 parameters have a much larger accumulation of both ions in the headgroup region of the bilayer compared to the  $\text{Mg}^{2+}$  2024 systems.

The bilayer thickness  $D_B$  and the acyl-chain region thickness  $2D_C$  are computed as the distance between the Gibb’s surfaces of the probability densities of solvent and the lipid acyl-chain carbons, respectively.<sup>41</sup> These are computed from the number densities of these species for each 1ns chunk of the simulation, and then averaged over the last 150ns of the simulation time. The values for these are listed in table 4.5. We also compute the lipid component volumes using the method of Petrache *et al.*<sup>42</sup> To do this, we partition the lipid

number densities into headgroup and chains, with the headgroup consisting of any particles above the acyl chain ester fragment and the chains as just the acyl chain carbons. We partition the chains into groups of CH<sub>2</sub>+CH<sub>1</sub>, and the terminal CH<sub>3</sub> atoms. We optimize the following objective function to partition the volume in each histogram slice  $z_j$  from the number densities to these groups:

$$\Omega(v_i) = \sum_{z_j}^{\rho_s} \left( 1 - \sum_{i=1}^{N_{\text{groups}}} (\rho_i(z_j)(v_i)^2) \right). \quad (4.3)$$

From this we obtain partial volumes for the groups  $v_{\text{CH1\&CH2}}$ ,  $v_{\text{CH3}}$ ,  $v_{\text{Headgroup}}$ . We equate the  $V_{\text{CH2}} = v_{\text{CH1\&CH2}}$  as these densities have significant overlap, and thus the volumes cannot be separated. This, along with the  $V_{\text{CH3}} = v_{\text{CH3}}$  can be seen in table 4.5. These volumes multiplied by the number of each moiety in a lipid are used to compute  $V_C$ . Finally, we compute the  $A_L$  as the ratio  $2 \times V_c / 2D_C$ .

#### 4.6.1 Acyl-Chain order parameters

Acyl-chain order parameters are computed using the method outlined by Douliez *et al.*<sup>68</sup> (see figure ). We note that the 2024 Mg<sup>2+</sup> parameters do not significantly increase the acyl-chain ordering from that of the system simulated without salt. The 2025 Mg<sup>2+</sup> parameters have a much greater effect on the ordering. We can compute the lipid bilayer thickness using the acyl-chain order parameter by using the "first-order mean-torque model" of Petrache *et al.*<sup>40,109</sup> This is done by taking the average  $S_{\text{CD}}$  from the experimental plateau region – the set of carbons where the experimental  $S_{\text{CD}}$  does not change detectably.<sup>40,110</sup> This can be used to compute the average segmental projection onto the bilayer normal  $\langle x \rangle$ :

$$\langle x \rangle = 1 - \frac{1}{\varepsilon_1}, \varepsilon_1 = \frac{2}{1 - \sqrt{\frac{-8\langle S_{\text{CD}} \rangle - 1}{3}}}, \quad (4.4)$$

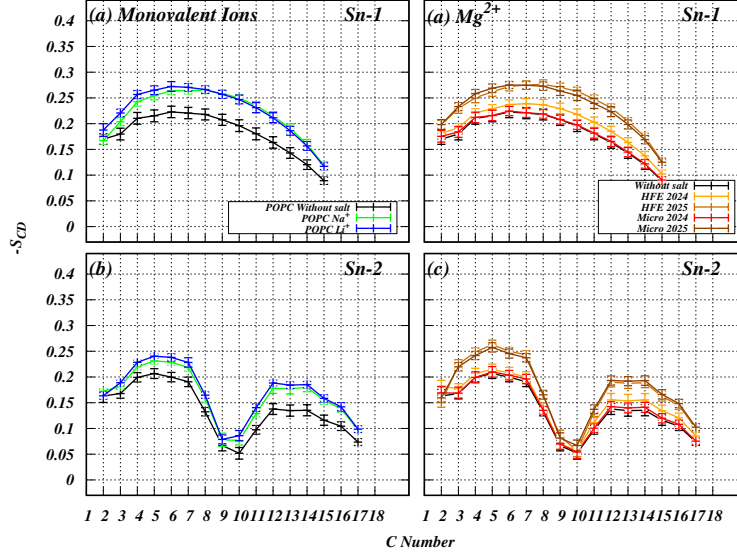


Figure 4.7: Acyl-chain CD Order parameters. We note increased ordering in the simulations using the 2025 model parameters, while the 2024 parameters result in bilayers that remain very similar to the simulation without salt.

where  $\varepsilon_1$  is the mean-torque parameter. We compute the corresponding squared projection  $\langle x^2 \rangle$  from the  $S_{CD}$  using the following equation:

$$\langle x^2 \rangle = \frac{1 - 4\langle S_{CD} \rangle}{3}, \quad (4.5)$$

which can be used together to compute the area factor:

$$q = 3 - 3\langle x \rangle + \langle x^2 \rangle. \quad (4.6)$$

This is then used to compute both the area per lipid and the thickness of the acyl-chain region of the lipid bilayer:

$$\langle A \rangle = q \frac{4V_{CH_2}}{D_M}, \quad (4.7)$$

Using  $V_{CH_2}$  computed from the number densities, and the bond length  $D_M = 2.54$ . We approximate the  $V_{CH_2}$  in two ways from the  $v_{CH_2\&CH_1}$  – first by directly using  $V_{CH_2} =$

$v_{CH2\&CH1}$ , and second by using the common approximation of  $\frac{V_{CH2}=v_{CH3}}{2}$ .<sup>40</sup> These values are listed in table 4.6. We can also compute the acyl chain thickness:

$$D_C = \frac{n_c D_M}{2q}, \quad (4.8)$$

with  $n_c = 16$  as the number of carbons in the Sn-1 chain. These values can be seen in table 4.6. Notably, the  $2D_C$  for all systems studied is slightly smaller than what we compute from the number densities, but follows similar trends. The  $A_L$  computed here only relies on the volume of the CH2 moiety, and ends up with again quite different results than what we computed from  $2V_C/2D_C$ .

We note that in the systems with the smallest number of adsorbed charges in non-steric modes (perfect and imperfect) – in this case the 2024-Mg<sup>2+</sup> parameters, show the smallest increase in  $2D_C$ . The Mg<sup>2+</sup> 2025 systems have the greatest number of adsorbed charges in non-steric modes, and have the largest increase in  $2D_C$  over the system simulated without salt. We note that this trend is not followed necessarily in the  $D_{hh}$ , which is not a reliable measures of bilayer thickness due to the effect of headgroup tilt angle, and overlapping number densities of water and salt in the headgroup region. Together, we note that the systems with the greatest number of charges in the Langmuir-type (non-steric) modes correlate with an increase the bilayer thickness (figure 4.8)

Table 4.6: Area factor, acyl chain region thickness and area per lipid. These values are computed via the method described in Petrache *et al.*<sup>109</sup> This provides us with another measure of the acyl chain thickness. We note that the thickening of the lipid bilayer remains consistent with the acyl chain thickness  $2D_C$  computed from the number densities.

	2024			2025			
	Without salt	Na <sup>+</sup>	Li <sup>+</sup>	Mg <sup>2+</sup> -HFE	Mg <sup>2+</sup> -Micro	Mg <sup>2+</sup> -HFE	Mg <sup>2+</sup> -Micro
$q$	$1.39 \pm 0.14$	$1.30 \pm 0.11$	$1.29 \pm 0.02$	$1.36 \pm 0.02$	$1.41 \pm 0.03$	$1.24 \pm 0.01$	$1.26 \pm 0.01$
$2D_C$ NMR (Å)	$28.67 \pm 2.97$	$30.85 \pm 2.57$	$31.53 \pm 0.53$	$29.98 \pm 0.47$	$28.84 \pm 0.57$	$32.66 \pm 0.33$	$32.17 \pm 0.30$
$A_L$ from $v_{CH2\&CH1}$	$55.14 \pm 1.21$	$51.98 \pm 0.69$	$53.13 \pm 0.91$	$55.98 \pm 0.92$	$58.45 \pm 1.16$	$51.37 \pm 0.52$	$51.97 \pm 0.49$
$((V_{CH3}/2)$	$30.87 \pm 0.30$	$29.65 \pm 0.24$	$27.58 \pm 0.19$	$27.40 \pm 0.19$	$27.49 \pm 0.20$	$27.38 \pm 0.13$	$27.59 \pm 0.13$
$A_L$ from $(V_{CH3}/2)$	$68.26 \pm 1.95$	$61.10 \pm 0.99$	$56.02 \pm 1.04$	$58.51 \pm 1.03$	$61.03 \pm 1.35$	$53.67 \pm 0.58$	$54.90 \pm 0.60$

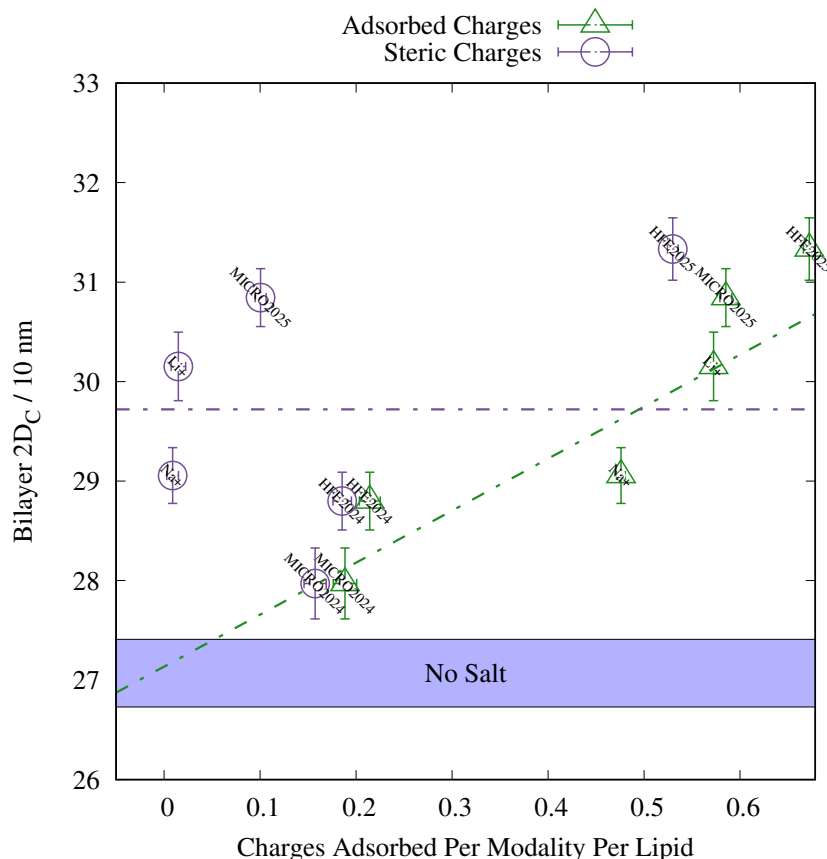


Figure 4.8: Adsorbed charge per adsorption modality per lipid as a function of the lipid bilayer hydrocarbon thickness  $2D_C$ . We compare both our results from this work, and our previous work with monovalent ions.<sup>106</sup> There is a clear trend in the total number of adsorbed charges (i.e. any charges not in bulk solvent), where more charges results in a greater  $2D_C$ . However, if one examines the sterically adsorbed charges, the trend is not as strong. This seems to indicate that the non-steric charges are most responsible for the perturbation of the bilayer thickness from that of the no-salt simulation shown as the blue region on the plot.

## 4.7 Conclusions

We have presented a comparison between two  $Mg^{2+}$  parameter sets developed by our group, under two different water-ion interaction models. The  $Mg^{2+}$  2024 parameters, optimized using clusters of ions and lipid-component ligands at sub-full oxygen coordination of the ion,<sup>106</sup> predict steric adsorption with negligible bilayer thickening. By contrast, the  $Mg^{2+}$  2025 parameters, optimized using fully coordinated clusters by replacing the missing ligand oxygens with waters, similar to sets of target data used to improve parameters for  $Mg^{2+}$ -nucleotide phosphate interactions,<sup>104</sup> yield significantly more ions in non-steric adsorption modes, greater

direct coordination with lipid phosphates, and a correlated increase in bilayer thickness. Both parameter sets reproduce their respective substitution energy targets, but the choice of partially versus fully coordinated clusters leads to divergent predictions for bilayer behavior. This raises a fundamental question about the nature of  $\text{Mg}^{2+}$  adsorption, and potentially of divalent ions in general. Both water-separated and direct-interaction adsorption modes have been described for  $\text{Mg}^{2+}$ -phosphate interactions in biological molecules,<sup>83–86,90,93,107,111,112</sup> and simulations with older ion models tend to favor the water-separated modes.<sup>90,93,107,111,113</sup> With sparse experimental data for lipid bilayers at relevant salt concentrations, it is not yet possible to judge between these models. Thus, the two parameter sets serve as complementary hypotheses and experimental targets, highlighting that the critical open question is not only which parameters best reproduce bilayer structure, but also which underlying reference chemistry most faithfully represents  $\text{Mg}^{2+}$ -lipid interactions in the condensed phase.



## 5 Conclusions

**TODO** We have introduced a framework for classifying ion adsorption at lipid bilayers based on the degree of dehydration observed in molecular dynamics simulations. This classification distinguishes between steric, imperfect, and perfect adsorption modes, corresponding to fully hydrated, partially dehydrated, and completely dehydrated ions within the hydration boundary of the bilayer.

Our results show that the electric field at the hydration shell of an ion correlates strongly with its observed mode of adsorption. Ions with high field strength, such as  $\text{Mg}^{2+}$ , remain hydrated and adsorb sterically. In contrast,  $\text{Na}^+$  and  $\text{Li}^+$  exhibit lower field strengths and bind with partial or full dehydration.

These adsorption modes are predictive of changes to bilayer structure. Systems with larger populations of imperfect or perfectly adsorbed ions display increased lipid chain order and hydrocarbon thickness. Systems dominated by steric adsorption show bilayer structures closer to the no-salt case.

The observed trends hold across multiple force-field parameterizations, including those with differing water-exchange kinetics for  $\text{Mg}^{2+}$ . Poisson–Boltzmann modeling confirms that the accumulation of ions within the hydration boundary is distinct from diffuse ionic layering predicted in the bulk.

Altogether, this work provides a mechanistic link between ion properties and lipid structural response, grounded in simulation observables. It suggests that the strength of ion adsorption—and its structural consequences—can be anticipated from the ion’s electric field without requiring direct tuning to experimental constraints.

## References

- [1] M. Abraham, D. van der Spoel, E. Lindahl, B. Hess, the gromacs development team  
gromacs user manual version 5.1. 2; 2016, MJ Abraham, T. Murtola, R. Schulz, S. Páll,  
JC Smith, B. Hess, E. Lindahl, SoftwareX 1 (2015) 19.
- [2] J. E. Jones, On the determination of molecular fields. i. from the equation of state of  
a gas, Proceedings of the Royal Society of London. Series A 106 (738) (1924) 441–462.  
doi:10.1098/rspa.1924.0081.
- [3] R. A. Buckingham, The classical equation of state of gaseous helium, neon and argon,  
Proceedings of the Royal Society of London. Series A 168 (933) (1938) 264–283. doi:  
10.1098/rspa.1938.0173.
- [4] H. A. Lorentz, Ueber die anwendung des satzes vom virial in der kinetischen theorie der  
gase, Annalen der Physik 248 (1) (1881) 127–136. doi:10.1002/andp.18812480110.
- [5] D. Berthelot, Sur le mélange des gaz, Comptes Rendus de l’Académie des Sciences 126  
(1898) 1703–1855.
- [6] M. Fyta, R. R. Netz, Ionic force field optimization based on single-ion and ion-pair  
solvation properties: Going beyond standard mixing rules, The Journal of chemical  
physics 136 (12) (2012) 124103.
- [7] D. Boda, D. Henderson, The effects of deviations from lorentz–berthelot rules on the  
properties of a simple mixture, Molecular Physics 106 (20) (2008) 2367–2370.
- [8] C. M. Baker, P. E. Lopes, X. Zhu, B. Roux, A. D. MacKerell Jr, Accurate calculation  
of hydration free energies using pair-specific lennard-jones parameters in the charmm

- drude polarizable force field, *Journal of chemical theory and computation* 6 (4) (2010) 1181–1198.
- [9] J. Yoo, A. Aksimentiev, Improved parametrization of  $\text{Li}^+$ ,  $\text{Na}^+$ ,  $\text{K}^+$ , and  $\text{Mg}^{2+}$  ions for all-atom molecular dynamics simulations of nucleic acid systems, *The journal of physical chemistry letters* 3 (1) (2012) 45–50.
- [10] M. Fyta, R. R. Netz, Ionic force field optimization based on single-ion and ion-pair solvation properties: Going beyond standard mixing rules, *The Journal of chemical physics* 136 (12) (2012) 124103.
- [11] S. Mamatkulov, M. Fyta, R. R. Netz, Force fields for divalent cations based on single-ion and ion-pair properties, *The Journal of chemical physics* 138 (2) (2013) 024505.
- [12] R. M. Venable, Y. Luo, K. Gawrisch, B. Roux, R. W. Pastor, Simulations of anionic lipid membranes: development of interaction-specific ion parameters and validation using nmr data, *The journal of physical chemistry B* 117 (35) (2013) 10183–10192.
- [13] A. Savelyev, A. D. MacKerell Jr, Balancing the interactions of ions, water, and dna in the drude polarizable force field, *The Journal of Physical Chemistry B* 118 (24) (2014) 6742–6757.
- [14] H. Li, V. Ngo, M. C. Da Silva, D. R. Salahub, K. Callahan, B. Roux, S. Y. Noskov, Representation of ion–protein interactions using the drude polarizable force-field, *The Journal of Physical Chemistry B* 119 (29) (2015) 9401–9416.
- [15] A. Savelyev, A. D. MacKerell Jr, Competition among  $\text{Li}^+$ ,  $\text{Na}^+$ ,  $\text{K}^+$ , and  $\text{Rb}^+$  monovalent ions for dna in molecular dynamics simulations using the additive charmm36 and drude polarizable force fields, *The Journal of Physical Chemistry B* 119 (12) (2015) 4428–4440.

- [16] Z. Jing, R. Qi, C. Liu, P. Ren, Study of interactions between metal ions and protein model compounds by energy decomposition analyses and the amoeba force field, *The Journal of chemical physics* 147 (16) (2017) 161733.
- [17] M. M. Reif, C. Kallies, V. Knecht, Effect of sodium and chloride binding on a lecithin bilayer. a molecular dynamics study, *Membranes* 7 (1) (2017) 5.
- [18] V. Wineman-Fisher, Y. Al-Hamdani, I. Addou, A. Tkatchenko, S. Varma, Ion-hydroxyl interactions: From high-level quantum benchmarks to transferable polarizable force fields, *Journal of chemical theory and computation* 15 (4) (2019) 2444–2453.
- [19] M. J. Abraham, T. Murtola, R. Schulz, S. Páll, J. C. Smith, B. Hess, E. Lindahl, Gromacs: High performance molecular simulations through multi-level parallelism from laptops to supercomputers, *SoftwareX* 1 (2015) 19–25.
- [20] S. Pall, M. J. Abraham, C. Kutzner, B. Hess, E. Lindahl, Tackling exascale software challenges in molecular dynamics simulations with gromacs, in: *International Conference on Exascale Applications and Software*, Springer, 2014, pp. 3–27.
- [21] D. V. D. Spoel, E. Lindahl, B. Hess, G. Groenhof, A. Mark, H. Berendsen, Gromacs: fast, flexible, free, *J. Comput. Chem.* 26 (2005) 1701.
- [22] E. Lindahl, B. Hess, D. Van Der Spoel, Gromacs 3.0: a package for molecular simulation and trajectory analysis, *Molecular modeling annual* 7 (8) (2001) 306–317.
- [23] H. J. Berendsen, D. van der Spoel, R. van Drunen, Gromacs: a message-passing parallel molecular dynamics implementation, *Computer Physics Communications* 91 (1-3) (1995) 43–56.
- [24] M. J. Abraham, T. Murtola, R. Schulz, S. Páll, J. C. Smith, B. Hess, E. Lindahl, Gromacs: High performance molecular simulations through multi-level parallelism from laptops to supercomputers, *SoftwareX* 1 (2015) 19–25.

- [25] H. Berendsen, J. Grigera, T. Straatsma, The missing term in effective pair potentials, *Journal of Physical Chemistry* 91 (24) (1987) 6269–6271.
- [26] S.-W. Chiu, S. A. Pandit, H. Scott, E. Jakobsson, An improved united atom force field for simulation of mixed lipid bilayers, *The Journal of Physical Chemistry B* 113 (9) (2009) 2748–2763.
- [27] S. Nosé, M. Klein, Constant pressure molecular dynamics for molecular systems, *Molecular Physics* 50 (5) (1983) 1055–1076.
- [28] M. Parrinello, A. Rahman, Polymorphic transitions in single crystals: A new molecular dynamics method, *Journal of Applied physics* 52 (12) (1981) 7182–7190.
- [29] B. Hess, H. Bekker, H. J. C. Berendsen, J. G. E. M. Fraaije, Lincs: A linear constraint solver for molecular simulations, *Journal of Computational Chemistry* 18 (12) (1997) 1463–1472.  
URL [http://dx.doi.org/10.1002/\(SICI\)1096-987X\(199709\)18:12<1463::AID-JCC4>3.0.CO;2-H](http://dx.doi.org/10.1002/(SICI)1096-987X(199709)18:12<1463::AID-JCC4>3.0.CO;2-H)
- [30] U. Essmann, L. Perera, M. L. Berkowitz, T. Darden, H. Lee, L. G. Pedersen, A smooth particle mesh ewald method, *The Journal of chemical physics* 103 (19) (1995) 8577–8593.
- [31] M. L. Berkowitz, *Biomembrane Simulations: Computational Studies of Biological Membranes*, CRC Press, 2019.
- [32] V. Blum, R. Gehrke, F. Hanke, P. Havu, V. Havu, X. Ren, K. Reuter, M. Scheffler, Ab initio molecular simulations with numeric atom-centered orbitals, *Computer Physics Communications* 180 (11) (2009) 2175–2196.
- [33] J. Kruczek, S.-W. Chiu, E. Jakobsson, S. A. Pandit, Effects of lithium and other monovalent ions on palmitoyl oleoyl phosphatidylcholine bilayer, *Langmuir* 33 (4)

- (2017) 1105–1115.  
 URL <http://dx.doi.org/10.1021/acs.langmuir.6b04166>
- [34] M. Saunders, M. Steele, W. Lavigne, S. Varma, S. A. Pandit, Interaction of salt with ether-and ester-linked phospholipid bilayers, *Biochimica et Biophysica Acta (BBA)-Biomembranes* 1861 (5) (2019) 907–915.
  - [35] J. P. Perdew, K. Burke, M. Ernzerhof, Generalized gradient approximation made simple, *Physical review letters* 77 (18) (1996) 3865.
  - [36] C. Adamo, V. Barone, Toward reliable density functional methods without adjustable parameters: The pbe0 model, *The Journal of chemical physics* 110 (13) (1999) 6158–6170.
  - [37] A. Tkatchenko, M. Scheffler, Accurate molecular van der waals interactions from ground-state electron density and free-atom reference data, *Physical review letters* 102 (7) (2009) 073005.
  - [38] V. Wineman-Fisher, J. M. Delgado, P. R. Nagy, E. Jakobsson, S. A. Pandit, S. Varma, Transferable interactions of  $\text{Li}^+$  and  $\text{Mg}^{2+}$  ions in polarizable models, *The Journal of Chemical Physics* 153 (10) (2020) 104113.
  - [39] V. Wineman-Fisher, Y. Al-Hamdani, P. R. Nagy, A. Tkatchenko, S. Varma, Improved description of ligand polarization enhances transferability of ion–ligand interactions, *The Journal of Chemical Physics* 153 (9) (2020) 094115.
  - [40] J. F. Nagle, S. Tristram-Nagle, Structure of lipid bilayers, *Biochimica et Biophysica Acta (BBA)-Reviews on Biomembranes* 1469 (3) (2000) 159–195.
  - [41] J. C. Fogarty, M. Arjunwadkar, S. A. Pandit, J. Pan, Atomically detailed lipid bilayer models for the interpretation of small angle neutron and x-ray scattering data, *Biochimica et Biophysica Acta (BBA)-Biomembranes* 1848 (2) (2015) 662–672.

- [42] H. I. Petrache, S. E. Feller, J. F. Nagle, Determination of component volumes of lipid bilayers from simulations., *Biophysical Journal* 72 (5) (1997) 2237–2242.  
URL <http://www.ncbi.nlm.nih.gov/pmc/articles/PMC1184418/>
- [43] S. A. Pandit, H. L. Scott, Simulations and models of lipid bilayers, in: *Soft Matter: Lipid Bilayers and Red Blood Cells*, Vol. 4, Wiley Online Library, 2008, Ch. 1, pp. 1–82.
- [44] J. Kruczek, S.-W. Chiu, S. Varma, E. Jakobsson, S. A. Pandit, Interactions of monovalent and divalent cations at palmitoyl-oleoyl-phosphatidylcholine interface, *Langmuir* 35 (32) (2019) 10522–10532.
- [45] R. A. Böckmann, A. Hac, T. Heimburg, H. Grubmüller, Effect of sodium chloride on a lipid bilayer, *Biophysical Journal* 85 (3) (2003) 1647–1655.
- [46] A. Cordomi, O. Edholm, J. J. Perez, Effect of ions on a dipalmitoyl phosphatidylcholine bilayer. a molecular dynamics simulation study, *The Journal of Physical Chemistry B* 112 (5) (2008) 1397–1408.
- [47] A. A. Gurtovenko, I. Vattulainen, Effect of nacl and kcl on phosphatidylcholine and phosphatidylethanolamine lipid membranes: insight from atomic-scale simulations for understanding salt-induced effects in the plasma membrane, *The Journal of Physical Chemistry B* 112 (7) (2008) 1953–1962.
- [48] A. Cordomi, O. Edholm, J. J. Perez, Effect of force field parameters on sodium and potassium ion binding to dipalmitoyl phosphatidylcholine bilayers, *Journal of chemical theory and computation* 5 (8) (2009) 2125–2134.
- [49] P. Jurkiewicz, L. Cwiklik, A. Vojtíšková, P. Jungwirth, M. Hof, Structure, dynamics, and hydration of popc/pops bilayers suspended in nacl, kcl, and cscl solutions, *Biochimica et Biophysica Acta (BBA)-Biomembranes* 1818 (3) (2012) 609–616.

- [50] G. Pabst, A. Hodzic, J. Štrancar, S. Danner, M. Rappolt, P. Laggner, Rigidification of neutral lipid bilayers in the presence of salts, *Biophysical journal* 93 (8) (2007) 2688–2696.
- [51] H. I. Petrache, S. Tristram-Nagle, D. Harries, N. Kučerka, J. F. Nagle, V. A. Parsegian, Swelling of phospholipids by monovalent salt, *Journal of lipid research* 47 (2) (2006) 302–309.
- [52] D. Uhríková, N. Kučerka, J. Teixeira, V. Gordeliy, P. Balgavý, Structural changes in dipalmitoylphosphatidylcholine bilayer promoted by  $\text{Ca}^{2+}$  ions: a small-angle neutron scattering study, *Chemistry and physics of lipids* 155 (2) (2008) 80–89.
- [53] I. S. Joung, T. E. Cheatham III, Determination of alkali and halide monovalent ion parameters for use in explicitly solvated biomolecular simulations, *The journal of physical chemistry B* 112 (30) (2008) 9020–9041.
- [54] S. Varma, S. B. Rempe, Multibody effects in ion binding and selectivity, *Biophysical journal* 99 (10) (2010) 3394–3401.
- [55] R. Vácha, P. Jurkiewicz, M. Petrov, M. L. Berkowitz, R. A. Bockmann, J. Barucha-Kraszewska, M. Hof, P. Jungwirth, Mechanism of interaction of monovalent ions with phosphatidylcholine lipid membranes, *The Journal of Physical Chemistry B* 114 (29) (2010) 9504–9509.
- [56] I. Vorobyov, T. W. Allen, The electrostatics of solvent and membrane interfaces and the role of electronic polarizability, *The Journal of Chemical Physics* 132 (18) (2010) 05B602.
- [57] J. Melcr, H. Martinez-Seara, R. Nencini, J. Kolafa, P. Jungwirth, O. S. Ollila, Accurate binding of sodium and calcium to a popc bilayer by effective inclusion of electronic polarization, *The Journal of Physical Chemistry B* 122 (16) (2018) 4546–4557.



- [58] P. Chen, I. Vorobyov, B. Roux, T. W. Allen, Molecular dynamics simulations based on polarizable models show that ion permeation interconverts between different mechanisms as a function of membrane thickness, *The Journal of Physical Chemistry B* 125 (4) (2021) 1020–1035.
- [59] G. Lee Warren, J. E. Davis, S. Patel, Origin and control of superlinear polarizability scaling in chemical potential equalization methods, *The Journal of chemical physics* 128 (14) (2008) 144110.
- [60] J. C. Fogarty, S.-W. Chiu, P. Kirby, E. Jakobsson, S. A. Pandit, Automated optimization of water–water interaction parameters for a coarse-grained model, *The Journal of Physical Chemistry B* 118 (6) (2014) 1603–1611.
- [61] J. C. Fogarty, High Dimensional Non-Linear Optimization of Molecular Models, University of South Florida, 2014.
- [62] S. Varma, S. B. Rempe, Coordination numbers of alkali metal ions in aqueous solutions, *Biophysical chemistry* 124 (3) (2006) 192–199.
- [63] P. Mason, S. Ansell, G. Neilson, Neutron diffraction studies of electrolytes in null water: a direct determination of the first hydration zone of ions, *Journal of Physics: Condensed Matter* 18 (37) (2006) 8437.
- [64] M. Galib, M. Baer, L. Skinner, C. Mundy, T. Huthwelker, G. Schenter, C. Benmore, N. Govind, J. L. Fulton, Revisiting the hydration structure of aqueous  $\text{Na}^+$ , *The Journal of chemical physics* 146 (8) (2017) 084504.
- [65] J. Timko, D. Bucher, S. Kuyucak, Dissociation of  $\text{NaCl}$  in water from ab initio molecular dynamics simulations, *The Journal of chemical physics* 132 (11) (2010) 114510.

- [66] P. Smirnov, Structure of the nearest environment of  $\text{Na}^+$ ,  $\text{K}^+$ ,  $\text{Rb}^+$ , and  $\text{Cs}^+$  ions in oxygen-containing solvents, *Russian Journal of General Chemistry* 90 (9) (2020) 1693–1702.
- [67] E. Egberts, H. Berendsen, Molecular dynamics simulation of a smectic liquid crystal with atomic detail, *The Journal of chemical physics* 89 (6) (1988) 3718–3732.
- [68] J.-P. Douliez, A. Leonard, E. J. Dufourc, Restatement of order parameters in biomembranes: calculation of cc bond order parameters from cd quadrupolar splittings., *Biophysical journal* 68 (5) (1995) 1727.
- [69] S. Varma, S. B. Rempe, Structural transitions in ion coordination driven by changes in competition for ligand binding, *Journal of the American Chemical Society* 130 (46) (2008) 15405–15419.
- [70] K. Åman, E. Lindahl, O. Edholm, P. Håkansson, P.-O. Westlund, Structure and dynamics of interfacial water in an  $\text{l}\alpha$  phase lipid bilayer from molecular dynamics simulations, *Biophysical journal* 84 (1) (2003) 102–115.
- [71] J. N. Israelachvili, *Intermolecular and surface forces*, Academic press, 2011.
- [72] O. Stern, The theory of the electrolytic double-layer, *Z. Elektrochem* 30 (508) (1924) 1014–1020.
- [73] D. C. Grahame, The electrical double layer and the theory of electrocapillarity., *Chemical reviews* 41 (3) (1947) 441–501.
- [74] M. C. Smith, R. M. Crist, J. D. Clogston, S. E. McNeil, Zeta potential: a case study of cationic, anionic, and neutral liposomes, *Analytical and bioanalytical chemistry* 409 (2017) 5779–5787.

- [75] J. Marra, J. Israelachvili, Direct measurements of forces between phosphatidylcholine and phosphatidylethanolamine bilayers in aqueous electrolyte solutions, *Biochemistry* 24 (17) (1985) 4608–4618.
- [76] J. Pan, F. A. Heberle, S. Tristram-Nagle, M. Szymanski, M. Koepfinger, J. Katsaras, N. Kucerka, Molecular structures of fluid phase phosphatidylglycerol bilayers as determined by small angle neutron and x-ray scattering, *Biochimica et Biophysica Acta (BBA)-Biomembranes* 1818 (9) (2012) 2135–2148.
- [77] J. Pan, X. Cheng, F. A. Heberle, B. Mostofian, N. Kucerka, P. Drazba, J. Katsaras, Interactions between ether phospholipids and cholesterol as determined by scattering and molecular dynamics simulations, *The Journal of Physical Chemistry B* 116 (51) (2012) 14829–14838.
- [78] H. Casal, H. Mantsch, H. Hauser, Infrared and  $^{31}\text{P}$ -nmr studies of the interaction of  $\text{Mg}^{2+}$  with phosphatidylserines: effect of hydrocarbon chain unsaturation, *Biochimica et Biophysica Acta (BBA)-Biomembranes* 982 (2) (1989) 228–236.
- [79] S. A. Pandit, D. Bostick, M. L. Berkowitz, Molecular dynamics simulation of a dipalmitoylphosphatidylcholine bilayer with NaCl, *Biophysical Journal* 84 (6) (2003) 3743–3750.
- [80] M. L. Berkowitz, D. L. Bostick, S. Pandit, Aqueous solutions next to phospholipid membrane surfaces: insights from simulations, *Chemical Reviews* 106 (4) (2006) 1527–1539.
- [81] V. Kalinin, C. Radke, An ion-binding model for ionic surfactant adsorption at aqueous-fluid interfaces, *Colloids and Surfaces A: Physicochemical and Engineering Aspects* 114 (1996) 337–350.
- [82] M. Saunders, V. Wineman-Fisher, E. Jakobsson, S. Varma, S. A. Pandit, High-dimensional parameter search method to determine force field mixing terms in molecular simulations, *Langmuir* 38 (9) (2022) 2840–2851.

- [83] J. C. Bowman, T. K. Lenz, N. V. Hud, L. D. Williams, et al., Cations in charge: magnesium ions in rna folding and catalysis, *Current opinion in structural biology* 22 (3) (2012) 262.
- [84] L. Rulíšek, J. Šponer, Outer-shell and inner-shell coordination of phosphate group to hydrated metal ions ( $\text{mg}^{2+}$ ,  $\text{cu}^{2+}$ ,  $\text{zn}^{2+}$ ,  $\text{cd}^{2+}$ ) in the presence and absence of nucleobase. the role of nonelectrostatic effects, *The Journal of Physical Chemistry B* 107 (8) (2003) 1913–1923.
- [85] T. Dudev, Lin, M. Dudev, C. Lim, First- second shell interactions in metal binding sites in proteins: A pdb survey and dft/cdm calculations, *Journal of the American Chemical Society* 125 (10) (2003) 3168–3180.
- [86] D. Pörschke, The mode of  $\text{mg}^{++}$  binding to oligonucleotides. inner sphere complexes as markers for recognition?, *Nucleic Acids Research* 6 (3) (1979) 883–898.
- [87] A. S. Petrov, J. Funseth-Smotzer, G. R. Pack, Computational study of dimethyl phosphate anion and its complexes with water, magnesium, and calcium, *International journal of quantum chemistry* 102 (5) (2005) 645–655.
- [88] P. Li, B. P. Roberts, D. K. Chakravorty, K. M. Merz Jr, Rational design of particle mesh ewald compatible lennard-jones parameters for+ 2 metal cations in explicit solvent, *Journal of chemical theory and computation* 9 (6) (2013) 2733–2748.
- [89] K. K. Grotz, N. Schwierz, Optimized magnesium force field parameters for biomolecular simulations with accurate solvation, ion-binding, and water-exchange properties in spc/e, tip3p-fb, tip4p/2005, tip4p-ew, and tip4p-d, *Journal of Chemical Theory and Computation* 18 (1) (2021) 526–537.
- [90] K. K. Grotz, S. Cruz-León, N. Schwierz, Optimized magnesium force field parameters for biomolecular simulations with accurate solvation, ion-binding, and water-exchange properties, *Journal of Chemical Theory and Computation* 17 (4) (2021) 2530–2540.

- [91] N. Michaud-Agrawal, E. J. Denning, T. B. Woolf, O. Beckstein, Mdanalysis: a toolkit for the analysis of molecular dynamics simulations, *Journal of computational chemistry* 32 (10) (2011) 2319–2327.
- [92] R. J. Gowers, M. Linke, J. Barnoud, T. J. E. Reddy, M. N. Melo, S. L. Seyler, J. Domanski, D. L. Dotson, S. Buchoux, I. M. Kenney, et al., Mdanalysis: a python package for the rapid analysis of molecular dynamics simulations, Tech. rep., Los Alamos National lab.(LANL), Los Alamos, NM (United States) (2019).
- [93] O. Allnér, L. Nilsson, A. Villa, Magnesium ion–water coordination and exchange in biomolecular simulations, *Journal of chemical theory and computation* 8 (4) (2012) 1493–1502.
- [94] J. Kruczek, M. Saunders, M. Khosla, Y. Tu, S. A. Pandit, Molecular dynamics simulations of ether-and ester-linked phospholipids, *Biochimica et Biophysica Acta (BBA)-Biomembranes* 1859 (12) (2017) 2297–2307.
- [95] M. R. Reddy, M. Berkowitz, The dielectric constant of spc/e water, *Chemical physics letters* 155 (2) (1989) 173–176.
- [96] S. Kurakin, O. Ivankov, V. Skoi, A. Kuklin, D. Uhríková, N. Kučerka, Cations do not alter the membrane structure of popc—a lipid with an intermediate area, *Frontiers in Molecular Biosciences* 9 (2022) 926591.
- [97] S. Kurakin, E. Ermakova, A. Ivankov, S. Smerdova, N. Kučerka, The effect of divalent ions on the structure of bilayers in the dimyristoylphosphatidylcholine vesicles, *Journal of Surface Investigation: X-ray, Synchrotron and Neutron Techniques* 15 (2021) 211–220.
- [98] A. Romani, A. Scarpa, Regulation of cell magnesium, *Archives of biochemistry and biophysics* 298 (1) (1992) 1–12.

- [99] J. Neely, R. Connick, Rate of water exchange from hydrated magnesium ion, *Journal of the American Chemical Society* 92 (11) (1970) 3476–3478.
- [100] G. Pálinkás, T. Radnai, Hydration shell structures in an  $\text{mgcl}_2$  solution from x-ray and md studies, *Zeitschrift für Naturforschung A* 37 (1982) 1049–1060, provides structural evidence of a highly rigid, octahedral hydration shell around  $\text{Mg}^{2+}$ , consistent with very long water residence times, though no explicit value is given. doi:10.1515/zna-1982-0912.  
URL [https://consensus.app/papers/hydration-shell-structures-in-an-mgcl2-solution-from-xray-pÁq16b7c39c6b6a50828119dbe4c293bfda/?utm\\_source=chatgpt](https://consensus.app/papers/hydration-shell-structures-in-an-mgcl2-solution-from-xray-pÁq16b7c39c6b6a50828119dbe4c293bfda/?utm_source=chatgpt)
- [101] A. Bleuzen, P.-A. Pittet, L. Helm, A. E. Merbach, Water exchange on magnesium (ii) in aqueous solution: a variable temperature and pressure  $^{17}\text{O}$  nmr study, *Magnetic resonance in chemistry* 35 (11) (1997) 765–773.
- [102] J. N. Sachs, H. Nanda, H. I. Petrache, T. B. Woolf, Changes in phosphatidylcholine headgroup tilt and water order induced by monovalent salts: molecular dynamics simulations, *Biophysical journal* 86 (6) (2004) 3772–3782.
- [103] G. Pabst, A. Hodzic, J. Štrancar, S. Danner, M. Rappolt, P. Laggner, Rigidification of neutral lipid bilayers in the presence of salts, *Biophysical journal* 93 (8) (2007) 2688–2696.
- [104] J. M. Delgado, P. R. Nagy, S. Varma, Polarizable amoeba model for simulating  $\text{Mg}^{2+}$ ·protein·nucleotide complexes, *Journal of Chemical Information and Modeling* 64 (2) (2023) 378–392.
- [105] J. M. Delgado, P. S. Klein, S. Varma, Atp-ion complexation and lithium’s bioactive form in cellular solutions, *Journal of the American Chemical Society* 147 (22) (2025) 19061–19072, PMID: 40405352. arXiv:<https://doi.org/10.1021/jacs.5c04061>, doi:10.

1021/jacs.5c04061.

URL <https://doi.org/10.1021/jacs.5c04061>

- [106] M. Saunders, A. Adekoya-Olowofela, S. Downing, S. A. Pandit, Adsorption modes of  $\text{Na}^+$ ,  $\text{Li}^+$ , and  $\text{Mg}^{2+}$  to a model zwitterionic lipid bilayer, *Langmuir* 40 (49) (2024) 25892–25901.
- [107] K. K. Grotz, N. Schwierz, Optimized magnesium force field parameters for biomolecular simulations with accurate solvation, ion-binding, and water-exchange properties in spc/e, tip3p-fb, tip4p/2005, tip4p-ew, and tip4p-d, *Journal of Chemical Theory and Computation* 18 (1) (2021) 526–537.
- [108] P. Li, B. P. Roberts, D. K. Chakravorty, K. M. Merz Jr, Rational design of particle mesh ewald compatible lennard-jones parameters for  $+2$  metal cations in explicit solvent, *Journal of chemical theory and computation* 9 (6) (2013) 2733–2748.
- [109] H. I. Petrache, S. W. Dodd, M. F. Brown, Area per lipid and acyl length distributions in fluid phosphatidylcholines determined by  $^2\text{H}$  nmr spectroscopy, *Biophysical journal* 79 (6) (2000) 3172–3192.
- [110] J. Nagle, Area/lipid of bilayers from nmr, *Biophysical journal* 64 (5) (1993) 1476–1481.
- [111] K. K. M. Grotz, Development of optimized magnesium force field parameters for improved simulations of magnesium-rna interactions, Ph.D. thesis, Universitätsbibliothek Johann Christian Senckenberg (2022).
- [112] B. P. Fingerhut, J. Schauss, A. Kundu, T. Elsaesser, Contact pairs of rna with magnesium ions-electrostatics beyond the poisson-boltzmann equation, *Biophysical Journal* 120 (23) (2021) 5322–5332.

- [113] J. Puyo-Fourtine, M. Juillé, J. Hénin, C. Clavaguéra, E. Duboué-Dijon, Consistent picture of phosphate–divalent cation binding from models with implicit and explicit electronic polarization, *The Journal of Physical Chemistry B* 126 (22) (2022) 4022–4034.